พฤติกรรมของคอนกรีตเสริมเส้นใยเหล็กภายใต้แรงระเบิด

นายศักย์เกษม สุวรรณรัต

วิทยานิพนธ์นี้เป็นส่วนหนึ่งของการศึกษาตามหลักสูตรปริญญาวิศวกรรมศาสตรมหาบัณฑิต
สาขาวิชาวิศวกรรมโยธา ภาควิชาวิศวกรรมโยธา
คณะวิศวกรรมศาสตร์ จุฬาลงกรณ์มหาวิทยาลัย
ปีการศึกษา 2558

BEHAVIOUR OF STEEL FIBER REINFORCED CONCRETE UNDER BLAST LOAD

Mr. Sakkasem Suwarnarat

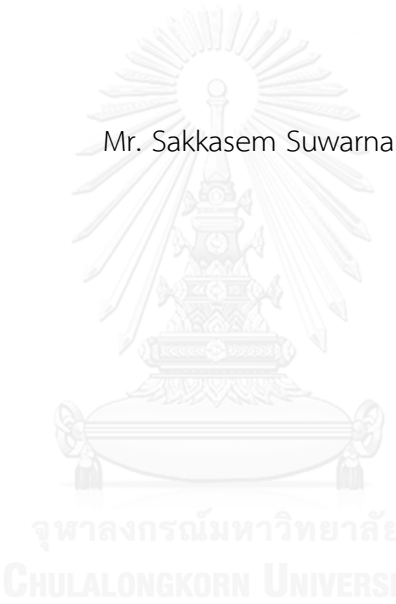

A Thesis Submitted in Partial Fulfillment of the Requirements

for the Degree of Master of Engineering Program in Civil Engineering

Department of Civil Engineering

Faculty of Engineering

Chulalongkorn University

Academic Year 2015

Thesis Title	BEHAVIOUR OF STEEL FIBER REINFORCED CONCRETE UNDER BLAST LOAD
By	Mr. Sakkasem Suwarnarat
Field of Study	Civil Engineering
Thesis Advisor	Associate Professor Withit Pansuk, Ph.D.
Thesis Co-Advisor	Colonel Assistant Professor Nuthaporn Nuttayasakul, Ph.D.

Accepted by the Faculty of Engineering, Chulalongkorn University in Partial Fulfillment of the Requirements for the Master's Degree

.....Dean of the Faculty of Engineering

(Associate Professor Supot Teachavorasinskun, Ph.D.)

THESIS COMMITTEE

.....Chairman

(Assistant Professor Watanachai Smittakorn, Ph.D.)

.....Thesis Advisor

(Associate Professor Withit Pansuk, Ph.D.)

.....Thesis Co-Advisor

(Colonel Assistant Professor Nuthaporn Nuttayasakul, Ph.D.)

.....Examiner

(Pitcha Jongvivatsakul, Ph.D.)

.....External Examiner

(Ganchai Tanapornraweekit, Ph.D.)

ศักย์เกษม สุวรรณรัต : พฤติกรรมของคอนกรีตเสริมเส้นใยเหล็กภายใต้แรงระเบิด (BEHAVIOUR OF STEEL FIBER REINFORCED CONCRETE UNDER BLAST LOAD) อ. ที่ปรึกษาวิทยานิพนธ์หลัก: รศ. ดร. วิทิต ปานสุข, อ.ที่ปรึกษาวิทยานิพนธ์ร่วม: พ.อ. ผศ. ดร. ณัฐพร นุตยะสกุล, 126 หน้า.

จากงานวิจัยที่ผ่านมาพบว่าการเสริมเส้นใยเหล็กในคอนกรีตสามารถเพิ่มความสามารถในการรับแรงดึงโดยเฉพาะเมื่อเกิดการการดึงด้วยความเร็วสูง งานวิจัยนี้นำเสนอผลการทดลองและผลจากโปรแกรมวิเคราะห์ สมรรถนะของแผ่นคอนกรีตเสริมเส้นใยเหล็กเปรียบเทียบกับแผ่นคอนกรีตธรรมดาที่ไม่มีการเสริมเส้นใยเหล็กเมื่อถูกกระทำด้วยแรงระเบิด มีการหล่อแผ่นคอนกรีตสองแผ่นต่อสัดส่วนเส้นใยเหล็กตั้งแต่ 0 (คอนกรีตไม่เสริมเส้นใย), 30, และ 60 กิโลกรัมต่อลูกบาศก์เมตร จำนวนแผ่นคอนกรีตมีจำนวนรวมทั้งหมด 6 แผ่น โดยมีการควบคุมค่ากำลังอัดของคอนกรีตให้อยู่ระหว่าง 55-60 MPa ชนิดของเส้นใยที่ใช้เป็นแบบปลายตะขอมีสัดส่วนความยาวต่อเส้นผ่านศูนย์กลางเท่ากับ 80 จากการศึกษาที่ผ่านมาพบว่าเส้นใยชนิดดังกล่าวสามารถรับแรงกระแทกได้เป็นอย่างดี แผ่นคอนกรีตถูกกระทำโดยแรงระเบิด TNT ปริมาณ 1lb และ 2 lb ที่ระยะคงที่เท่ากับ 0.5 เมตร ในการทดลองมีการตรวจวัด การเคลื่อนที่ของแผ่นคอนกรีตและอัตราเร่งของแผ่นคอนกรีต จากนั้นได้ทำการจำลองด้วยระเบียบวิธีไฟไนต์เอลิเมนต์ ด้วยโปรแกรมABAQUS เพื่อทำการเปรียบเทียบกับผลการทดลอง ผลจากการทดลองแสดงให้เห็นว่าแผ่นคอนกรีตเสริมเส้นใยเหล็ก มีความสามารถในการรับแรงระเบิดที่ดีกว่าแผ่นคอนกรีตธรรมดา และผลที่ได้จากการวิเคราะห์ด้วย ABAQUS ก็มีความใกล้เคียงกับผลการทดลอง

ภาควิชา วิศวกรรมโยธา ลายมือชื่อนิสิต .....

สาขาวิชา วิศวกรรมโยธา ลายมือชื่อ อ.ที่ปรึกษาหลัก .....

ปีการศึกษา 2558 ลายมือชื่อ อ.ที่ปรึกษาร่วม .....

5670397621 : MAJOR CIVIL ENGINEERING

KEYWORDS: BLAST-LOADING / STEEL FIBER / FINITE ELEMENT METHOD / FINITE ELEMENT ANALYSIS / ABAQUS

SAKKASEM SUWARNARAT: BEHAVIOUR OF STEEL FIBER REINFORCED CONCRETE UNDER BLAST LOAD. ADVISOR: ASSOC. PROF. WITHIT PANSUK, Ph.D., CO-ADVISOR: COL. ASST. PROF. NUTHAPORN NUTTAYASAKUL, Ph.D., 126 pp.

Recent studies show that adding steel fiber into concrete will enhance tensile capacity especially in high strain-rate loading condition. This thesis shows the results from experiments and finite element analysis simulations for the responses of steel fiber reinforced concrete (SFRC) panels and normal reinforced concrete (NRC) panels subjected to blast loading. Two panels per fiber weight ratio of 0 (concrete without fiber), 30, and 60 kg per cubic meter were casted. Total of 6 panels were casted with controlled cementitious matrix strength within a range of 55-60MPa. The steel fiber used in this study is hook-type fiber with an aspect ratio of 80 which, from past study, found to have a good performance for impact loading. The concrete panels were subjected to blast load using TNT explosive weighing 1lb and 2 lb all at a fix stand-off distance of 0.5 meter. Deflection and acceleration responses were measured from the experiment. Simulation models were developed via finite element analysis program "ABAQUS". The experiment results showed that the SFRC panels possesses better resistance against blast loading than NRC panels.The analysis models were also proven to have good accuracy in predicting panels' responses.

Department:	Civil Engineering	Student's Signature	.....
Field of Study:	Civil Engineering	Advisor's Signature	.....
Academic Year:	2015	Co-Advisor's Signature	.....

ACKNOWLEDGEMENTS

It is with immense gratitude that I acknowledge the support and help of my advisor Assoc. Prof. Dr. Withit Pansuk who continuously guided me throughout my research work. He convincingly conveyed a spirit of adventure in regard to research. Without his guidance and persistent help this dissertation would not have been possible.

I wish to thank Asst. Prof. Dr. Watanachai Smittakorn my dissertation committee chairman and Dr. Pitcha Jongvivatsakul my dissertation examiner for feedback, direction, and recommendation for my thesis writing.

I would like to thank my co-advisor Col. Asst. Prof. Dr. Nuthaporn Nuttayasakul, who managed all the authorization processes for the use of blast material and blast sites at Chulachomklao Royal Military Academy. Without his help the experiment would not have been successful

I would also like to express the deepest appreciation to my external examiner Dr. Ganchai Tanapornraweekit, who allow me to use the facilities at Asian Institute of Technology and Sirindhorn International Institute of Technology for casting of specimens and material testing.

I am indebted to the specialist team led by Wg. Cdr. Pratchaya Rianpuet from Defence Technology Institute, who provided the high speed camera Fastcam SA4 which captured very valuable and useful video footages for this research.

Lastly but most importantly, I would like to thank Siam Gabion Co.,Ltd., who provided the steel fiber at no charge. Thank you B.S.Y. Construction Co.,Ltd., who provided the equipment for installation of transducers. Thank you Siam Yamato Steel Co., Ltd., who helped in a fabrication of the steel rig used in the experiment.

This thesis is supported by Graduate School Thesis Grant, Chulalongkorn University

CONTENTS

Page

Page

Page

FIGURE CONTENTS

TABLE CONTENTS

CHAPTER 1 **Introduction**

1.1 General Background

Reinforced concrete is a popular and low-cost building material in Thailand. Concrete itself has a high compressive strength but low tensile capacity. Steel reinforcement is normally used to substitute this lacking characteristic. However, the steel member will become effective only when the bonding capacity of the two materials are properly made. This can be enhanced by the use of steel fiber reinforced concrete.

Presently, most of the numerous sites of the national department of defense's ammunition and explosive storages are of earth covered magazines (ECM) made of normal reinforced concrete (NRC). NRC structures are prone to cracks and thus water leakages. The authority has reported that the storages are now in need of renewal maintenance or replacement. Cracks were, reportedly, found on walls and roof panels of the structures causing severe water leakage. The leakage of water would cause further erosion of steel reinforcement underneath which will eventually result in lower structural integrity.

When a structure is subjected to a blast loading, the survivability of the structure depends on a durability of the element subjected to the load. This means the design of a structure subjected to blast load is element based where failure of a single important element could lead to a collapse of the whole structure.

Recent studies show that Steel Fiber Reinforced Concrete (SFRC) which is a ferrous material in a fibrous form will have a high dynamic increase factor (DIF) allowing the material to have very high tensile and compressive strength under high strain rate loading scenario such as blast loading. It is, therefore, viable that SFRC elements should provide a higher energy absorption capacity and thus perform better in resisting blast load as compared to the NRC elements. Steel fibers are also used in concrete to reduce cracks due to shrinkage and permanent load which should be useful in preventing water leakage in ECM.

Due to these views, it should be sensible to incorporate SFRC material in the design of structures subjected to blast load to prevent cracks and enhance blast load resistance capacity of ECM storage walls and panels as well as important structural elements for any concerned structures.

Full scale blast experiments are costly and the control of blast load is very difficult. Thus, small scaled experiment is preferable then an analytical model could be made to simulate the experiment. The same analytical model approach, after being verified with actual experiments, could then be used to simulate other scenarios in larger scales and more complex configurations.

To investigate the improvement in performance of the structure with adoption of SFRC material, actual experiment is conducted for both NRC and SFRC specimens to compare their results. To develop a finite element analysis (FEA) model, a computer program called "ABAQUS" will be used. To provide a positive impact to the civil engineering technology, the model is to be validated by comparing the analysis results with the experiment results for both NRC and SFRC panels. This will substantiate the additional specifications to the choices of building material and the design of future explosion resistance structures to provide better performance and thinner elements with higher blast load capacity. This is also even more useful when the new information is made available to the design of structures subjected to blast.

1.2 Research Objectives

- To investigate the improvements in performance of concrete panels in resisting blast load after an inclusion of steel fiber into the concrete by conducting actual experiments for NRC and SFRC panels to compare the responses between the two panel types.
- To predict the responses of both NRC and SFRC panels using FEA program ABAQUS.
- To validate the FEA results by comparing them with the experiment results.
- To suggest possible utilizations of SFRC properties in improving the performance of structure subjected to blast load.

1.3 Scope

- Blast load magnitudes considered are 1lb and 2lb with fixed 0.5 m standoff distance.
- FEA analysis do not include damage parameters in the material model, thus incapable of predicting the rebound behavior of the panels.
- Fiber type used in the experiment is hooked type fiber with an aspect ratio of 80.
- Only flexural mode of failure is considered in the analysis and experiment to observe the performance improvement due to enhanced tensile capacity of SFRC.

1.4 Expected outcome

- The finding of performance improvement of concrete panels in resisting blast load after the inclusion of steel fiber.
- The capability to create an accurate FEA model to simulate responses of SFRC and NRC panels subjected to blast load with flexural mode of failure.
- Deeper knowledge in incorporating SFRC material into the design of structures subjected to blast load.

CHAPTER 2 **Literature review**

2.1 Blast loading

2.1.1 Behavior and historical background of blast load

A blast is a rapid release of energy which may be released from many matters. This thesis will focus on a blast from a nucleic explosion where energy is released from the formation of different atomic nuclei by a rearrangement of the protons and neutrons within the interacting nuclei. Explosive materials are categorized according to their physical states. Explosion from solid state has highest intensity-weight ratio and intensity-volume ratio as compared to explosion from other states such as liquid and gas. Blast load effect from solid material is best known among all states. Explosive materials are also categorized accordingly to their ignition sensitivity; primary explosive materials can be ignited easily by flame, spark, or excessive impact. Primary explosives include mercury fulminate and lead azide; secondary explosive materials are less sensitive to ignition but create more catastrophic damage than the primary explosive. Secondary explosive materials include ANFO and toluene (TNT). (Beshara, 1994)

During the start of an explosion, the air pressure around the detonated explosive material increases to multiples of bars with an increase of temperature. The boundary of this high pressure and hot air suddenly expands to release the explosive energy into the surrounding air. This type of boundary expansion is called side-on overpressure. The side-on overpressure decays as the boundary expands away from the explosive source. The air pressure behind the explosive boundary increases to a maximum positive pressure then rapidly lowers down to a minimum pressure which is a little less than the ambient pressure before finally return back to the ambient pressure. (Ngo, Mendis, Gupta, & Ramsay, 2007)

Schematic of a typical overpressure time history at a certain location from an explosive source is as shown in figure 2.1.1-1 where overpressure means pressure that exceeds the ambient pressure.

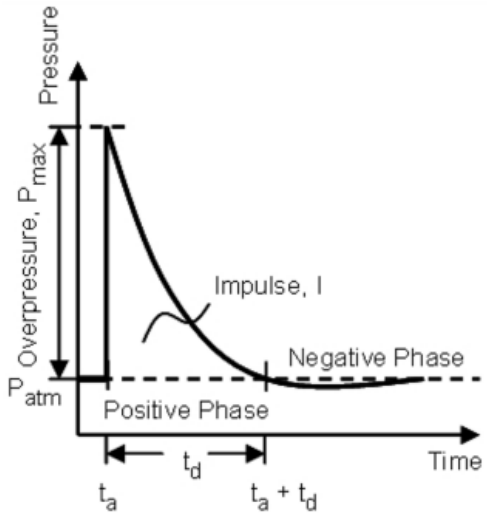

Figure 2.1.1-1 Typical overpressure time-history diagram due to an explosion (Borenstein & Benaroya, 2009)

Figure 2.1.1-1 can be expressed by the Friedlander's equation 2.1.2-1. (Borenstein & Benaroya, 2009)

$$P(t) = \begin{cases} 0 & ,t < ta \\ P_{\max}\left(1 - \dfrac{t - t_a}{t_d}\right) e^{-b\left(\frac{t-t_a}{t_d}\right)} & ,t_a \le t \le t_a + t_d \\ 0 & ,t > t_d \end{cases} \qquad (2.1.2\text{-}1)$$

Where:

$P(t)$ = overpressure at time t after the detonation

$P_{\max}$ = peak overpressure

t_d = duration of shockwave

t_a = arrival time of blast wave

b = explosive pressure decay constant

This equation represents pressure experienced by a certain point in the air medium. The parameters $P_{\max}$, t_d, t_a and b will be explain in later sections

2.1.2 Scaling of blast load.

Since The parameters $P_{\max}$, t_d, t_a, and b depend primarily on explosive weight and standoff distance, some types of scaling are used for the actual charge weight of interest. There are two types of scaling which are Sach's scaling and Hopkinson scaling, but Sach's scaling is more generic than Hopkinson scaling. However, Hopkinson scaling is more adequate for a detonation of conventional high explosive. The Hopkinson scaling (Z) is calculated by equation (2.3.1-1). (Baker, Cox, Westine, Koles, & Strehlow, 1983)

$$Z = \frac{R}{W^{1/3}} \qquad (2.3.1\text{-}1)$$

Where

R = stand-off distance, unit in meter

W = explosive weight, unit in kg of TNT

Explosive materials other that TNT may be scaled by first calculate an equivalent weight in TNT using equation (2.3.1-2)

$$W_{TNT} = \frac{H_{\exp}}{H_{TNT}} W_{\exp} \qquad (2.3.1\text{-}2)$$

Where

$W_{\exp}$ = weight of the explosive being used

$H_{\exp}$ = heat detonation of the explosive

H_{TNT} = heat detonation of TNT

The ratio $H_{\exp} / H_{TNT}$ can be defined as a ratio of energy output between the explosive and TNT material, the ratio is normally called TNT equivalence factor. The values for heat detonation of several explosive materials are tabulated in TM-5 1300 manual. (US Department of the Army, 1990)

2.1.3 Parameters for blast load time history generation

The parameters for blast load may be determined according to many sources. The paper published by Kingery and Bulmash provides detailed information for both side-on and reflected scenario which is also used to develop a blast load generation program called Conventional Weapon Effects Backfill (ConWeb). The empirical data used to make the program is available only for U.S. military and those who are associated with the government. (Kingery & Bullmash, 1984) An alternative information sources for blast load parameter are also available in the publication by Kinney and Graham (Kinnery & Graham, 1985), Smith and Hetherington (Smith & Hetherington, 1994) and Brode (Brode, 1955) which include all necessary information for the blast parameters.

The work of Kinney and Graham proposed equations to calculate for duration of shockwave t_d and peak side-on overpressure $P_{\max,s}$ as functions of scaled distance z as shown by equation 2.1.4-1 and 2.1.4-2 respectively.

$$\frac{t_d}{W^{1/3}} = \frac{980\left[1+\left(\frac{Z}{0.54}\right)^{10}\right]}{\left[1+\left(\frac{Z}{0.02}\right)^{3}\right]\left[1+\left(\frac{Z}{0.74}\right)^{6}\right]\sqrt{1+\left(\frac{Z}{6.9}\right)^{2}}} \qquad (2.1.4\text{-}1)$$

$$P_{\max,s} = 808 \cdot P_{atm} \frac{\left[1+\left(\frac{Z}{4.5}\right)^{2}\right]}{\sqrt{\left[1+\left(\frac{Z}{0.048}\right)^{2}\right]\left[1+\left(\frac{Z}{0.32}\right)^{2}\right]\left[1+\left(\frac{Z}{1.35}\right)^{2}\right]}} \qquad (2.1.4\text{-}2)$$

Where,

P_{atm} = atmospheric pressure in bars.

The work of Kinney and Graham studied for arrival time t_a and decay constant b then proposed experimental results for scaled distances ranging from 0.3 to 500. Guzas and Earls then later used piecewise polynomials fitting to obtain expressions for both arrival time and decay constant. Equation 2.1.4-3 is used to calculate for arrival time t_a where a_i is tabulated in the Table 2.1.4-1. (Guzas & Earls, 2010)

$$\frac{t_a}{W^{1/3}} = \sum_{i=1}^{4} a_i Z^{i-1} \qquad (2.1.4\text{-}3)$$

$Z(m/kg^3)$	a_1	a_2	a_3	a_4
$0.3 \le Z \le 2.4$	$1.769362e^{-2}$	$-2.032568e^{-2}$	$5.395856e^{-1}$	$-3.010011e^{-2}$
$2.4 < Z < 12$	-2.251241	1.765820	$1.140477e^{-1}$	$-4.066734e^{-3}$
$12 \le Z \le 500$	-6.852501	2.907447	$9.466282e^{-5}$	$-9.344539e^{-8}$

Table 2.1.3-1 Coefficient for arrival time calculation

Similarly, equation 2.1.4-4 can be used to calculate decay constant b where c_i is tabulated in the Table 2.1.4-2 (Guzas & Earls, 2010)

$$b = \sum_{i=1}^{6} c_i Z^{i-1} \qquad (2.1.4\text{-}4)$$

$Z(m/kg^3)$	c_0	c_1	c_2	c_3	c_4	c_5
$0.3 \le Z < 0.95$	$3.08473e^2$	$-2.14692e^3$	$5.95329e^3$	$-8.22603e^3$	$5.68743e^3$	$-1.57341e^3$
$0.95 \le Z < 2.4$	$1.76074e^1$	$-2.67855e^1$	$1.78607e^1$	$-5.65557e^0$	$6.94164e^{-1}$	0
$2.4 \le Z < 6.5$	$4.43216e^0$	$-2.67855e^1$	$7.41973e^{-1}$	$-9.34132e^{-2}$	$4.46971e^{-3}$	0
$6.5 \le Z < 40$	$7.11610e^{-1}$	$-6.26846e^{-2}$	$3.32532e^{-3}$	$-8.24049e^{-5}$	$7.61887e^{-7}$	0
$40 \le Z \le 500$	$2.51614e^{-1}$	$-1.76758e^{-3}$	$9.51638e^{-6}$	$-2.19712e^{-8}$	$-2.19712e^{-8}$	0

Table 2.1.3-2 Coefficient for decay constant calculation

The experimental data used to generate the piecewise polynomial equation is for the side on scenario or when the angle of incident is at $90°$. However, the pressure is greatest at $0°$ angle of incident; the pressure occurs in this scenario is call reflected overpressure (P_r). According to the work of baker, the decay behavior for side-on and reflected air blast overpressure is almost identical. Baker stated that the ratio between Impulse and maximum pressure for both side-on and reflected scenarios is constant which means that equation 2.1.4-5 may be assumed. (Baker et al., 1983)

$$\frac{I_r}{I_s} = \frac{P_r}{P_s} \qquad (2.1.4\text{-}5)$$

This also means that the decay constant b can be used interchangeably for side-on and reflected pressure. The impulse may also be calculated by integrating equation 2.1.2-1 resulting in equation 2.1.4-6.

$$I = \frac{P_{\max} t_d e^{-b}(b \cdot e^{-b} - e^{-b} + 1)}{b^2} \qquad (2.1.4\text{-}6)$$

Kinney and Graham also provided an equation to calculate for impulse for side-on scenario as shown by equation 2.1.4-7

$$I_s = \frac{0.067\sqrt{1+\left(\frac{z}{0.23}\right)^4}}{Z^2\sqrt[3]{1+\left(\frac{z}{1.55}\right)^3}} \qquad (2.1.4\text{-}7)$$

According to the experiment data from the work of Kinney and Graham, impulse obtained from equation 2.1.4-5 is found to be more accurate than that from equation 2.1.4-6, meaning the piecewise polynomial fitting approach is more accurate in calculating impulse from air blast loading.

In the manual TM 5-1300 published by the US army and the US Navy, a simplified triangular time history profile as shown in figure. 2.1.4-1 is suggested for preliminary determination of blast load where the area under the triangle must be equivalent to the impulse I of a particular blast load and the peak overpressure must

be equivalent to the calculated value. Therefore, the approximate blast time duration may be calculated using equation 2.1.4-8. (US Department of the Army, 1990)

$$t_d^{'} = \frac{2I}{P_{\max}} \qquad (2.1.4\text{-}8)$$

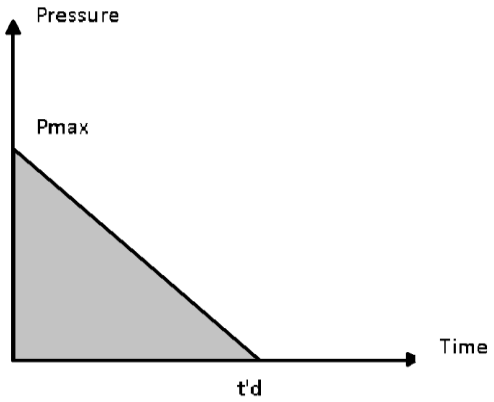

Figure 2.1.3-1 Simplified blast load triangular time history diagram

Equation 2.1.4-2 is for the calculation of side-on overpressure: reflected overpressure, as explained earlier, exerts greater pressure. The work of Brode includes an equation to calculate the reflected pressure P_r as a function of the side-on or incident pressure $P_{\max,s}$ which can be calculated by equation 2.1.4-9 when heat ratio of the air medium is 1.4; this is when the air molecule react independently (ideal gas) or when the pressure is less than 6.9 bars. However, at the pressure greater than 6.9bars, the air molecules will have mutual interaction and P_r is calculated with equation 2.1.4-10. (Brode, 1955)

$$P_r = P_s\left(2 + \frac{6P_s}{P_s + 7P_{atm}}\right) \qquad \text{for } P_s < 6.9bar \qquad (2.1.4\text{-}9)$$

$$P_r = P_s\left(\frac{0.03851P_s}{1 + 0.0025061P_s + 4.041e^{-7}P_s^2} + 2 + \frac{0.004218 + 0.7011P_s + 0.001442P_s^2}{1 + 0.1160P_s + 8.086e^{-4}P_s^2}\right)$$

$$\text{for } P_s \geq 6.9bar \qquad (2.1.4\text{-}10)$$

Actual blast overpressure depends on the angle of incident (θ). In fact, the actual overpressure is a combination of side-on and reflected overpressure. Randers-Pehrson and Bannister gives an equation to calculate an air blast profile for an air blast event with known reflected and side-on overpressure using equation 2.1.4-11. (Randers & A.B., 1997)

$$P(t,\theta) = P_r(t)\cos^2\theta + P_s(t)(1+\cos^2\theta - 2\cos\theta) \qquad (2.1.4\text{-}11)$$

The same assumption as that for equation 2.1.4-12 may be used to calculate for total Impulse contributed from side-on and reflected overpressure with equation 2.1.4-13

$$I(\theta) = I_r\cos^2\theta + I_s(1+\cos^2\theta - 2\cos\theta) \qquad (2.1.4\text{-}13)$$

Using simplified triangular time-history assumption for blast overpressure, the time duration may be calculated by equation 2.1.4-14.

$$t_d^*(\theta) = \frac{2I(\theta)}{P(t=t_a,\theta)} = \frac{2I(\theta)}{P_r\cos^2\theta + P_s(1+\cos^2\theta - 2\cos\theta)} \qquad (2.1.4\text{-}14)$$

Since the overpressure time-history curves for reflected and side-on overpressure are similar, this equation is further simplified to equation 2.1.4-12

$$P_{\max}(\theta) = P_r\cos^2\theta + P_s(1+\cos^2\theta - 2\cos\theta) \qquad (2.1.4\text{-}12)$$

Overpressure may be assumed as equivalent to reflected overpressure for conservative design. However, in the case where the explosive source is located very close to the affected surface, this assumption may results in an overdesign as the blast wave arriving at the structural element will be at varying angle of incident as shown in

figure. 2.1.4-2 where the angle of incident varies as much as from 0 to 45 degrees. (Chock & Kapania, 2001)

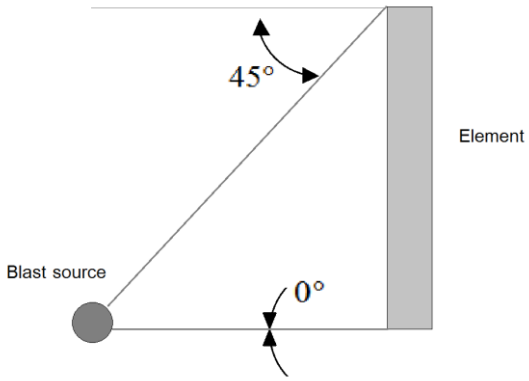

Figure 2.1.3-2 Diagram shows varying angle of incident

2.1.4 Mach effect.

Mach effect is a superposition of reflected shock and incident shock. As a detonation occurs at a certain height above the surface, a spherical wave front is formed and partly reflects with the ground at varying angle of incident from zero at the ground zero right below the epicenter of the explosion to 90 degree at the distance away from the epicenter. The air behind the incident shock which is hotter than the air ahead causes the following reflected wave to travel faster. At a certain time the reflected wave catches up with and reinforce the incident wave as shown in the most-right diagram of figure 2.1.5-1. The region where the reflected wave reinforces the incident wave is called irregular or Mach reflection region. The top of the region is called triple point which is where the Mach reflection shock, reflected shock, and incident shock are converged. (US Department of the Army, 1990)

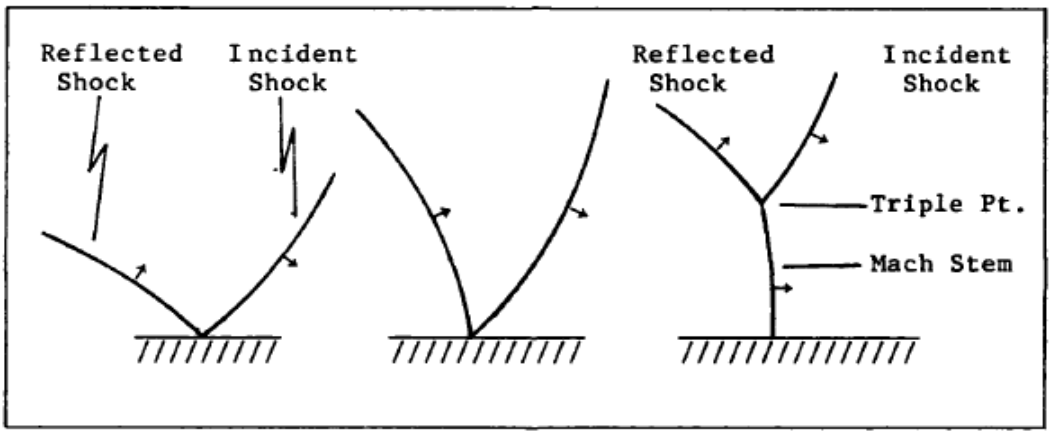

Figure 2.1.4-1 Occurrence of Mach Stem (US Department of the Army, 1990)

Another effect is concerned with the reflected shock at the location just below the explosion. This happens when the explosion is at or very near to the ground. The reflected wave travels through the source region which is heated to a very high temperature then reinforces the incident shock above the explosive region as shown in figure 2.1.5-2. This particular region is called region of coalescence.

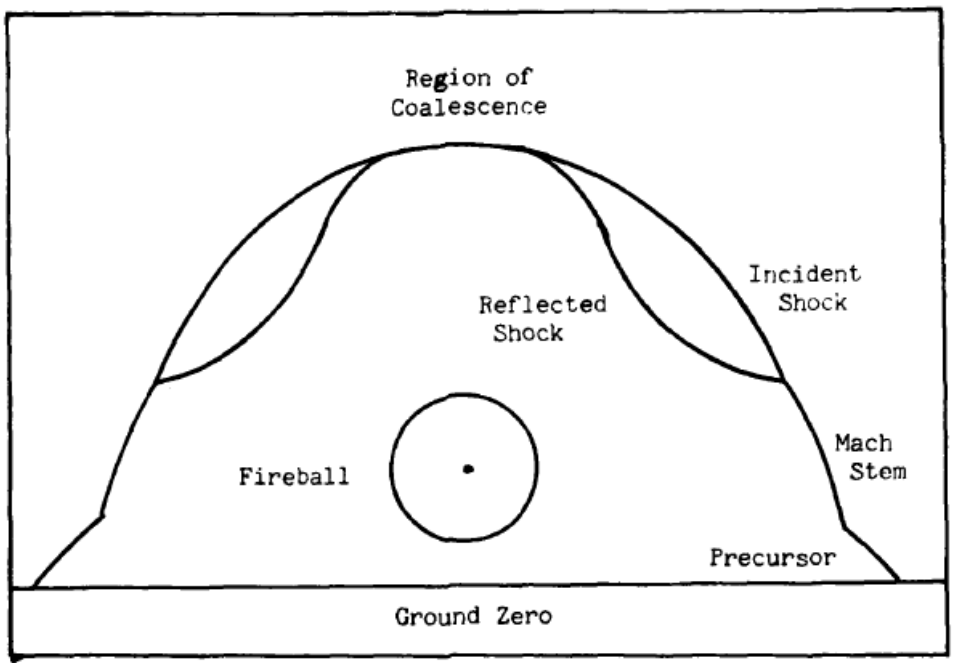

Figure 2.1.4-2 Region of coalescence (US Department of the Army 1990)

2.1.5 Hemispherical blast.

Hemispherical blast is considered when the detonation is near or at the ground surface where the top half of the explosive sphere is reinforced by the reflected ground shock. This phenomenal can be described as Mach effect as explained in earlier section.

TM 5-1300 provides separate blast parameters for spherical and hemispherical blasts. The parameters are presented as plotted graphs. The work of Baker also suggests an alternative method to consider the effect of ground surface detonation where the bottom half of the spherical wave immediately reflects with the ground surface and overlaps with the incident wave at the very start of the explosion. This effect should amplify the incident wave by two folds, however some of the energy is absorbed by the ground and the amplification factor of 1.8 is recommended. Thus, the over-pressure time history diagram for the hemispherical blast scenario is the same as mid-air spherical blast scenario but with an amplification factor of 1.8. (Baker et al., 1983)

2.1.6 CONWEP model for incident shock waves simulation

The FEA program ABAQUS provides a shock waves simulation function "CONWEP" which is capable of simulating an outward propagating shock wave of an explosion in air from compressed gas mass interacting with surrounding air. The function is also capable of simulating hemispherical incident waves from a surface blast. The simulation is based on empirical data sets provided by the CONWEP function which requires two input parameters including equivalent detonated mass of TNT and equivalent standoff distance. The function is able to generate the overpressure time-history graph to simulate the load caused by the blast. The distance of loading surface from the source of explosion or standoff distance is automatically calculated by ABAQUS according to the geometry of the created model. The program uses the same principle suggested by Randers-Pehrson (discussed in 2.1.4) to account for the effect from reflected wave front.

The CONWEP function is valid within a range of standoff distance which must be larger than the charge radius or else the analysis is terminated. The valid range depends on the charge radius of particular charge weights. The function do not include effects from shadowing or the effects from obstructing objects, thus load from reflected waves must be considered if relevant.

2.2 Blast resistance design review

2.2.1 Goals of blast resistance design

The main goal off most structural designs is to determine appropriate section sizing and reinforcement configuration such that the structure stays intact when subjected to normal loading conditions such as wind loading, gravity loading, and earth quake loading. Blast loading is less common and rarely considered in most structural design, however, this is not the case for important structures or those that are very likely to be exposed to blasts such as ammunition storage. A structure is expected to stay intact and remain in service after subjected to normal loading. For extreme load conditions such as intense earthquake load and blast load, the structure is not expected to remain in service, but safety of lives must be ensured. For the case of ammunition storages, damaging effects should be minimized especially to adjacent structure in order to prevent progressive explosion.

In some cases, only a portion of the structure is subjected to the blast load. If the subjected element is important to the stability and integrity of a whole structure, complete failure or loss of the element may cause progressive collapses and thus failure of the structure as a whole. This means that important elements of the structure must have adequate toughness, ductility, strength and dynamic capacity to survive in a blast event. (Mccann & Smith, 2007)

2.2.2 Method in determining structural resistance to blast load

To evaluate if a structure can survive a blast load, the respond of the structure subjected to blast load must be determined. Blast load is different in nature as compared to other common loading types, it is an extreme load scenario which may cause removal or large permanent deflection to the subjected element. Thus, choosing the method of analyzing the structural respond depends on the goal of the design. From the literature review, methods in analyzing the structure are divided into three categories

- The most accurate way of determining structural respond is called "coupled dynamic analysis" where overpressure from the blast load changes with the deformation of the subjected element. This method is used by many design programs such as SHAMRC. This method, however, requires rigorous model fabrication and computational effort, making it expensive and time consuming. In fact, RC elements can be assumed almost rigid during the blast event and the effect of coupled dynamic is small especially for short standoff distance of accidental explosion. (Crepeau, 2001)

- Uncouple single or multi-degree of freedom dynamic analysis using FEA method is as accurate as the coupled dynamic analysis method for the case that coupling effect is small. FEA method can capture all material behaviors including nonlinearity, strain-rate sensitivity, as well as geometric nonlinearity. This method is, however, time consuming and demands high computation effort. Since the design is elemental-focus, this method may be applied to a small elemental analysis of the structure, only important portion of the structure may be analyzed to determine the resistance of a whole structure

- The most conservative approach in determining performance of a structure is to assume complete removal of the subjected element from the structure. This method was implemented by the Government Security Agency. The guideline for this method is found in the manual “Progressive Collapse Analysis and Design Guideline”. The aim of this design method is to prevent progressive collapse of the structure when an element is removed from the structure where the remaining capacity of the structure must be able to withstand factored load of 2x(deadload+25%lifeload). This type of analysis is simple but not economical and may not be appropriate for some structure. (GSA, 2003)

2.2.3 Ammunition and explosive storage design and specification

Current Ammunition and explosive storage in Thailand

Current ammunition and explosive storages in Thailand are earth covered magazines built with normal reinforced concrete which have been in use for almost as long as the expected structural life-span of approximately 30 years. From recent inspection, intermediate cracks are found throughout the structure revealing signs of repair, renovation or replacement. Water leakage from the earth cover through the intermediate cracks causes corrosion in steel and tendency in compromising the structural integrity. The storage has a dimension of 30 m wide, 30 m long and 7.3 m in height. The storage is earth covered magazine type where the embedded RC structure is a half cylinder with thickness of 15cm. Figure 2.2.3-1 through 2.2.3-4 roughly illustrate construction drawings of the existing AE storage in Thailand.

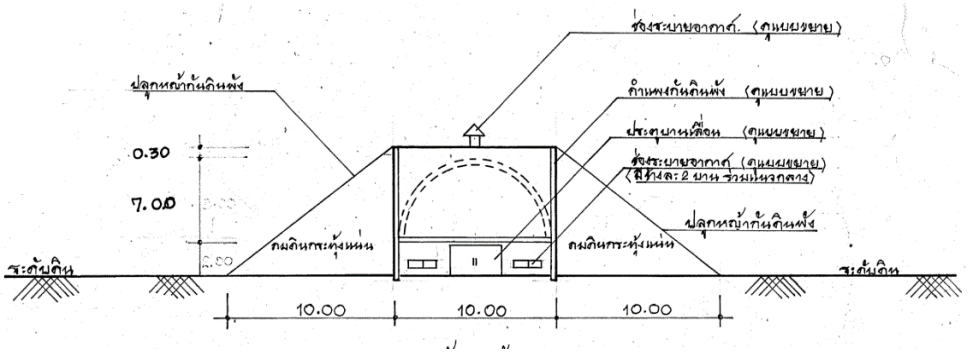

Figure 2.2.3-1 Construction drawings of the existing Ammunition storage in Thailand

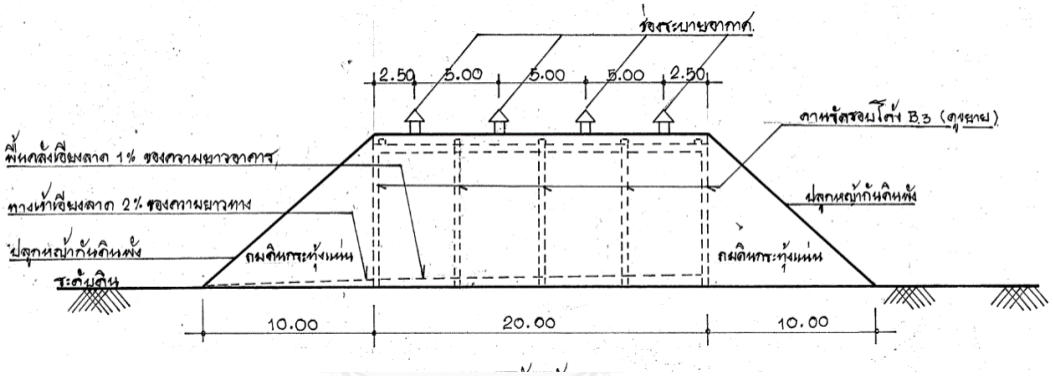

Figure 2.2.3-2 Construction drawings of the existing Ammunition storage in Thailand

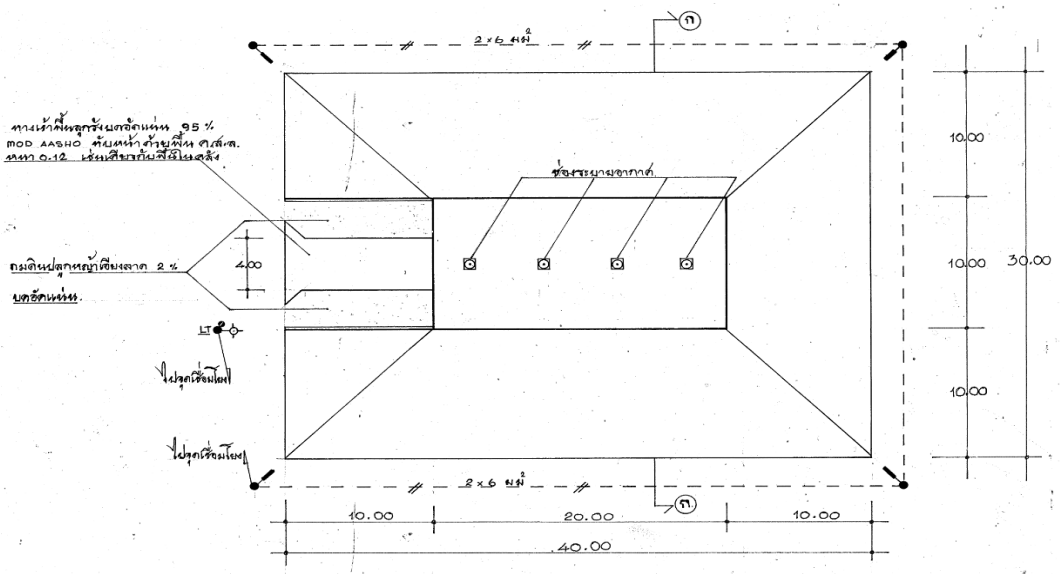

Figure 2.2.3-3 Construction drawings of the existing Ammunition storage in Thailand

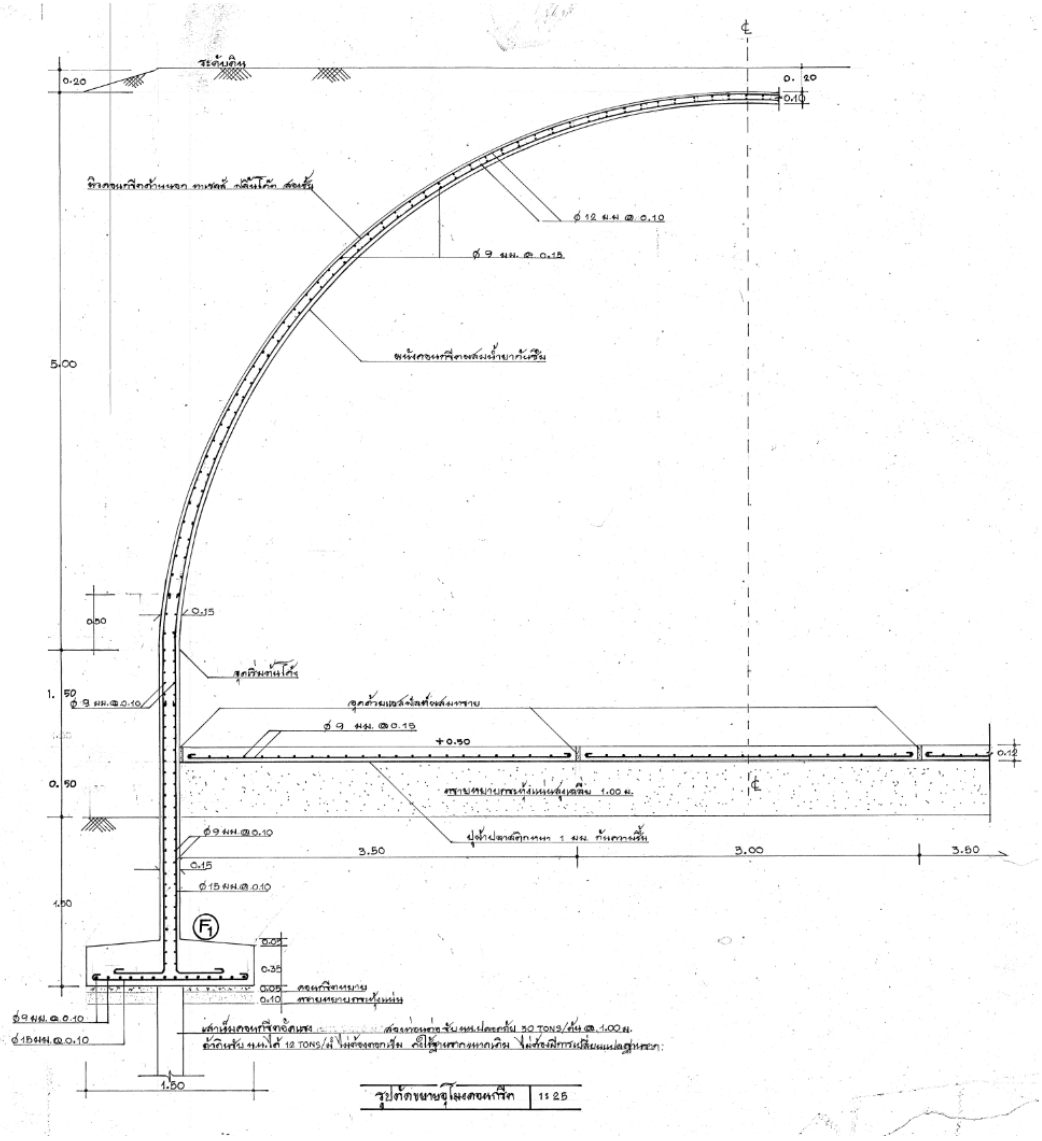

Figure 2.2.3-4 Construction drawings of the existing Ammunition storage in Thailand

National institute of building science Ammunition and explosive storage magazine design guidance.

Whole building design guide (WBDG) is a program of the national institute of building science (NIBS) which provides the guideline for building ammunition explosive storage magazine. The guideline mainly considers the uniform minimum AE safety standard for personal and property established by the Department of Defense Explosive Safety Board (DDESB). The explosive safety standards is a part of Dod 6055.09-M guideline. The guideline is used for the entire storage magazines approved by the department of defense (DoD) of the United States

The scope of the design guideline does not cover the capability of the AE storage to resist the damaging effect from internal explosion but the design scope is such that, in case of accidental explosion, the adjacent AE storages located at appropriate specified Explosive Safety Quantity- Distance (ESQD) will not be affected or consecutively detonated.

WBDG provides a wide variety of Earth Covered Magazine (ECM) designs which are designed according to the AE safety standard required by the DoD. ECM designs are categorized into 3 main categories according to their hardness and explosive resistance capability. The 3 categories are listed out as following

- "7-bars" standard design, this type of ECM provides highest blast load resisting capacity allowing the least magazine separation distance. Magazines with this categorization may contain up to 500,000 pound net explosive weight (NEW).
- "3-bars" design, this type of ECM allows less containment amount of 300,000 pound NEW and requires greater separation distance between magazines.
- "Undefined" Nonstandard Designs, this type of ECM provides lowest blast load resisting capacity.

The 7-bars and 3-bars ECM designs were approved by DDESB while the undefined ECM is in the progress of determining explosive resisting capacity from the analysis result and not yet approved by DDESB. Complete drawings for construction of approved ECM designs are readily available in the WEDG website which includes all blast parameters used in the analysis of the structure as well as the required inter-magazine separation distance. (WBDG, 2016)

2.3 Mechanical property of NRC and SFRC

Mechanical properties for all materials used in the test specimens are to be modelled for a development of FEA model in ABAQUS. This section shows theories used to determine stress-strain relationships for both NRC and SFRC.

2.3.1 Stress-strain relationship of NRC in compression

In general, the maximum stress or peak stress of concrete depends on the strength of concrete mix. The maximum stress is reached at strain between 0.0015 and 0.003 which is then followed by a descending branch. The stress-strain curve is mainly characterized by a formation of micro-cracks in concrete matrix.

The modified Hognested stress-strain model represents the behavior of concrete with stress less than or equal to 6000 psi. As shown in the figure 2.3.1-1, the curve consists of a second degree parabola with maximum stress f_c'' of 90% compressive strength or $0.9f_c'$ at a strain of $1.8f_c''/E_c$ then followed by a linear descending branch which terminates at stress of $0.85f_c''$ and strain of 0.0038. (Wight & MacGregor 2012)

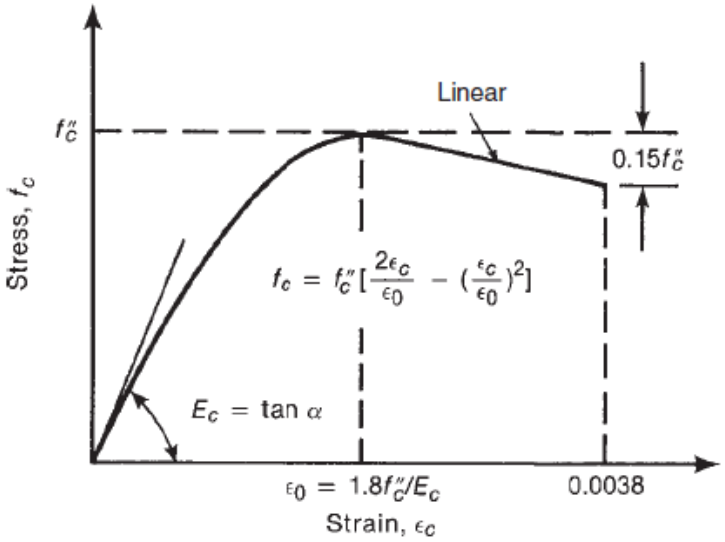

Figure 2.3.1-1 Modified Hognested stress-strain model (Wight & MacGregor 2012)

Todeschini also proposed a stress-strain relationship represented by a single continuous equation as shown in the figure 2.3.1-2 where the maximum stress is also taken to be equal to $f_c^{"}$ or $0.9f_c^{'}$ but at a strain of $1.7f_c^{"}/E_c$. (Wight & MacGregor 2012)

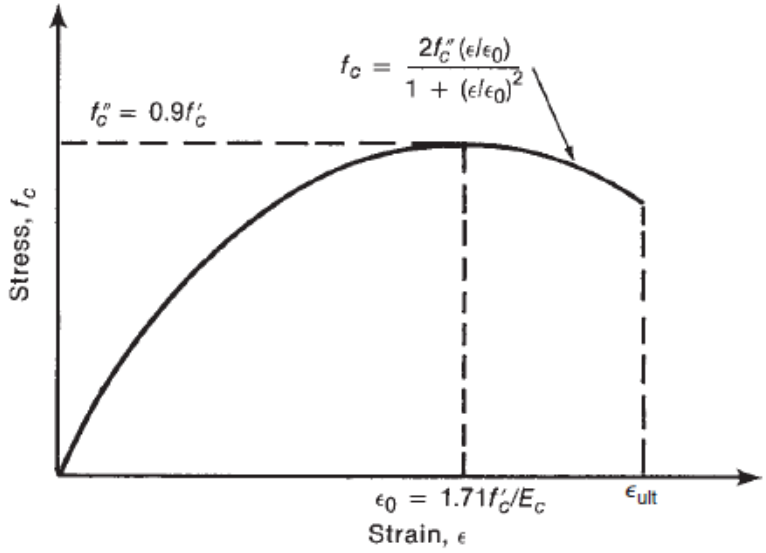

Figure 2.3.1-2 proposed a stress-strain relationship by Todeschini (Wight & MacGregor 2012)

These two stress-strain relationships were later reviewed by Popov Thorenfeldt, Tomaszewicz, and Jensen whom later proposed a refined relationship equation which may be used for concrete with strength ranging from 15 to 125 MPa as shown by equation 2.3.1-1. (Wight & MacGregor 2012)

$$\frac{f_c}{f_c'} = \frac{n(\varepsilon_c / \varepsilon_0)}{n-1+(\varepsilon_c / \varepsilon_0)^{nk}} \qquad (2.3.1\text{-}1)$$

f_c' = Peak stress obtained from a cylinder test,

ε_0 = Strain at peak stress,

n = curve fitting factor = $E_c / (E_c - E_c')$

E_c = initial tangent modulus

E_c = f_c'/ε_0

k = controlling factor of the descending branch which is equal to 1 when $\varepsilon_c / \varepsilon_0$ is less than 1.0 and greater than 1 when $\varepsilon_c / \varepsilon_0$ greater than 1.0.

In the case where ε_0, E_c, and k are not available from the experiment, following equations 2.3.1-2 through 2.3.1-5 are used instead.

$$n = 0.8 + \left(\frac{f_c'}{2500}\right) \qquad (f_c' \text{ is in psi}) \qquad (2.3.1\text{-}2)$$

$$k = 0.67 + \left(\frac{f_c'}{9000}\right) \geq 1.0 \qquad (f_c' \text{ is in psi}) \qquad (2.3.1\text{-}3)$$

$$\varepsilon_0 = \frac{f_c'}{E_c}\left(\frac{n}{n-1}\right) \qquad (2.3.1\text{-}4)$$

$$E_c = 57{,}000\sqrt{f_c'} \qquad (f_c' \text{ is in psi}) \qquad (2.3.1\text{-}5)$$

2.3.2 Stress-strain relationship of NRC in tension

Plane concrete normally has tensile strength as low as only 10% of the compressive strength and usually taken as zero in conservative design. However, for accurate modeling of concrete material, tensile behavior of concrete should not be omitted.

There are two phases in the tensile stress-strain curve for concrete including the linear part and the curved part. The strain at peak stress is approximately 0.0001 for pure tension and 0.00014 to 0.00012 for flexure. The stress-strain relationship may be modeled as a parabola or a straight line with a slope being equivalent to modulus of elasticity of concrete (E_c) and with maximum tensile stress of $f_t^{'} = 6.4\sqrt{f_c^{'}}$ (psi) at strain of $\varepsilon_t^{'} = 1.8 f_t^{'} / E_c$ where $E_c = 57000\sqrt{f_c^{'}}$ (psi). The curve is as shown in Figure 2.3.2-1. (Wight & MacGregor 2012)

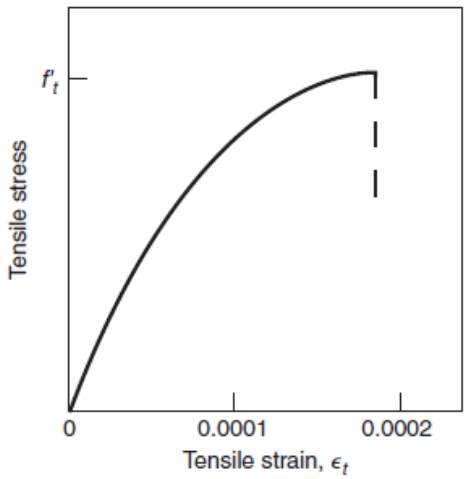

Figure 2.3.2-1 Tensile strength of concrete (Wight & MacGregor 2012)

Figure 2.3.2-1 shows that, tensile stress rapidly drops to zero after the maximum tensile stress is reached. However, the modeling of tensile behavior should also cover the descending branch of tensile stress called “Tension softening”. During the tension

softening, tensile strength gradually drops to zero. A model that is able to represent this behavior was proposed by Rim Nayal and Hayder A Rashseed which may be represented by a curve as shown in figure 2.3.2-2 where $\sigma_{t0} = 0.3 f_{cu}^{2/3}$ and $\varepsilon_{cr} = \sigma_{t0} / E_c$. (Alih & Khelil, 2012)

Wahalathantri, Thambiratnam and Chan later pointed out that the sudden drop in stress after the maximum may cause runtime-error in the analysis and that the tensile strength should not reduce to zero. With these considerations and some calibration explained in the paper, a refined curve is proposed as shown in figure 2.3.2-3. (Wahalathantri & Thambiratnam, 2008)

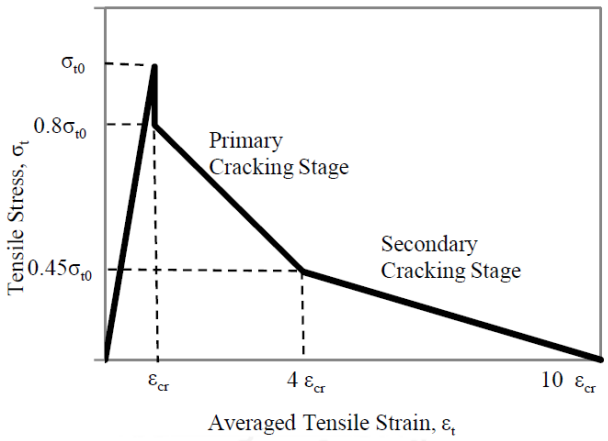

Figure 2.3.2-2 Tensile stress-strain relationship for concrete with softening behavior (Alih & Khelil, 2012)

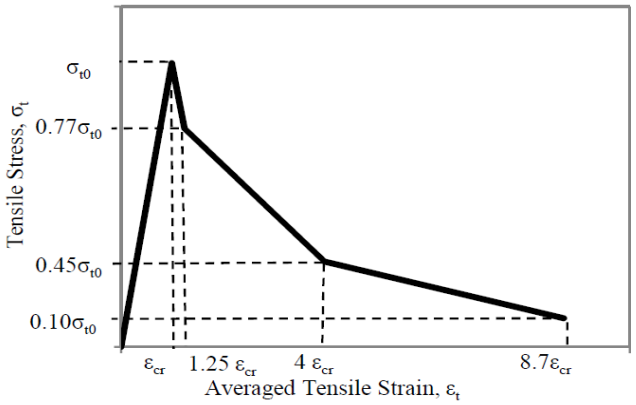

Figure 2.3.2-3 Refined Tensile stress-strain relationship (Wahalathantri & Thambiratnam, 2008)

2.3.3 Stress-Strain relationship of SFRC in compression

Neves and Almeda conducted a research to investigate the compressive strength of SFRC with controlled parameters including concrete strength, fiber ratio, length, and diameter of fiber; the compressive strength ranges from 35 to 60 MPa; fiber volumetric ratio ranges from 0 to 1.5%; fiber diameter ranges from 0.375 to 0.55m and a fixed fiber length of 30mm. By conducting series of compressive test, Neves and Almeda proposed equations to calculate modulus of elasticity and strain at peak stress which may be calculated by equation 2.3.3-1 and 2.3.3-2 respectively. Neves and Almeda also proposed a stress-strain relationship of SFRC in compression for use in finite element analysis which was later improved by Bhargava resulting in a complete stress-strain relationship for SFRC as shown by equation 2.3.3-3. (Bhargava, Sharma, & Kaushik, 2005)

$$E_{cf} = \left(10.5 - 0.22V_f\right) f_c^{1/3} \qquad (2.3.3\text{-}1)$$

$$\varepsilon_{cf} = 0.69 f_{cf}^{'\left[0.29+0.0002V_f\left(l_f/d_f^2\right)\right]} \qquad (2.3.3\text{-}2)$$

$$\sigma_{cf} = f_{cf}^{'}\left(\frac{k_1\beta\left(\frac{\varepsilon_{cf}}{\varepsilon_{cf}^{'}}\right)}{k_1\beta - 1 + \left(\frac{\varepsilon_{cf}}{\varepsilon_{cf}^{'}}\right)^{k_2\beta}}\right) \qquad (2.3.3\text{-}3)$$

$$k_1 = k_2 = 1$$

And for the descending part of the curve,

$$k_1 = \left(\frac{D}{f_{cf}^{'}}\right)^{3.79}, \quad k_2 = \left(\frac{G}{f_{cf}^{'}}\right)^{1.46}$$

Where,

$$D = 35.635 + 17.21(R.I.) + 9.11(R.I.)$$

$$G = 31.82 + 16.39(R.I.) + 9.35(R.I.)$$

$$\beta = \left(\frac{f_{cf}^{'}}{A}\right)^3 + C$$

$$A = 50.35 + 22.31(R.I.) + 19.13(R.I.)$$

$$C = 2.04 - 0.313(R.I.) - 0.155(R.I.)$$

And for the reinforcement index,

$$R.I. = V_f \frac{l_f}{D_f}$$

Where,

V_f = volume metric ratio of steel fiber

l_f = length of steel fiber

D_f = diameter of steel fiber

σ_{cf} = stress at strain $\varepsilon_{cf}^{'}$

$f_{cf}^{'}$ = peak compressive stress

$\varepsilon_{cf}^{'}$ = strain at peak compressive stress

2.3.4 Stress-Strain relationship of SFRC in Tension

Tensile behavior of SFRC is different from that of NRC. SFRC has higher peak stress and longer softening path. Carreira and Chu suggested a continuous function to represent both ascending and descending paths for tensile stress-strain behavior of normal concrete. The function was further modified by Al-Taan and Shammasby to account for the effect of fibrous material in concrete; the modified function may be written as shown in equation 2.3.4-1. (AL-TAAN & SHAMMAS, 2006)

$$\frac{f_t}{f_{tf}^{'}} = \frac{\beta\left(\varepsilon / \varepsilon_{tf}\right)}{\beta - 1 + \left(\varepsilon / \varepsilon_{tf}\right)^{\beta}} \qquad (2.3.4\text{-}1)$$

Where,

ε = the tensile strain at a stress f_t

$f_{tf}^{'}$ = tensile strength of SFRC

ε_{tf} = strain at peak stress

β = a parameter represents fiber characteristic

According to Nataraja's and Ezelsin's works the fiber parameter β is to be calculated as shown in equation 2.3.4-2 through 2.3.4-4 for different types of fiber. (Ezeldin & Balaguru, 1992)

$\beta = 1.0930 + 0.7132 R.I.^{-0.9260}$ for hooked fiber, (2.3.4-2)

$\beta = 1.0930 + 7.4848 R.I.^{-1.3870}$ for smooth fiber, (2.3.4-3)

$\beta = 0.5811 + 1.9300 R.I.^{-0.7406}$ for crimped fiber, (2.3.4-4)

Where,

$R.I.$ = $w_f l_f / d_f$

w_f = weight ratio of fiber to that of concrete

l_f = length of fiber

d_f = diameter of fiber

According to Soroushain and Lee, when no experimental data is available, tensile strength (f'_{tf}) and strain at peak stress (ε_{tf}) may be calculated with equation 2.3.4-5 and 2.3.4-6 respectively. (Soroushian & Lee, 1989)

$$f'_{tf} = f'_t(1+0.016N_f^{1/3}+0.05\pi N_f d_f l_f) \quad (2.3.4\text{-}5)$$

$$\varepsilon_{tf} = \varepsilon_t(1+0.35N_f d_f l_f) \quad (2.3.4\text{-}6)$$

Where,

ε_t = cracking strain of plain concrete = f'_t / E_c

f'_t = tensile strength of plain concrete = $0.7\sqrt{f'_c}$

E_c = elastic modulus of plain concrete

N_f = No. of fiber per unit area = $\eta_0(4V_f / \pi d_f^2)$

η_0 = orientation factor which is taken as 0.5

V_f = fiber volume fraction

2.4 Behavior of fiber reinforced concrete (SFRC) under blast loading

Fibrous material is commonly added to concrete element to improve performance in many ways. It is commonly added to reduce cracks and improve flexural and shear capacities. More importantly, fibrous material greatly improve the strength and ductility within yielding limit or in post-cracking region allowing the material to have improved strain-softening or strain-hardening behavior while the post-

cracking peak becomes higher than the elastic peak. In the other hand, non-fibrous concrete exhibit less strain-softening where cracks are formed as soon as the elastic limit is reached resulting in a sudden reduction in strength after the yielding point.

2.4.1 Fiber types

There are many types of fiber currently available commercially including glass, cellulose, Poly-vinyl, synthetic and steel fibers, in varieties of shape. Smaller size fibers, such as micro-synthetic and nylon fibers, are used to control plastic shrinkage cracking in concrete. Larger size fibers, such as deformed steel fiber, are used to enhance ductility, toughness, and post-crack strength. Steel fibers are made of stainless steel or carbon with sizes ranging from 1 to1.5 inches. Hooked and twisted steel fibers are the most popular among all available shapes. The hooked type is proven to have highest energy absorption capacity but the twisted-type fiber is proven to have higher strain-rate sensitivity in improving effective strength of the concrete matrix. (Tran & Kim, 2014)

2.4.2 Strain-rate effect on NRC and SFRC

Mechanical behaviors of steel fiber reinforced concrete composite has been studied for a long time. The composite is well known as high performance fiber reinforced cement composites (HPFRCC) which has high tensile strength and high energy absorption capacity. Most of the studies related to HPFRCC investigated the behavior of HPFRCCs in quasi-static loading condition. However, for high impact loading scenario, the composite is subjected to dynamic or seismic condition where the deformation of the composite material is at very high velocity or high strain-rate conditions meaning the results from the quasi-static loading condition is invalid. There are also many studies which concern for direct tensile and compressive behaviors at high strain rate. Cadoni uses Modified Hopkinson bar (MHB) experiment on varieties of fiber reinforce concrete samples and found that the tensile strength is significantly increased with the increase of strain-rate from $50s^{-1}$ to 200 s^{-1}. (Cadoni, Meda, & G.A., 2009) Mechtcherine also uses high rate MTS hydraulic testing machine to investigate the tensile behavior of PVA fiber reinforce composite at strain rate up to $50s^{-1}$ and finds

significant improvement in tensile strength and strain-hardening behavior. (Mechtcherine, Silva, Butler, Zhu, & Mobasher, 2011)

Comite Euro-International du Beton a guideline for designs of structures subjected to impact and explosion which includes equations to predict DIFs for post-cracking tension and compression for normal concrete. The correlation between DIF and strain rate for concrete in tension and compression is in accordance with the equation proposed by Malvar and Crawford (L. J. Malvar & J. E. Crawford, 1998)where the quasi-static strain rate is 1.E-06 s^{-1} and the gradient of the curve suddenly increases at the strain rate of 1 s^{-1}. The proposed equation by Malvar and Crawford is as shown in equation 2.4.2-1 and 2.4.2-2 for tensile load and compressive load respectively. (Tran & Kim, 2014)

$$DIF_{ft} = \left(\frac{\dot{\varepsilon}}{\dot{\varepsilon}_s}\right)^{\delta} \quad \text{for} \quad \dot{\varepsilon} \le 1s^{-1} \qquad (2.4.2\text{-}1.1)$$

$$DIF_{ft} = \beta\left(\frac{\dot{\varepsilon}}{\dot{\varepsilon}_s}\right)^{1/3} \quad \text{for} \quad \dot{\varepsilon} > 1s^{-1} \qquad (2.4.2\text{-}1.2)$$

$$DIF_{fc} = \left(\frac{\dot{\varepsilon}}{\dot{\varepsilon}_s}\right)^{1.026\alpha_s} \quad \text{for} \quad \dot{\varepsilon} \le 30s^{-1} \qquad (2.4.2\text{-}2.1)$$

$$DIF_{fc} = \gamma_s\left(\frac{\dot{\varepsilon}}{\dot{\varepsilon}_s}\right)^{1/3} \quad \text{for} \quad \dot{\varepsilon} > 30s^{-1} \qquad (2.4.2\text{-}2.2)$$

Where:

DIF_{fc}	=	Dynamic compressive strength at $\dot{\varepsilon}$
DIF_{ft}	=	Dynamic tensile strength at $\dot{\varepsilon}$
$\dot{\varepsilon}_s$	=	Static strain rate of 1.e-06 s^{-1}
$\log(\gamma_s)$	=	$6.156\alpha_s - 2$
α_s	=	$1/(5+9f_c^{'}/f_{co}^{'})$
$\log(\beta)$	=	$6\delta - 2$
δ	=	$1/(1+8f_c^{'}/f_{co}^{'})$

$f_c^{'}$ = static compression strength

$f_{co}^{'}$ = 10Mpa

From the study of Tuan, Strain Energy Frame Impact Machine (SEFIM) was used to generate high impact pulse allowing an application of high strain rate deformation into the test specimens. Tuan used the machine to investigate the DIFs for tensile strength of SFRC. The experiment was conducted for hooked-type and twisted-type deformed steel fiber, two fiber volume percentages of 1% and 1.5%, and two cement composite strength of 56Mpa and 81Mpa. Stress-strain curves for static and high strain-rate condition were obtained and investigated. The result was used to modify the DIF equations suggested by CEB. By applying curve-fitting to the experimental data, the study proposed modified equations as shown by equation 2.4.2-3. The equations took into account effects of fiber type and different in concrete strength by introducing new parameters m, h, and k; m=0.75, h=1, and k=1 for hooked-type fiber; h=1.3, and k=0.8 for twisted-type fiber. (Tran & Kim, 2014)

$$DIF_{ft} = \left(\frac{\dot{\varepsilon}}{\dot{\varepsilon}_s}\right)^{h\delta} \quad \text{for} \quad \dot{\varepsilon} \le 1s^{-1} \qquad (2.4.2\text{-}2.1)$$

$$DIF_{ft} = \beta\left(\frac{\dot{\varepsilon}}{\dot{\varepsilon}_s}\right)^{k/3} \quad \text{for} \quad \dot{\varepsilon} > 1s^{-1} \qquad (2.4.2\text{-}2.2)$$

Where,

$\log(\beta)$ = $6h\delta - 2$

δ = $1/(1+8mf_c^{'}/f_{co}^{'})$

Figure 2.4.2-1 shows DIF for Hooked-type fiber on the left-hand side and twisted-type fiber on the right-hand side; the white and black dots represent 1.5% and 1% fiber volume percentages respectively. The figure shows that an increase of fiber volume percentage from 1% to 1.5% resulted in strain rate sensitivity reduction for post-cracking strength, strain capacity and peak toughness of the test specimens. This

behavior may be explained by the fiber group effect studied by Naaman which is when a group of fiber is clumped together, thus pulling out a group of fiber is not as rate sensitive as pulling out a single fiber from concrete, because the amount of concrete surrounding a single fiber is less for larger fiber volume percentage. The experiment results also show that the increase in matrix strength leads to higher strain rate sensitivity.

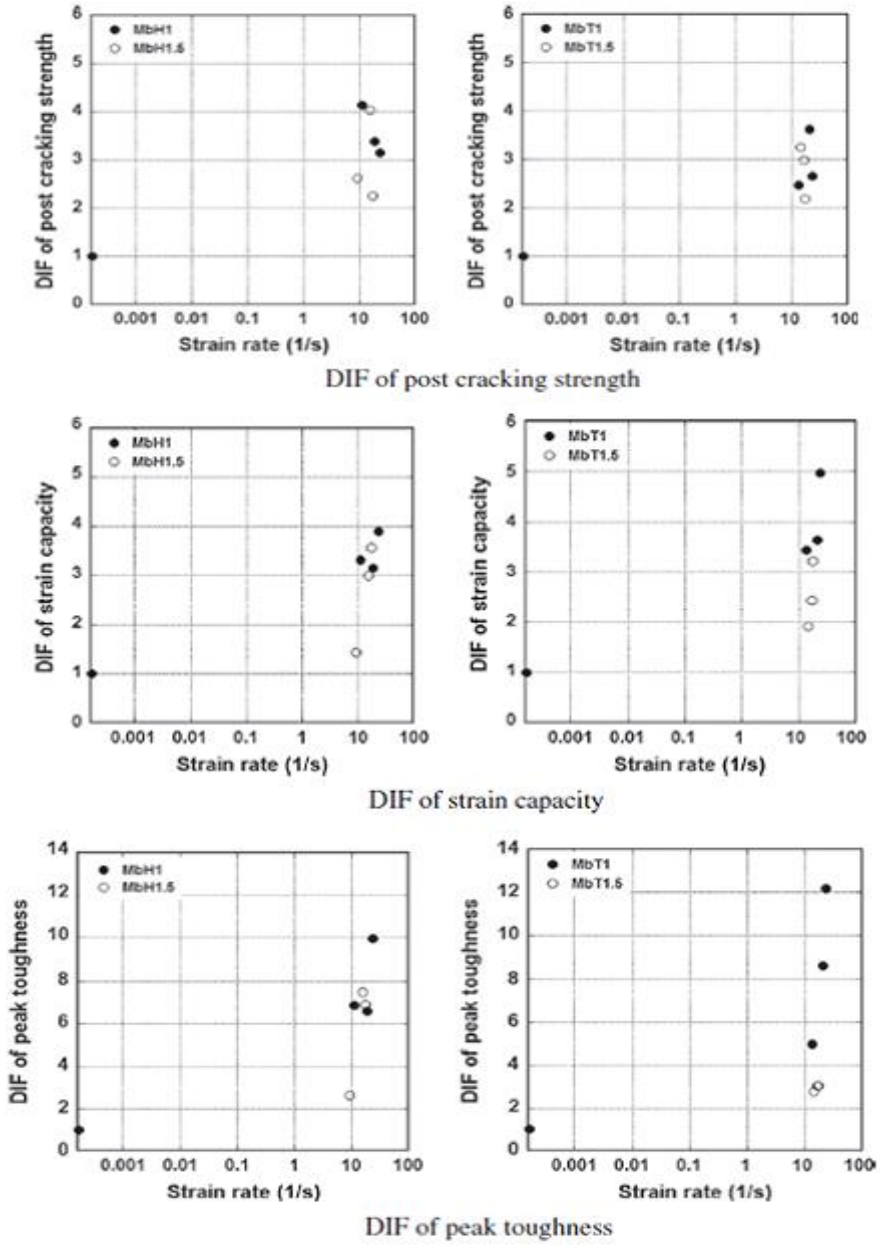

Figure 2.4.2-1 Strain rate sensitivity with increase of fiber percentage (Tran & Kim, 2014)

2.4.3 Strain rate effect on steel rebars

Malva and Crawford compiled sets of data from dynamic tensile tests for steel rebar from many sources to determine static and dynamic characteristic of most types of steel reinforcing rebar. A formulation was proposed for steel rebar with yield stresses between 290 and 710 MPa and for strain rates between 10^{-4} and 225 s^{-1}. The author proposed that DIF for steel rebar may be calculated by equation 2.4.3-1 (J. L. Malvar & E. J. Crawford, 1998)

$$DIF = \left(\frac{\dot{\varepsilon}}{10^4} \right)^{\alpha} \qquad (2.4.3\text{-}1)$$

For yield stress

$$\alpha_{fy} = 0.074 - 0.040 \frac{f_y}{414}$$

For ultimate stress

$$\alpha_{fu} = 0.019 - 0.009 \frac{f_y}{414}$$

Where

f_y = yield stress with unit of MPa

2.5 Finite Element Analysis (FEA) Modelling

2.5.1 Finite element modeling steps

Step1 Discretization

This step is a process of dividing each part into finitely small elements connected by nodes. All elements and nodes are numbered and labeled where each element with respective nodes has individual matrix of connectivity

Step 2 Element analysis

In this step, displacement at nodes may be computed while equilibrium of all elements forming the problem must remain in equilibrium where compatibility and stress-strain relation must be satisfied. The computation usually occur only at nodal points where element interpolating functions determine analysis results between nodes. Relationship between the nodal displacement and force may be given as shown in equation 2.5.1-1. Element types commonly used by FEA computer program are as shown in the figure 2.5.1-1

$$F = ku + F^0 \qquad (2.5.1\text{-}1)$$

Where

F = nodal point force

k = element stiffness matrix

u = nodal point displacement

F^0 = elemental nodal point force or equivalent point force

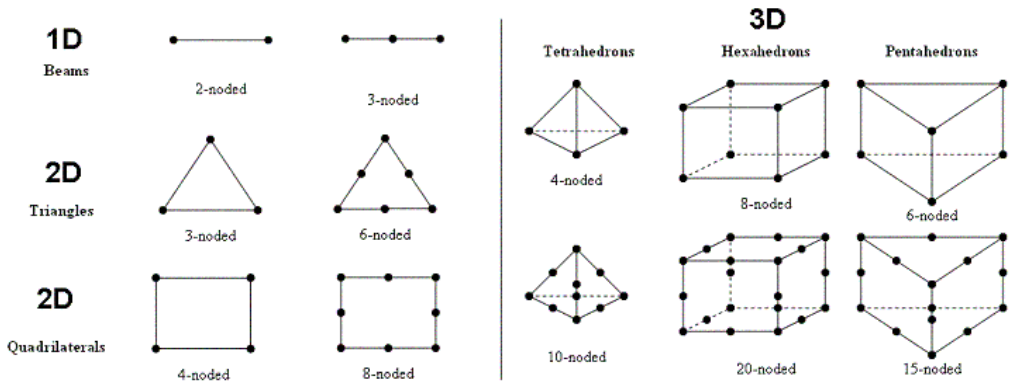

Figure 2.5.1-1 Commonly used element types in FEA modelling

Step3 System analysis

Results of the problem is computed with a requirement that all elements and nodes in the problem or system are in equilibrium at all times. The equilibrium equation is $R = Kr + R^0$ where R is system modal force , K is system stiffness matrix, R^0 is initial system model force, and r is displacement vector. K is a stiffness matrix calculated as $K = \sum_j^N a_j^T k_j a_j$ where j is element number, N is total number of element, k_j is elemental stiffness and a_j is element transformation matrix.

Step 4 Boundary condition

In most problems, initial displacement is known at some nodal points. This may be accounted by setting nodal displacements at the nodal points to be known variables before the process of system analysis.

Step 5 Post processing

This is a step for computation of internal forces and displacement at all nodes or between nodes. The finding of internal forces or stress in elements is done by back substitution of nodal displacement results from the analysis into elemental compatibility equations.

2.5.2 Damaged Plasticity Model (DPM) for concrete

In the case of blast load, structural elements are subjected to an impulse or high intensity short duration loading. The elements tend to deflect while absorbing the blast load and, if not exhibit instant failure, bounce back toward original orientation

due to remaining element elastic modulus. In most of the blast events, the blast duration is shorter than the natural frequency of the structural element allowing the element to freely exhibit cyclic deformation before finally become stationary with respective residual or permanent deformation. In the case where element natural frequency is longer than the blast duration, the time where the bouncing of the element occurs may coincide with the suction from negative phase of the blast load and greatly affects the behavior of the element after the first cyclic deformation.

ABAQUS provides a material model which is able to simulate the behavior of concrete and other quasi-brittle materials subjected to monotonic, cyclic, and/or dynamic loading. The model adopt the concepts of isotopic damaged elasticity and isotopic tensile and compressive plasticity to represent the plastic behavior of concrete matrix. Concrete is assumed to be at low confining pressure where cracks can freely propagate, thus mainly exhibits cracking in tension and crushing in compression. (Hibbitt, Karisson, & Sorensen, 2008)

The model requires strain rate decomposition from the field output which is assumed to be the total strain rate of the elastic strain rate and plastic strain rate. The stress strain relations may be expressed by equation 2.5.2-1.

$$\sigma = (1+d)D_0^{el} : (\varepsilon - \varepsilon^{pl}) = D^{el} : (\varepsilon - \varepsilon^{pl}) \qquad (2.5.2\text{-}1)$$

Which means that scalar damaged plasticity governs the relation. D_0^{el} represents undamaged elastic stiffness of the material while D^{el} represent damaged or degraded elastic stiffness equivalent to $(1-d)D_0^{el}$ where d is a scalar quantity representing stiffness degradation. d ranges from 0 to 1 where 0 means no damage and 1 means completely damaged. The isotropic stiffness degradation is, therefore, represented by a scalar variable d and thus the effective stress is defined as equation 2.5.2-2

$$\bar{\sigma} \overset{def}{=} D_0^{el} : (\varepsilon - \varepsilon^{pl}) \qquad (2.5.2\text{-}2)$$

The Cauchy stress σ is then a function of effective stress $\bar{\sigma}$ and scalar degradation d which can be resented as equation 2.5.2-3

$$\sigma = (1-d)\bar{\sigma} \qquad (2.5.2\text{-}3)$$

Thus, in terms of effective stress $\bar{\sigma}$, the yield condition takes the form as shown in equation 2.5.2-4

$$F(\bar{\sigma}, \tilde{\varepsilon}^{pl}) = \frac{1}{1-\alpha}\left(\bar{q} - 3\alpha\bar{p} + \beta\left(\tilde{\varepsilon}^{pl}\right)\left\langle\hat{\bar{\sigma}}_{\max}\right\rangle - \gamma\left\langle-\hat{\bar{\sigma}}_{\max}\right\rangle\right) - \bar{\sigma}_c\left(\tilde{\varepsilon}_c^{pl}\right) \le 0 \quad (2.5.2\text{-}4)$$

Where α and γ are dimensionless material constants and $\bar{p} = -\bar{\sigma}/3 : I$ is a hydro static pressure, $\bar{q} = \sqrt{3/2\bar{S} : \bar{S}}$ is the Mises equivalent effective stress, $\bar{S} = \bar{p}I + \bar{\sigma}$ is the deviatoric part of the effective stress tensor $\bar{\sigma}; \hat{\bar{\sigma}}_{\max}$ is algebraically maximum value of $\bar{\sigma}$; where the function of $\beta\left(\tilde{\varepsilon}^{pl}\right)$ is given as shown in equation 2.5.2-5.

$$\beta\left(\tilde{\varepsilon}^{pl}\right) = \frac{\bar{\sigma}_c\left(\tilde{\varepsilon}_c^{pl}\right)}{\bar{\sigma}_t\left(\tilde{\varepsilon}_t^{pl}\right)}(1-\alpha) - (1+\alpha) \qquad (2.5.2\text{-}5)$$

Where $\bar{\sigma}_c$ and $\bar{\sigma}_t$ are the effective compressive and tensile stresses, respectively. The DPM assume nonassociated potential flow, $\dot{\varepsilon}^{pl} = \dot{\lambda}\frac{\partial G(\bar{\sigma})}{\partial(\bar{\sigma})}$ where the flow potential function G is the Ducker-Prager hyperbolic function as shown in equation 2.5.2-6 where φ is dilation angle measured in the p-q plane at high confining pressure, σ_{t0} is uniaxial tensile stress at failure, and ε is eccentricity coefficient defining the rate at which the function approaches the asymptote.

$$G = \sqrt{\left(\varepsilon\sigma_{t0}\tan\varphi\right)^2 + \bar{q}^2} - \bar{p}\tan\varphi \qquad (2.5.2\text{-}6)$$

The continuous and smooth flow potential ensures that the flow direction is defined uniquely; the flow function asymptotically approached the linear Ducker-Prager flow potential at high confining pressure and intersects the hydrostatic pressure at 90 degree angle. The use of concrete model requires the solution of nonsymmetrical equations because the plastic flow is non-associated. The uniaxial stress-strain curves can be converted to stress versus plastic strain curves of the form as shown in equation 2.5.2-7 and 2.5.2-8 for tension and compression respectively.

$$\sigma_t = \sigma_t\left(\tilde{\varepsilon}_t^{pl}, \dot{\tilde{\varepsilon}}_t^{pl}, \theta, f_i\right) \qquad (2.5.2\text{-}7)$$

$$\sigma_c = \sigma_c\left(\tilde{\varepsilon}_c^{pl}, \dot{\tilde{\varepsilon}}_c^{pl}, \theta, f_i\right) \qquad (2.5.2\text{-}8)$$

Where $\tilde{\varepsilon}_t^{pl}$ and $\tilde{\varepsilon}_c^{pl}$ are equivalent plastic strain rate in tension and compression respectively; $\tilde{\varepsilon}_t^{pl} = \int_0^t \dot{\tilde{\varepsilon}}_t^{pl} dt$ and $\tilde{\varepsilon}_c^{pl} = \int_0^t \dot{\tilde{\varepsilon}}_c^{pl} dt$ are equivalent plastic strain in tension and compression; θ is the temperature, and $f_i\left(i = 1, 2, ...\right)$ are other predefined field variables. For uniaxial loading conditions, the effective plastic strain rates are given as $\dot{\tilde{\varepsilon}}_t^{pl} = \dot{\tilde{\varepsilon}}_{11}^{pl}$ in uniaxial tension and $\dot{\tilde{\varepsilon}}_c^{pl} = \dot{\tilde{\varepsilon}}_{11}^{pl}$ in uniaxial compression σ_c is a positive quantity which represents the magnitude of uniaxial compression stress, $\sigma_c = \sigma_{11}$.

As shown in figure 2.5.2-1 and 2.5.2-2, when the concrete material is unloaded from any point on the strain softening part of the curve, the elastic stiffness is weaken due to the scalar damage d_t or d_c. The degradation of the elastic stiffness is significantly different in tension and compression tests. The degraded response of concrete is characterized by two independent uniaxial damage variables d_t and d_c, which are assumed to be functions of the plastic strain, temperature and field variable. d_t and d_c may be represented by equation 2.5.2-9 and 2.5.2-10 respectively

$$d_t = d_t\left(\tilde{\varepsilon}_t^{pl}, \theta, f_i\right), \left(0 \le d_t \le 1\right) \qquad (2.5.2\text{-}9)$$

$$d_c = d_c\left(\tilde{\varepsilon}_c^{pl}, \theta, f_i\right), \left(0 \le d_c \le 1\right) \qquad (2.5.2\text{-}10)$$

If E_0 is undamaged elastic stiffness of the material, the stress-strain relations under uniaxial tension and compression loading are as shown in equation 2.5.2-11 and 2.5.2-12 respectively.

$$\sigma_t = (1-d_t)E_0\left(\varepsilon_t - \tilde{\varepsilon}_t^{pl}\right) \quad (2.5.2\text{-}11)$$

$$\sigma_c = (1-d_c)E_0\left(\varepsilon_c - \tilde{\varepsilon}_c^{pl}\right) \quad (2.5.2\text{-}12)$$

Under uniaxial loading, cracks propagate in a direction transverse to the stress direction. The nucleation and propagation of cracks, therefore, causes a reduction of the available load-carrying area, which in turn leads to an increase in the effective stress. The effect is less pronounced under compressive loading since cracks run parallel to the loading direction; however, after a significant amount of crushing, the effective load-carrying area is also significantly reduced. The effective uniaxial cohesion stresses are given as equation 2.5.2-13 and 2.5.2-14

$$\bar{\sigma}_t = \frac{\sigma_t}{(1-d_t)} = E_0\left(\varepsilon_t - \tilde{\varepsilon}_t^{pl}\right) \quad (2.5.2\text{-}13)$$

$$\bar{\sigma}_c = \frac{\sigma_c}{(1-d_c)} = E_0\left(\varepsilon_c - \tilde{\varepsilon}_c^{pl}\right) \quad (2.5.2\text{-}14)$$

The effective uniaxial cohesion stresses determine the size of yield surface. Material models exhibiting softening behavior and stiffness degradation often lead to severe convergence difficulties in implicit analysis programs. Some of these convergence difficulties can be overcome by using a viscoplastic regularization of the constitutive equations. The concrete damaged plasticity model can be regularized using viscoplasticity, therefore, permitting stresses to be outside of the yield surface. DPM uses a generalization of the Duvaut-Lions regularization, according to which the viscoplastic Under uniaxial loading, $\dot{\tilde{\varepsilon}}_v^{pl}$, is defined as equation 2.5.2-15

$$\dot{\tilde{\varepsilon}}_v^{pl} = \frac{1}{\mu}(d - d_v) \quad (2.5.2\text{-}15)$$

Here μ is the viscosity parameter representing the relaxation time of the viscoplastic system and ε^{pl} is the plastic strain evaluated in the inviscid backbone model. Similarly, a viscous stiffness degradation variable $\dot{d}_v$, for the viscoplastic system is defined as equation 2.5.2-16

$$\dot{d}_v = \frac{1}{\mu}\left(d - d_v\right) \qquad (2.5.2\text{-}16)$$

Where d is the degradation variable evaluated in the inviscid backbone model. The stress-strain relation of the viscoplastic model is given as equation 2.5.2-17

$$\sigma = \left(1 - d_v\right) D_0^{el}\left(\varepsilon - \varepsilon_v^{pl}\right) \qquad (2.5.2\text{-}17)$$

The solution of the viscoplastic system relaxes to that of the inviscid case as ration between time and viscosity parameter t/μ approaches infinity. Using the viscoplastic regularization with a small value for the viscosity parameter, which is small compared to the characteristic time increment, usually helps improve the rate of convergence of the model in the softening regime, without compromising results.

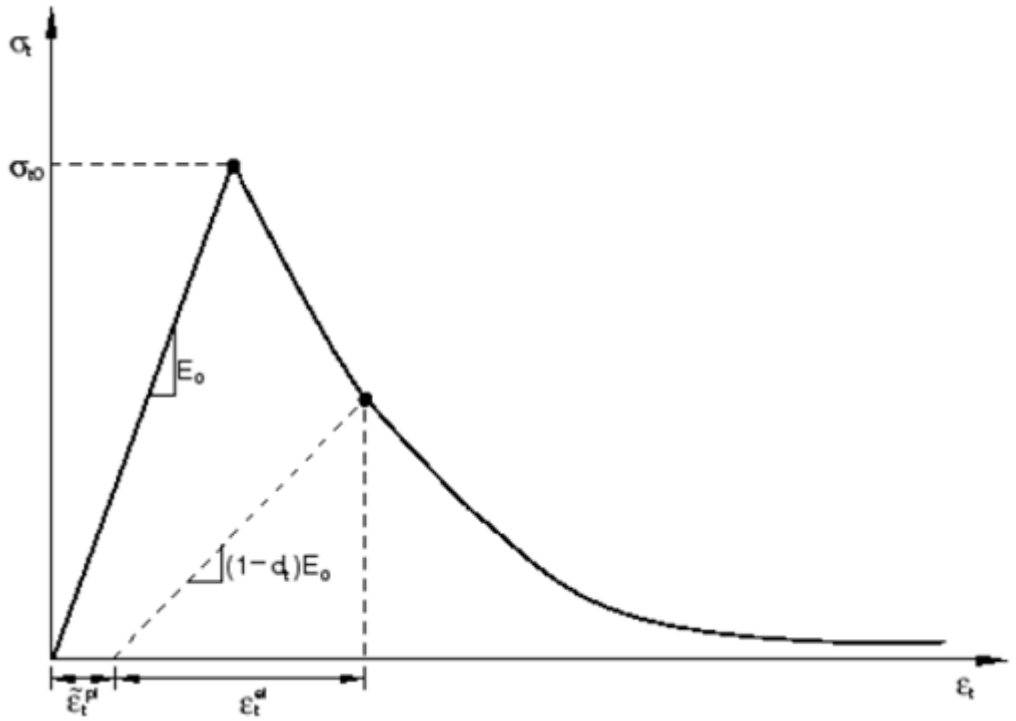

Figure 2.5.2-1 Uniaxial tension stress-strain curve. (Hibbitt et al., 2008)

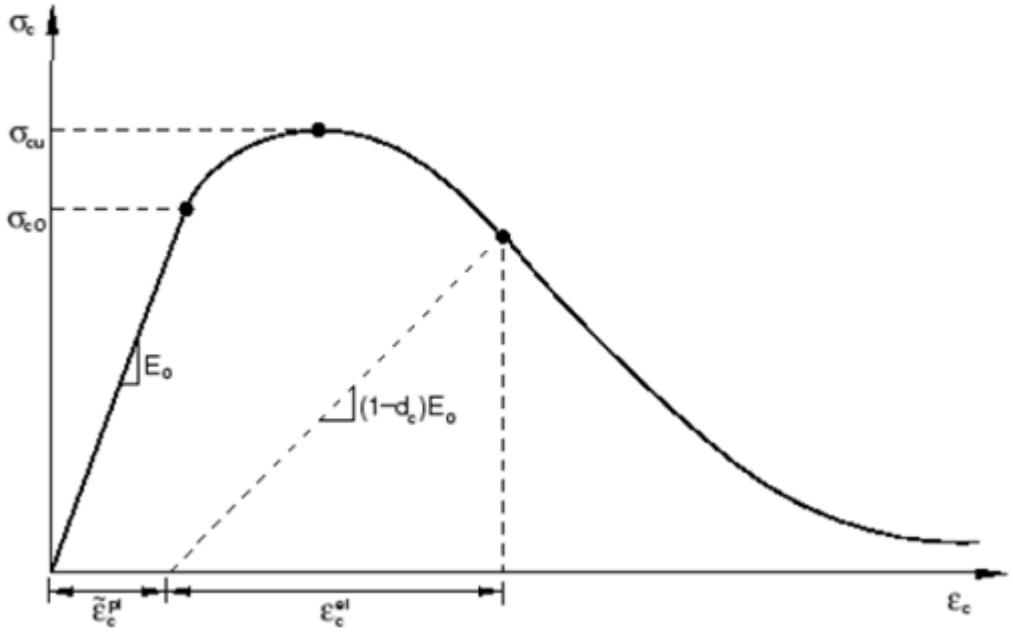

Figure 2.5.2-2 Uniaxial compression stress-strain curve. (Hibbitt et al., 2008)

2.5.3 Johnson-cook constitutive model for steel

Johnson-cook (JC) model is a constitutive model for most of the ductile materials subjected to large strain, high strain rate and high temperature. JC model is commonly used in FEA simulations due to simplicity and robustness. The model for the von Mises flow stress (σ) may be expressed as shown in equation 2.5.3-1 where, $\in$ is equivalent plastic strain, $\dot{\epsilon}^* = \dot{\epsilon}/\dot{e}_0$ is dimensionless plastic strain rate, and T^* is homologous temperature calculated as $(T - T_{room})/(T_{melt} - T_{room})$.

$$\sigma = \left[A + B \in^n\right]\left[1 + C \ln \dot{\epsilon}^*\right]\left[1 - T^{*m}\right] \qquad (2.5.3\text{-}1)$$

The parameters A, B, n, C, and m are material parameters, where A is yield stress, B and n represent strain hardening behavior, and C is strain rate constant. These material parameters are readily available in many published paper for most of the commonly used materials for reinforced concrete

Johonson-Cook material model is readily available within ABAQUS as built in property module with minor different where the notations T^* is replaced by θ (Hibbitt et al., 2008)

CHAPTER 3 **Experiment studies**

To investigat the effect from inclusion of steel fiber, specimens casted from normal reinforced concrete (NRC) and specimens casted from steel fiber reinforced concrete (SFRC) with weight ratio of 30kg/m^3 were tested and compared; also, to investigate the effect from increasing amount of steel fiber, specimens casted from (SFRC) with weight ratio of 60kg/m^3 were also tested and compared. It was sensible to apply appropriate blast load magnitudes such that the level of damage would be high enough to give meaningful results, thus two explosive weights of 1lb and 2lb were considered in this experiment. In total, there were two varying parameters for this experiment which were 3 fiber weight ratio of 0, 30, and 60 kg/m^3; as well as 2 explosive weights of 1 and 2 lb. This means 2 NRC specimens and 4 SFRC specimens were casted and tested under blast load to satisfy all varying parameters. Since steel fiber enhanced concrete elements greatly in flexural tensile capacity. Several preliminary FEA models in ABAQUS were made and adjusted to decide for appropriate element geometries and steel reinforcement configuration so that the failure mode was flexural. The specimen geometry and steel reinforcement detail were decided to be the same as that used in the work of Tanapornraweekit, Haritos, and Ngo; the reinforcement layout was RB6@225 for main longitudinal reinforcement and RB6@300 for transverse reinforcement with additional longitudinal rebar of RB6@115 as shown in figure 3-1. Note that the panel-type geometry of 2000x1000x75thkmm was chosen to avoid the effect from reflection of blast from the ground which may happen when the area of the test specimen receiving the blast pressure was too small causing some parts of the blast waves to be reflected with the ground causing additional blast pressure on the bottom side of the panel.

Panels were named according to their steel fiber weight ratio and subjected blast weight as shown in Table 3-1. For example, 30SF2LB means the specimen was casted from steel fiber reinforced concrete with 30kg/m^3 steel fiber weight ratio. Note

here that the maximum fiber weight ratio of 60kg/m^3 was a maximum amount suggested by the manufacturer.

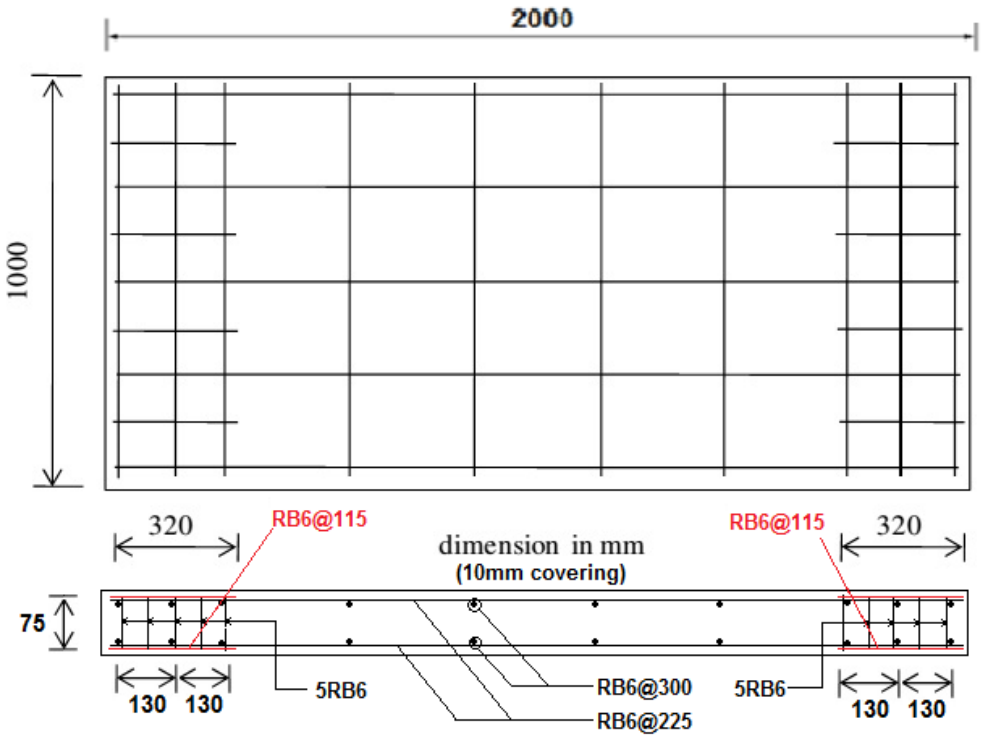

Figure 3-1 Panel geometry and steel reinforcement detail (Tanapornraweekit, Haritos, Mendis, & Ngo, 2010)

Specimen name		NRC1LB	NRC2LB	30SF1LB	30SF2LB	60SF1LB	60SF2LB
concrete compressive strength (fc')		55 MPa		60 MPa		56 MPa	
steel reinforcement strength	grade	SR24					
	yield	305 MPa					
	Ultimate	440 MPa					
steel fiber	length (L)	30 mm					
	diameter (D)	0.38 mm					
	aspect ratio (L/D)	80					
	weight fraction	0 kg/m3		30 kg/m3		60kg/m3	
explosive weight (lb)		1	2	1	2	1	2

Table 3-1 Specimen details

3.1 Setting up of experiment

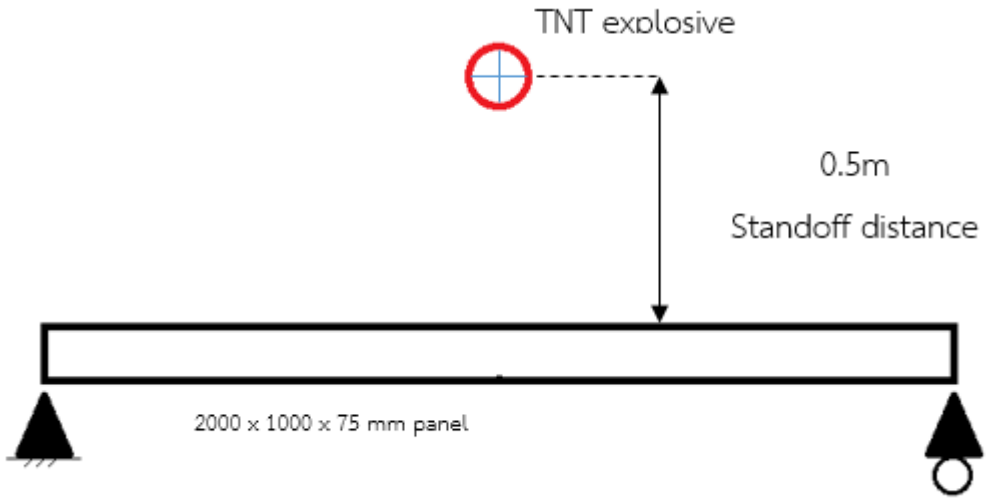

Figure 3.1-1 Overall experiment setup

The test was idealized as shown in figure 3.1-1 where each test panel with dimension of 2000 x 1000 x 75 mm is simply supported and subjected to a TNT explosive hung at fixed 0.5m standoff distance.

Figure 3.1-2 Steel rig supporting test specimens

A solid steel frame rig made out of steel sections, as shown in figure 3.1- 2, was used as a support for the test specimens. The rig was a modified version of that used in the study of Wu, Oehler, Rebentrost, Leach, and Whittaker. (Wu, Oehlers, Rebentrost, Leach, & Whittaker, 2009) The rig was made mainly from steel H-sections; bracing beams were made of 150x75 H-sections; the 6 columns were made of 150x150 H-sections. All components were assembled by nuts and bolts. In order to prevent possible vertical translations or up-lift of the test panels, two 100x100x10 mm steel angles were bolted together to form a C-section support as shown in figure 3.1-3. The C-section still allow support rotation during the movement response of the panel. The test rig was bolted down on each of the six supporting legs to the hooks embedded into the casted foundation as shown in figure 3.1-4 and 3.4-5. The foundations were heavy 1500x500x300 band beams with 4 of DB26 for top and bottom longitudinal reinforcement and DB6@200 for stirrup as shown in figure 3.1-6. The foundations were casted with high early strength 400ksc self-compacted concrete to shorten the site preparation procedure.

The experiment setup for all six trials was kept the same. In each test, a panel was placed then the steel angles were bolted together on both side to form the C-section supports locking the test panel in place on both supporting sides. Blast load was produced from a standard bar shape TNT with a size of 44.45 x 44.45 x 177.8 mm with TNT weight of 1 lb; two 1lb TNT bars were tied together to form a 2lb blast load for respective blast trials as shown in figure 3.1-7. The TNT bars were carefully suspended at a fix 500mm standoff distance by a one-time-use PVC pipe hanger placed on the test panel. To ensure that the TNT explosive is hung right in the middle of the panel, a pendulum was used to finely move the PVC hanger as shown in figure 3.1-8. A pictorial representation of a finished test setup for each of the six test trials is as shown in figure 3.1-9.

Figure 3.1-3 C-section made of assembled 100 x 100 x 10 mm steel angle

Figure 3.1-4 Steel hook embedded in the foundation

Figure 3.1-5 Bolted support after casting of concrete

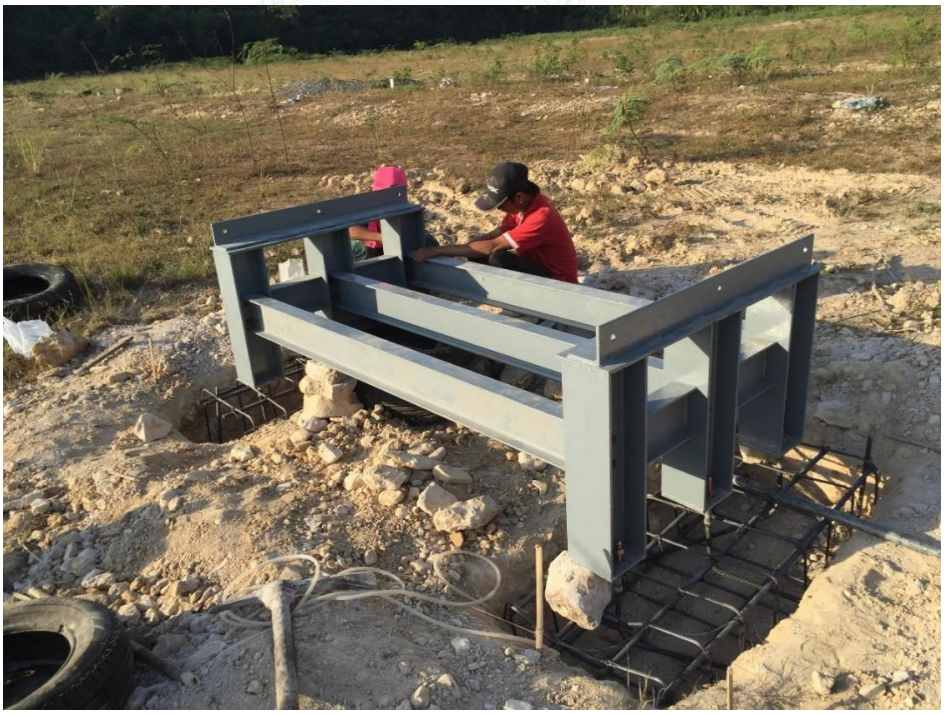

Figure 3.1-6 Steel cage in the foundation formwork

Figure 3.1-7 Two of 1lb TNT explosive tied together to form a 2lb loading

Figure 3.1-8 Use of pendulum to ensure that the explosive is right above the center of the panel

Figure 3.1-9 Test setup for each test trial

3.2 Casting of panels

The test panels were all casted with self-compacting ready-mixed concrete. The NRC panels were casted by pouring concrete directly from the concrete truck into the formwork while the SFRC panels first required the concrete to be mixed with the steel fiber in a mixer before later casted into the formworks.

Two of the four SFRC panels were casted with 30kg/m^3 fiber weight ratio and the other two with 60kg/m^3 fiber weight ratio. Since the workability of the concrete was significantly reduced after mixing in the steel fibers, casting trials were conducted before the actual casting of SFRC panels in order to find the most appropriate concrete pre-mixed slump for both fiber weight ratios. The trials were done to prevent inappropriate workability of the concrete after mixing in the steel fiber. Appropriate pre-mix slump flow diameters were found being 45 cm for 30kg/m^3 fiber weight ratio and 60 cm for 60kg/m^3 fiber weight ratio; the final slump was approximately 15 cm for both fiber weight ratios. Note that, the NRC panels were casted with the same ready mix concrete as that for SFRC panels with 60 kg/m^3 weight ratio.

Casting procedures for SFRC panels are as following

- The formworks and steel cages were prepared at the casting site along with a high speed 80 liter mortar mixer as shown in figure 3.2-1

Figure 3.2-1 Form works and mortar mixer prepared at the site

- The concrete truck was then arrive at the site; a slum-flow check was then conducted to ensure required slump flow as shown in figure 3.2-2.

Figure 3.2-2 Pre-mix slump flow check

- After the slump was verified, 80 liters of concrete together with the pre-weighted fiber were then poured into the prepared mixer and stirred at high speed for 5 minutes before another slump check to ensure final 15 cm slump was obtained. The thoroughly mixed SFRC was then casted into the formworks as shown in figure 3.2-3. Six compressive test cylinders were also collected for each of the three material types which are NRC, SFRC with 30 kg/m^3 fiber weight ratio, and SFRC with 60 kg/m^3 fiber weight ratio. This procedure was repeated until all panels and cylinders were all filled.

Figure 3.2-3 Casting of SFRC panels

- Casted panels were then wet cured for 28 days together with all collected cylinders as shown in Figure 3.2-4 and 3.2-5.

Figure 3.2-4 Wet cure and storage of casted panel

Figure 3.2-5 Wet cure and storage of cylinders

3.3 Material properties

Compressive strength tests were conducted on the concrete cylinders for 7-days and 28-days strength with method recommended by the standard ASTM C 39. Three trials of tensile strength test were also conducted on the RB6 steel rebar to obtain an actual yield and ultimate strength. A summary including all material details is shown in Table 3.3-1

denoted		NRC	30kg/m^3 SFRC	60kg/m^3 SFRC
28 days compressive strength		55 Mpa	60 Mpa	56 Mpa
7 days compressive strength		42 Mpa	40 Mpa	39 Mpa
steel reinforcement strength	yield	305 MPa		
	Ultimate	440 MPa		
steel fiber	length (L)	30 mm		
	diameter (D)	0.38 mm		
	aspect ratio (L/D)	80		
	weight fraction	0 kg/m3	30 kg/m3	60kg/m3

Table 3.3-1 Material properties acquired from tests

3.4 Panel responses measurements

There were three measurement types conducted in this experiment including residual deflection, panel acceleration, and high speed video recording.

The residual deflection was measure at 6 locations along the two long edges of each test panel after each blast trial; the locations were as shown in figure 3.4-1. Two antennas were also adapted in this experiment as shown in figure 3.4-2 to measure the maximum deflection. The antennas were casted straight up into concrete blocks then placed along the A-D and B-E lines as indicated in figure 3.4-1. The antennas contract during the downward movement of the panels, however, the antennas do not extend with the upward movement of the panel leaving a gap between the tips and the bottom surface of test panels. Maximum deflection calculated by adding the residual deflection with the measured gap size.

Acceleration response of the panel was recorded by installing an acceleration transducer at the center of the panel which was connected to a 50 kHz data logger buried and protected under the panel. The installation of the acceleration transducer was as shown in figure 3.4-3

A high speed camera Fastcam SA4, as shown in figure 3.4-3, was used to record video footages at the rate of 40000 frame per second. The camera was installed and protected at a safe distance of 150 m away from the explosion. The video footages were recorded with VGA resolution, giving a picture quality such that a pixel on the recorded footage was equivalence to 3.64x3.64 mm^2 square on the plane of the panel's edge facing the camera.

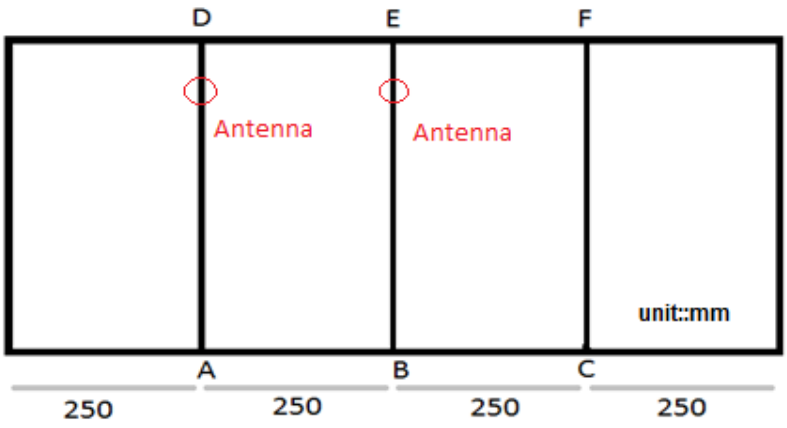

Figure 3.4-1 Location where displacement is measured and locations of the two antennas' tips

Figure 3.4-2 Antenna used for measurement

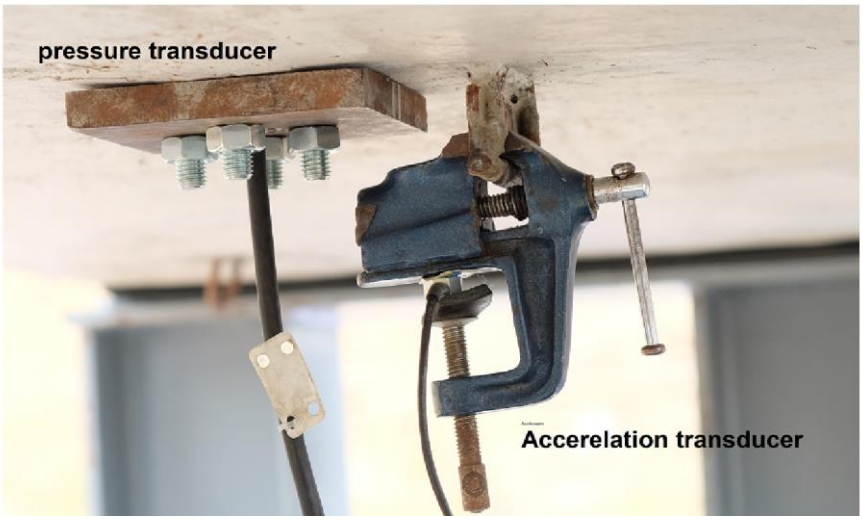

Figure 3.4-3 Installation of acceleration transducer

Figure 3.4-4 High speed camera Fastcam SA4

CHAPTER 4 ABAQUS Finite Element Analysis

4.1 FEA material modeling

4.1.1 Element type

Solid element

The solid element type in ABAQUS is denoted as C3D8. In each element, there are 8 nodes. Each node has three degrees of freedom which are translation in x, y, and z direction. The element contains homogeneous material which has linear and non-linear behavior. This element type was used to model the concrete part of both NRC and SFRC specimens.

Truss element

Truss element in ABAQUS is called T3D2 which has 2 nodes and each node has three degrees of freedom including translation in x, y, and z direction. The element is able to transfer only axial force but not the moment nor any forces perpendicular to the centerline of the element. This element type is normally used to model a slender element that is thin enough to be modelled as a line object. The steel rebars were modeled with this element type as they can transfer very little moment and forces perpendicular to the centerline. This element type may be used in both two and three dimensional analysis where displacement and position are computed by linear interpolation.

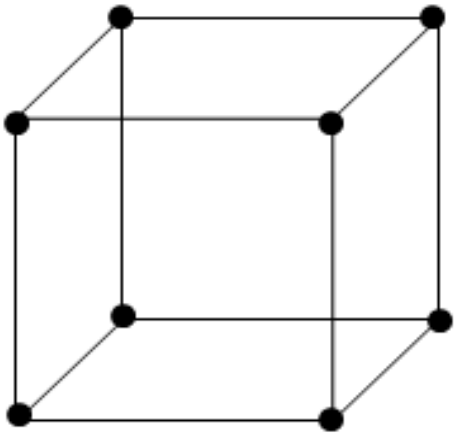

Figure 4.1.1-1 Solid element C3D8

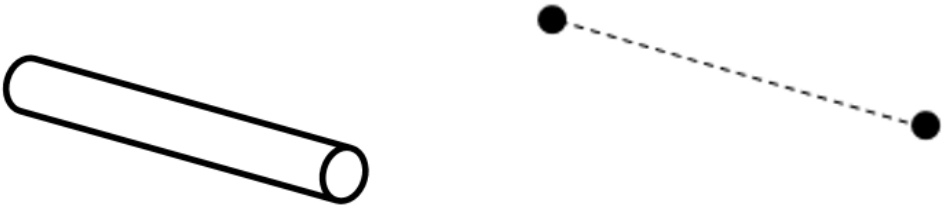

Figure 4.1.1-2 Truss element T3D2

4.1.2 Modeling of concrete with concrete damage plasticity model (CDP)

The cementitious matrix was modeled with the “Concrete Damage Plasticity” (CDP) material model which is readily available in ABAQUS. This model is based on the theory proposed by Drucker-Prager then later developed by Lubliner, Lee and Fenves. The model includes the effects from compressive behavior, tensile behavior, and damage condition of the material. The parameters used in model are as following.

1. K_c

Drucker-Pracker assume that the failure surface in the deviatoric cross section was a circle. Lublineae, Lee, and Fenves, improved this assumption by proposing that the deviatoric cross section was in fact not necessary a circle and the shape was govern

by parameter K_c. The parameter K_c was a ratio of the distance between the hydrostatic axis and respectively to the compression meridian and the tension meridian. When $K_c = 1$ means the deviatoric cross section of the failure surface becomes a circle as assumed by the classic Drucker-Pracked assumption. The value of 2/3 was recommended giving the shape similar to the strength criterion formulated by William and Warnke tri-axial test. The value of 2/3 was used for both RC and SFRC material modelling.

2. $\in$ (eccentricity)

The shape of the meridians in the stress space was found to be a curve and may be assumed as a hyperbola form. The shape of hyperbola was modified by the small positive parameter $\in$ which would affect the rate at which the plastic potential hyperbola approaches its asymptote. It was also said to be the distance from the intersection of the asymptotes of the hyperbola to the vertex of the hyperbola. The parameter $\in$ could be calculated as the ratio between tensile strength and compressive strength but it was recommended that a value of 0.1 should be used when $\in = 0$ or when the meridian plane was a straight line as assumed by Drucker-Pracker hypothesis.

3. $\sigma_{b0} / \sigma_{c0}$

It was a parameter describing the state of material when undergoing failure under biaxial compression. It was a ratio between the strength in biaxial state (σ_{b0}) and the strength in uniaxial state (σ_{c0}) which could be derived from the experiment. Kuple suggested a value of 1.16 which is equivalent to the default value specified by ABAQUS.

4. Dilation angle

Dilation angle is the angle between the failure surface and the hydrostatic axis measured in meridian plane. The angle could also be explained as concrete internal friction angle. This thesis would adopt a dilation angle of $31°$ as suggested by Malm.

5. Degradation Variable

There were two types of damage parameter which are the compressive damage parameter and tensile damage parameter ranging from 0 for undamaged material to 1 for fully damaged material or material with no load capacity. The damage parameter was defined as the ratio of the remaining stress from the declining part of the curve to the strength of concrete; this definition was applied for both compressive damage parameter and tensile damage parameter. Since there were no available sources for damage parameter especially in high strain rate condition, the input was omitted and default value was automatically used in the model; this means that the model would not be able to determine actual remaining strength of the material after being damaged by high strain which also means that the model is unable to predict the rebound behavior or residual deflection of the test panels.

The parameters used in concrete damage plasticity model were summarized in Table 4.1.2-1

Parameter used in CDP model				
Dilation angle	$\in$	$\sigma_{b0} / \sigma_{c0}$	K_c	Viscosity Parameter
31°	0.1	1.16	2/3	0

Table 4.1.2-1 Parameters used in concrete damage plasticity model

4.1.3 Stress-strain relationships used to model NRC and SFRC specimens

CDP model requires user to manually input stress-strain curves both for tension and compression as tabular data sets. The theories for NRC and SFRC stress-strain relationships are those included in literature review section 2.3.

Normal reinforced concrete in compression

As explained in section 2.3.1, a stress-strain relationship for NRC in compression was calculated according to the equation proposed by Popov Thorenfeldt, Tomaszewicz, and Jensen as written by equation 4.1.3-1

$$\frac{f_c}{f_c'} = \frac{n(\varepsilon_c / \varepsilon_0)}{n-1+(\varepsilon_c / \varepsilon_0)^{nk}} \qquad (4.1.3\text{-}1)$$

Relevant parameters were calculated as following

$$f_c' = 55MPa$$

$$E_c = 57{,}000\sqrt{f_c'} = 35101MPa$$

$$n = 0.8 + \left(\frac{f_c'}{2500}\right) = 4$$

$$\varepsilon_0 = \frac{f_c'}{E_c}\left(\frac{n}{n-1}\right) = 0.0021$$

This gives a stress strain curve for NRC which was used as a tabular data set for CDP model as shown in figure 4.1.3-1.

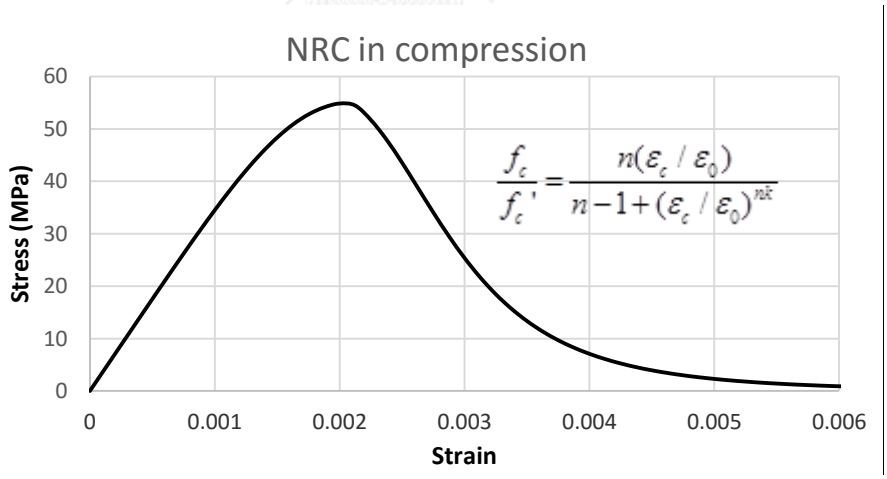

Figure 4.1.3-1 Stress-strain relationship of normal reinforced concrete in compression

Normal reinforced concrete in Tension

As explained in section 2.3.2, Stress-strain relationship for NRC in Tension was calculated according to the theory proposed by Wahalathantri, Thambiratnam and Chan with the tensile strength, $\sigma_{t0} = 0.3 f_{cu}^{2/3} = 0.3(55)^{2/3} = 4.34MPa$ and the strain

at maximum tensile strength, $\varepsilon_{cr} = \sigma_{t0} / E_c = 4.34 / 35101 = 0.000124$. Based on the information given in figure 2.3.2-3, a stress-strain curve was generated and used as a tabular data set for CDP model as shown in figures 4.1.3-2

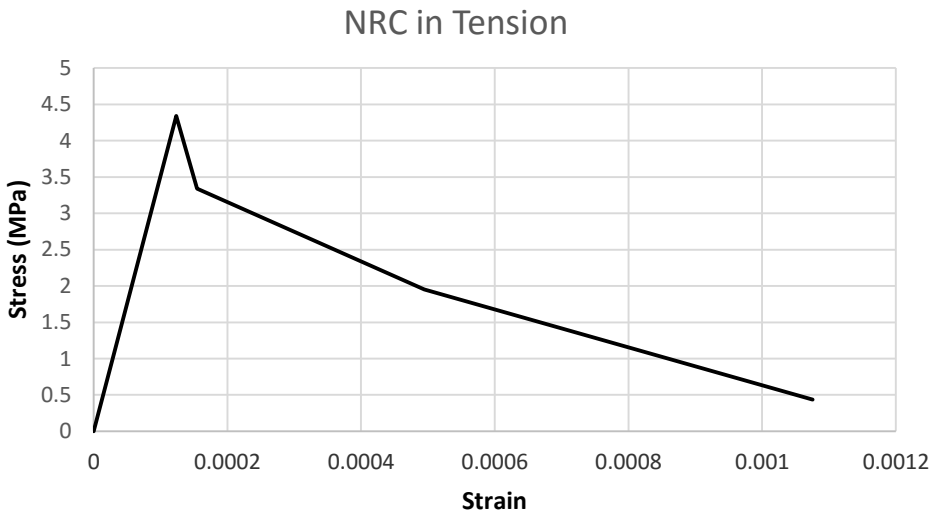

Figure 4.1.3-2 Stress-strain relationship of normal reinforced concrete in tension

Steel fiber reinforced concrete in compression

Stress-strain relationship for SFRC in compression was calculated according to the theory mentioned in the literature review section 2.3.3. The strain at peak compressive stress (ε_{cf}) was calculated by equation 2.3.3-1 while young modulus of SFRC (E_{cf}) was obtained from actual compressive tests with displacement controlled Universal Testing Machine (UTM). All relevant parameters were summarized for both fiber densities as shown in table 4.1.3-1. The whole stress-strain curve for each of the two fiber densities was then calculated using equation 2.3.3-3. The stress-strain curves for both SFRC with fiber density of 30kg/m^3 and 60kg/m^3 as shown in figure 4.1.3-3 were used as tabular data sets for CDP model.

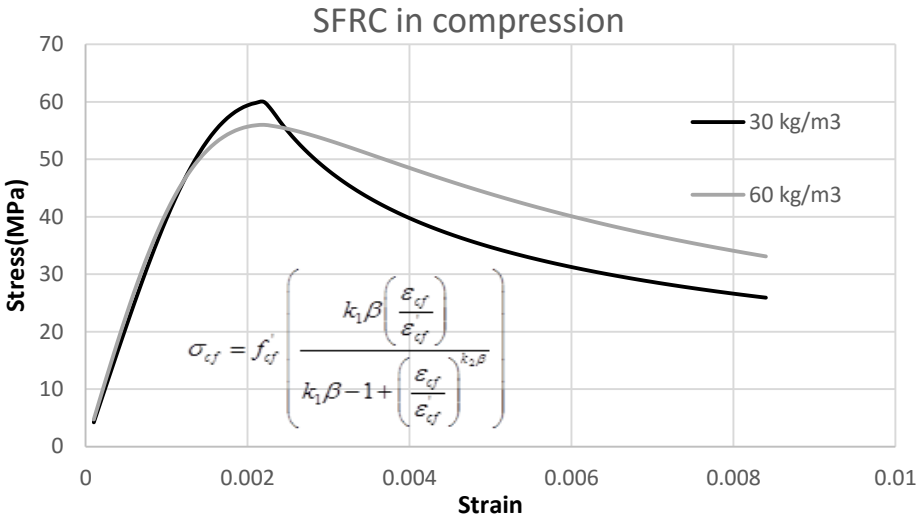

Figure 4.1.3-3 Stress-strain relationship for SFRC in compression

Table 4.1.3-1 Relevant parameters for SFRC compressive stress-strain curves

parameter	Acquirement	30SF	60SF	unit	description
w	Predefined	30	60	kg/m^3	Fiber weight density
$f_c^{'}$	Compressive test	57	55	MPa	Plain concrete compressive strength
$f_{cf}^{'}$	Compressive test	60	56	MPa	SFRC compressive strength
ρ_f	Defined by manufacturer	7850	7850	ρ_f	Fiber density
V_f	$V_f = w/\rho_f$	0.0038	0.0076	-	Fiber volume fraction
l_f	Predefined	30	30	mm	Fiber length
d_f	Predefined	0.375	0.375	mm	Fiber diameter
E_i	Material test by UTM	35400	38935	MPa	SFRC young modulus
$R.I.$	$V_f \frac{l_f}{D_f}$	0.31	0.61	-	Reinforcement index
ε_{cf}	$\varepsilon_{cf} = 0.69 f_{cf}^{'\left[0.29+0.0002V_f\left(l_f/d_f^2\right)\right]}$	0.00223	0.002209	-	Strain at peak stress
G	$31.82+16.39(R.I.)+9.35(R.I.)$	39.68	47.54	-	Theoretical factor
k_1	$\left(D/f_{cf}^{'}\right)^{3.79}$	0.30	0.74	-	Theoretical factor
k_2	$\left(G/f_{cf}^{'}\right)^{1.46}$	0.55	0.79	-	Theoretical factor
k_1, k_2		1	1	-	Theoretical factor
A	$50.35+22.31(R.I.)+19.13(R.I.)$	63.02	75.69	-	Theoretical factor
C	$2.04-0.313(R.I.)-0.155(R.I.)$	1.90	1.75	-	Theoretical factor
β	$\left(f_{cf}^{'}/A\right)^3+C$	2.76	2.16	-	Theoretical factor

Steel fiber reinforced concrete in tension

Stress-strain relationship for SFRC in tension was calculated according to the theory mentioned in the literature review section 2.3.4. All relevant parameters were summarized for both fiber densities as shown in table 4.1.3-2. The whole stress-strain curve for each of the two SFRC densities was then calculated using equation 2.3.4-1. The stress-strain curves for both SFRC with fiber density of 30kg/m^3 and 60kg/m^3 as shown in figure 4.1.3-3 are use as tabular data sets for CDP model.

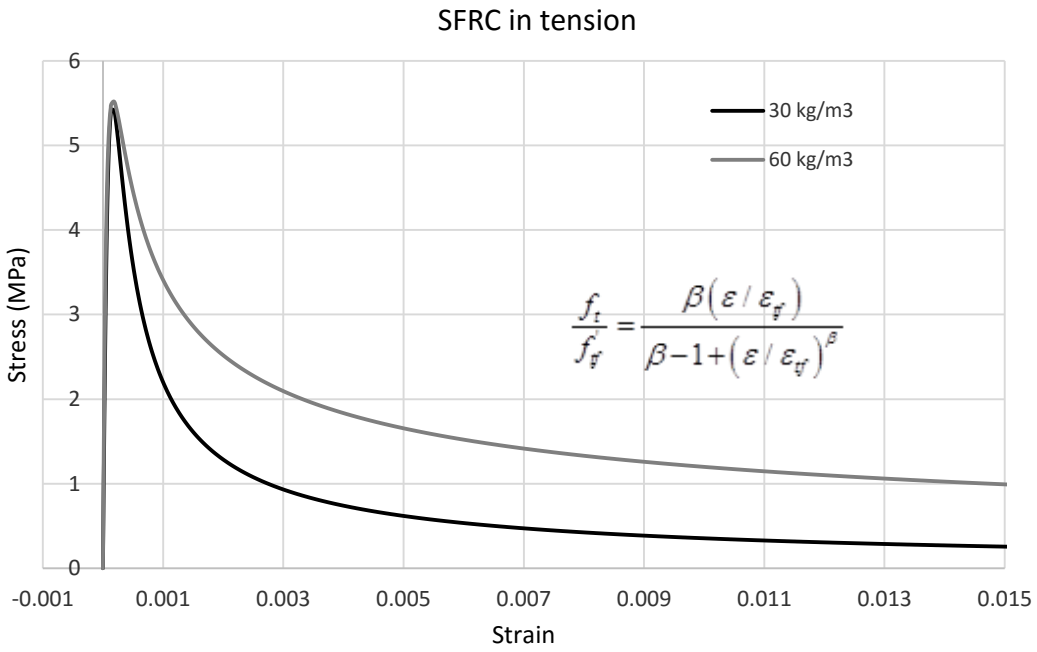

Figure 4.1.3-4 Stress-strain relationship of SFRC in tension

Table 4.1.3-2 Relevant parameters for SFRC tensile stress-strain curves

parameter	Acquirement	30SF	60SF	unit	description
$f_c^{'}$	Material test	57	55	MPa	
W_f	Predefined	30	60	kg/m^3	Fiber weight density
ρ_c	Material test	2400	2400	kg/m^3	Density of concrete
w_f	W_f/ρ_c	0.0125	0.025	-	Fiber weight ratio
l_f	Predefined	30	30	mm	length of fiber
d_f	Predefined	0.375	0.375	mm	diameter of fiber
R.I.	$w_f l_f / d_f$	1.00	2.00	-	Reinforcement index
η_0	Recommended by author	0.5	0.5	-	Orientation factor
V_f	$V_f = W_f/\rho_f$	0.0038	0.0076	-	Fiber volume fraction
N_f	$\eta_0(4V_f/\pi d_f^2)$	0.017	0.034	-	No. of fiber per unit area
$f_t^{'}$	$0.7\sqrt{f_c^{'}}$	5.284884105	5.191339	MPa	Tensile strength of plain concrete
E_c	Material test by UTM	35400	38935	MPa	modulus of plain concrete
ε_t	$f_t^{'}/E_c$	0.00015	0.00015	-	cracking strain of plain concrete
ε_{tf}	$\varepsilon_{tf}(1+0.35N_f d_f l_f)$	0.00016	0.00017	-	cracking strain of SFRC
$f_{tf}^{'}$	$f_t^{'}(1+0.016N_f^{1/3}+0.05\pi N_f d_f l_f)$	5.47	5.53	MPa	tensile strength of SFRC
β	$1.0930+0.7132R.I.^{-0.9260}$	1.81	1.47	-	

4.1.4 Modelling of steel rebar

The steel rebar which made of ductile material was modeled by “Plasticity” model available in ABAQUS. The program requires user to input tabular data sets represent stress-strain relationship of the material.

Actual tensile tests for steel rebars were conducted by the displacement controlled UTM. The yield stress and ultimate stress averaged from three test trials were 300MPa and 420MPa respectively. Elastic modulus was also measured in the test which was found to be closed to a theoretical value of 200GPa, this value was adopted in the model.

The stress-strain curve obtained from the test was found to have 3 main regions including elastic region, hardening region, and plastic region. Figure 4.1.4-1 illustrates a test result which shows that the steel rebar does not exhibit any softening behaviors even at high strain deformation in plastic region. Due to these facts, a simplified stress-strain curve as illustrated in figure 4.1.4-2 was used as tabular data sets for the plasticity model.

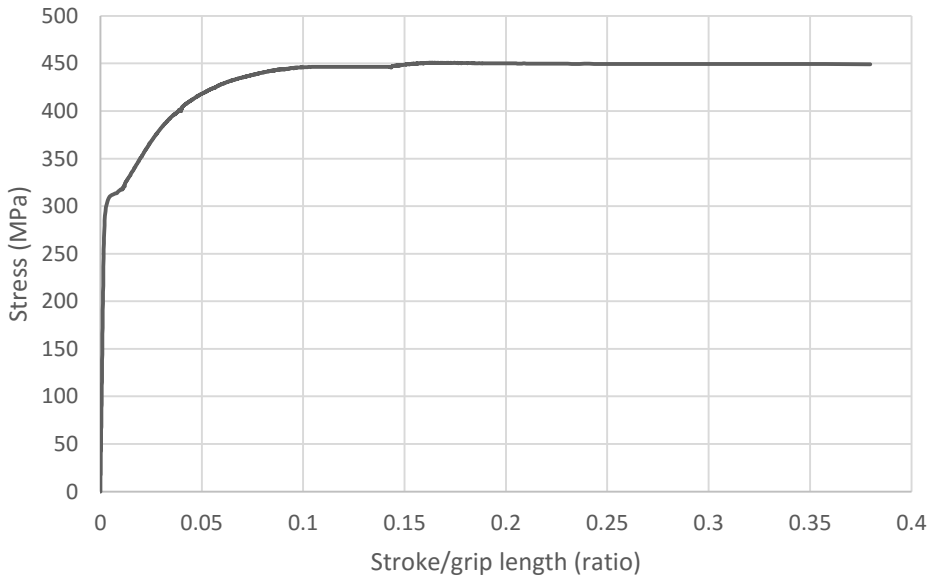

Figure 4.1.4-1 Stress-stroke/grip length curve from steel rebar tensile test

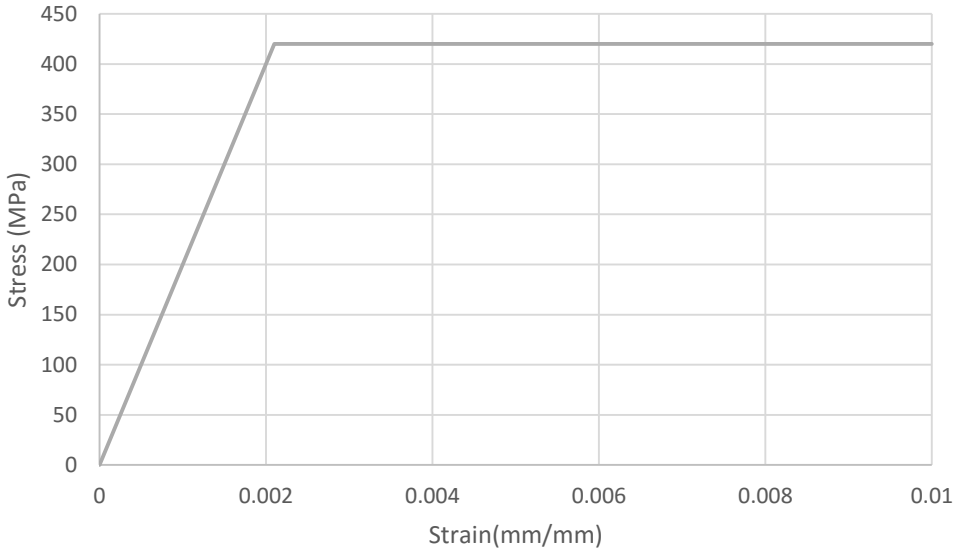

Figure 4.1.4-2 Simplified stress-strain curve for steel rebar

4.2 FEA modeling procedures

4.2.1 Building panel section

Since the problem was doubly symmetrical, only a quarter of the test specimen was modelled. In the modelling interface, that z-axis defines thickness of the panel, the model is symmetrical about x-axis and y-axis which has intersection at the center of the panel. The model had a geometry of 1000 x 500 x 75 mm to represent the actual test specimen size of 2000 x 1000 mm with 75mm thickness. The concrete part was assigned as solid element and the steel rebar was assigned as truss elements as shown in figure 4.2.1-1 and 4.2.1-2 respectively.

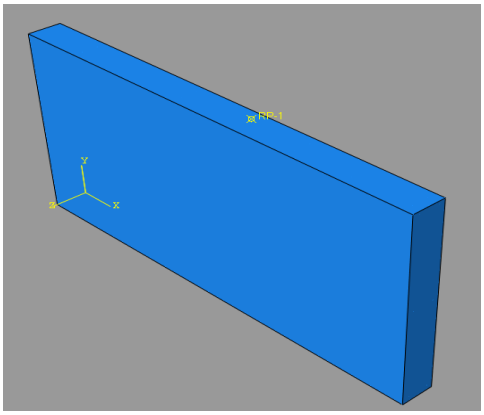

Figure 4.2.1-1 Solid element represents a quarter of actual panel section

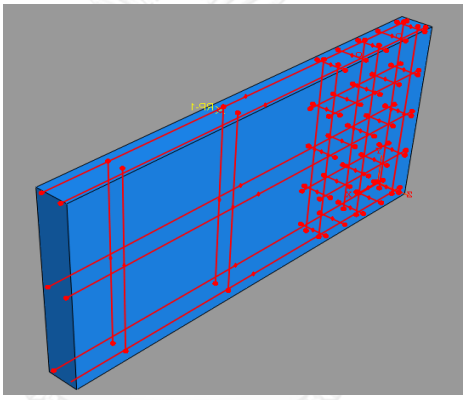

Figure 4.2.1-2 Truss elements represent steel rebar

4.2.2 Assumption and boundary condition

Since the model was doubly symmetrical about x-axis and y-axis, symmetrical boundary condition was defined along the cut sections. The cut section perpendicular to x-axis of the model (y-z plane) was assigned with restriction of translation along x-axis and rotation about y- and z-axis. Similarly, the cut section perpendicular to y-axis (x-z plane) was assigned with restriction of translation along y-axis and rotation about x- and z-axis. The assignment of symmetrical boundary was illustrated as shown in figure 4.2.2-1. In the program interface, the notation 1, 2, and 3 represented x, y, and z respectively; similarly, U denoted translation and UR denoted rotation.

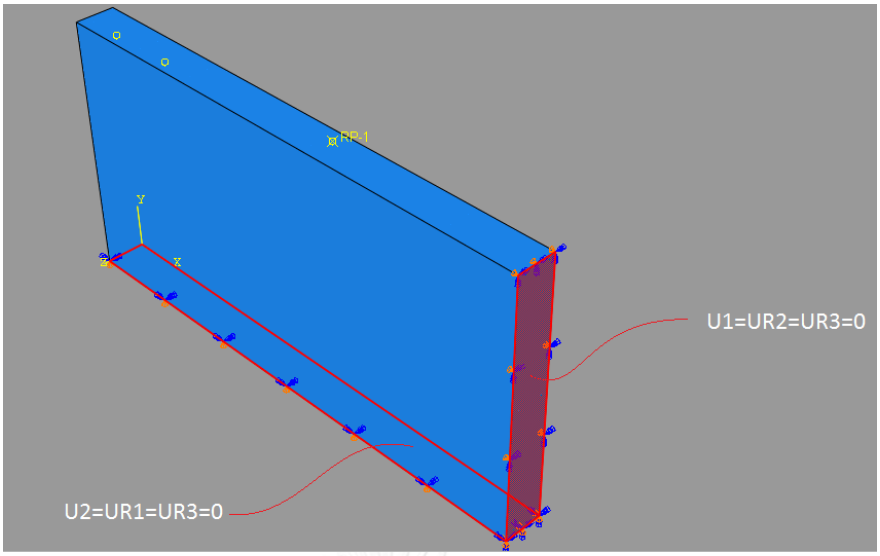

Figure 4.2.2-1 Doubly symmetrical boundary condition

Support condition of the specimen was also simulated by modeling an actual steel C section into the ABAQUS model. The C section was assigned as solid element which was in contact with the panel specimen. The C section element was assembled with the panel element as shown in Figure 4.2.2-2. One of the surfaces of the channel was then assigned as encased in order to simulate the fix support condition between the C section and the test rig as shown in Figure 4.2.2-3.

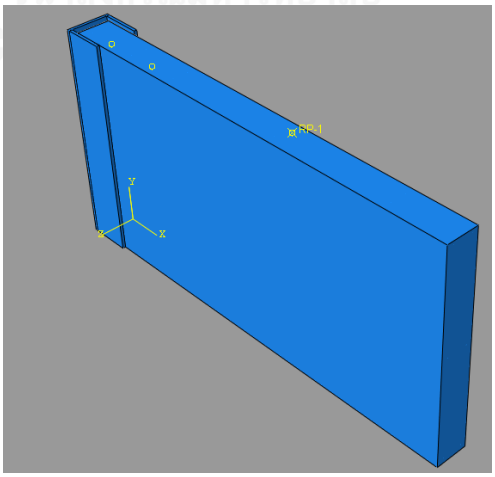

Figure 4.2.2-2 Panel attached with the C-section

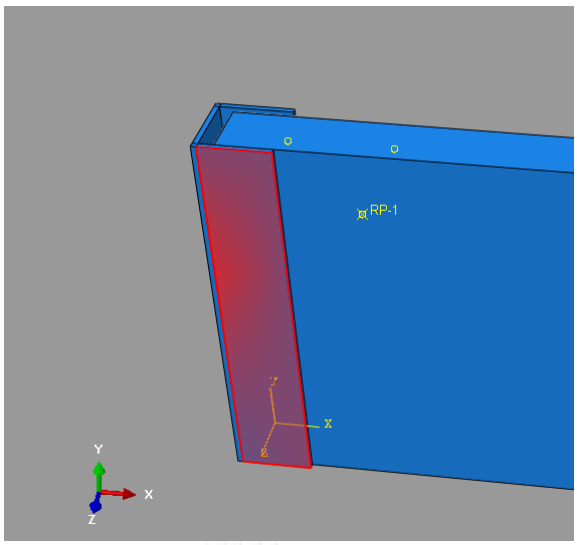

Figure 4.2.2-3 Restricted translation surface of C-section

4.2.3 Element meshing

In a finite element analysis, the problem was divided into small elements then the analysis result of all elements were combined together to make up a result for the whole problem. Smaller divided elements would give more accurate results, however, smaller elements also required greater computation time. Each of the components in the model was divided into equally sized elements; the element size was reduced after each analysis trial until the solution converged. Figure 4.2.3-1 showed a meshed panel element which was divided into 40,000 small elements. Similarly, all truss elements were divided into small elements with lengths of no more than 20 mm

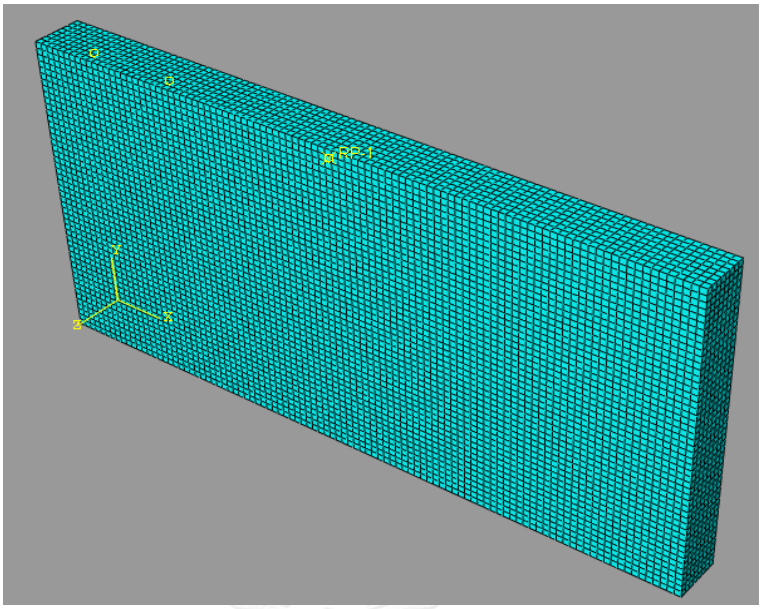

Figure 4.2.3-1 Meshed panel

4.2.4 Material interface modeling

The interaction between steel rebar and concrete was assumed as perfect bonding. The assumption was viable as unbounding or slippage between the rebar and concrete rarely occurs in high strain-rate loading scenario. The truss elements which represent reinforcing rebar were assigned as embedded into the concrete region. In the modelling interface, the truss elements were assigned as “embedded region” while the concrete solid element was assigned as “host region” as shown in the figure 4.2.4-1

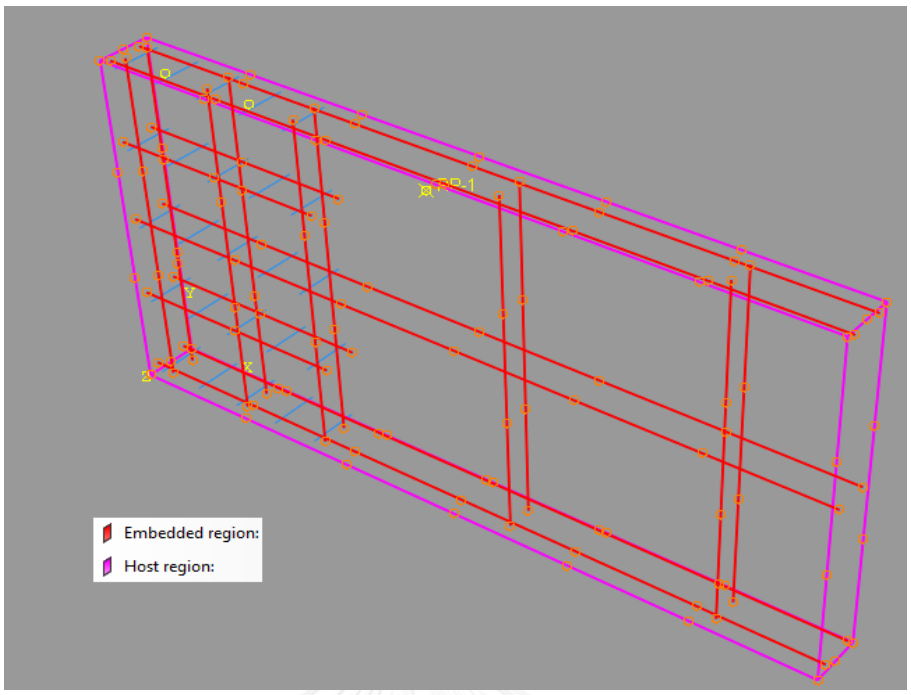

Figure 4.2.4-1 Truss elements are assigned as embedded into the panel

The contact between the C-section surfaces and the panel surfaces was modelled via "general contact" function in ABAQUS where any exterior surfaces of the elements which come into contact with each other during the analysis would not travel pass each other. The contact traction was also assumed as frictionless for both tangential and normal translations.

4.2.5 Blast load assignment

The blast load pressure was calculated and applied in the model using CONWEP function available in ABAQUS as mentioned in section 2.1.7. The CONWEP function required user to specify the blast source location (source point) and the affected surface area which was affected by the blast load. These were specified as shown in figure 4.2.5-1; the blast source was located at a point denoted RP-2 which was 500mm away from the affected surface bounded by a pink square. The profiles of blast pressure-time history at some surfaces of small meshed elements near to the blast source and those further away were as shown in figure 4.2.5-2. As illustrated in the figure, the surfaces which were nearer to the blast source experienced earlier and

greater peak pressure. This shown that, for this problem, the blast pressures applied to different meshed surfaces were greatly varied

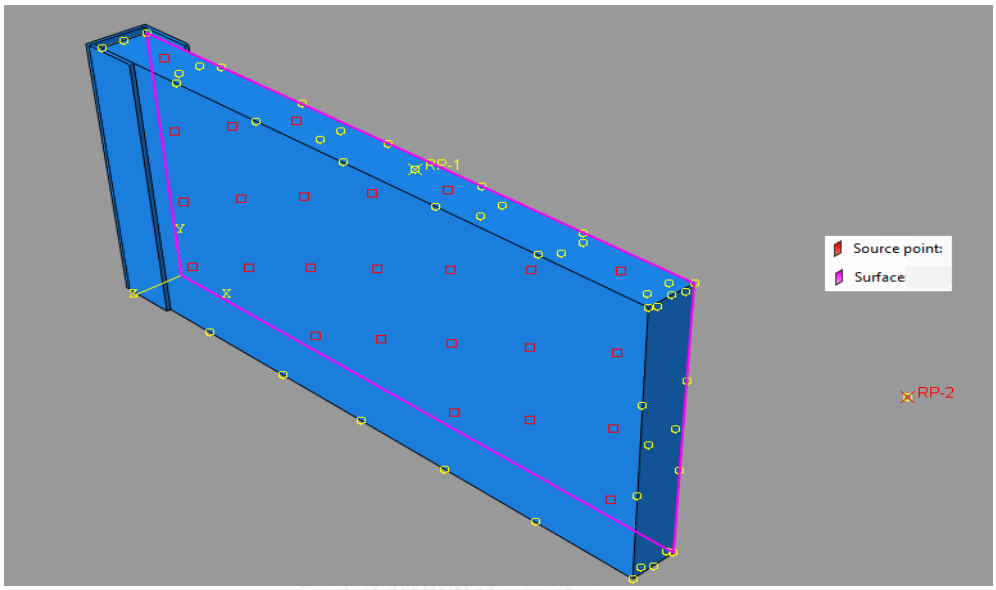

Figure 4.2.5-1 Specified source point and affected surface

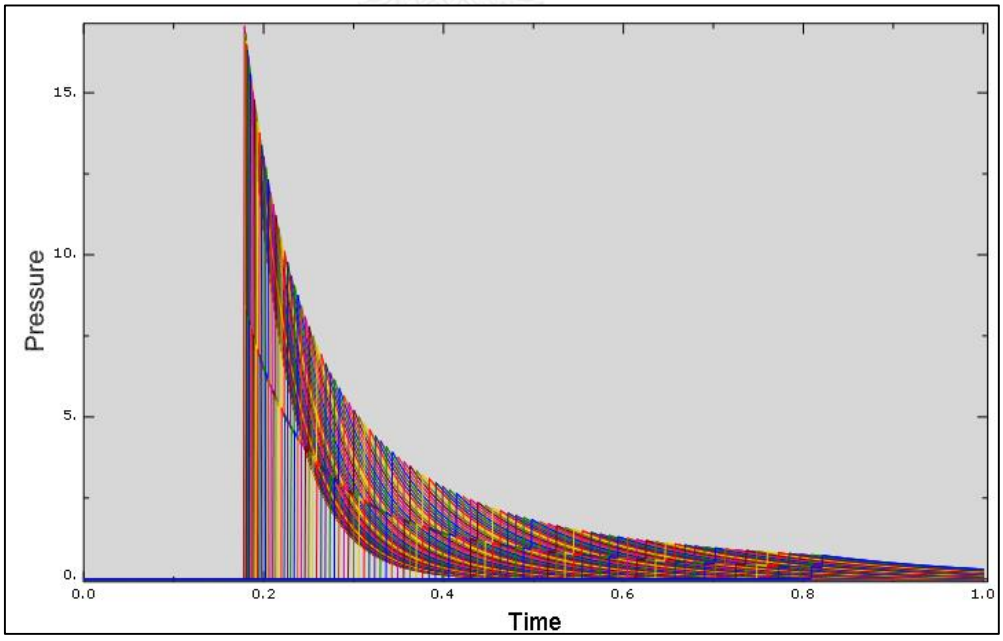

Figure 4.2.5-2 Simulated pressure-time history diagrams from 1lb TNT weight at 0.5 m standoff distance acting on small elements' surfaces (Pressure:MPa , Time : ms)

CHAPTER 5 Experiment and finite element analysis results

5.1 Experiment results and discussion

5.1.1 Test outcome with residual and maximum deflection records

This section reports experiment details and specimen pictures after each blast trial. Table 5.1.1-1 shows details of 6 experiment trials including the test order of specimens and explosive weight used for each test specimen. At the end of this section, residual and maximum deflection measurements for all specimens will be reported. For convenience Figure 5.1.1-1 shows again the partition and notation positioning of each test specimen.

denoted	NRC1LB	NRC2LB	30SF1LB	30SF2LB	60SF1LB	60SF2LB
explosive weight (lb)	1	2	1	2	1	2
Trial number	3	4	5	6	2	1
Date Time	1/25 4:57 PM	1/26 09:32 AM	1/26 10:55 AM	1/26 11:45 AM	1/25 2:43 PM	1/25 3:56PM

Table 5.1.1-1 Experiment trial details

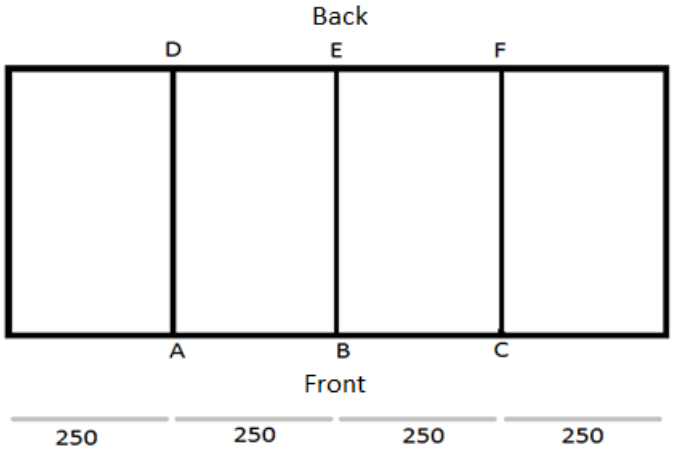

Figure 5.1.1-1 Partition and notation positioning

Pictures of following parts for all 6 tested specimens will be illustrated.

Top : top surface of the panel
Bottom: bottom surface of the panel
Front : whole front side of the panel
Back : whole back side of the panel

A : portion from the edge to position A of the front of the panel.
A-B : portion from position A to B of the front of the panel.
B-C : portion from position B to C of the front of the panel.
C : portion from position C to the edge of the front of the panel.

D : portion from the edge to position D of the back of the panel.
D-E : portion from position D to E of the back of the panel.
E-F : portion from position E to F of the back of the panel.
F : portion from position F the edge of the back of the panel.

NRC1LB

Top

Bottom

Figure 5.1.1-2 Top and Bottom of NRC1LB

NRC1LB

Front

(No picture available for back side see figure 5.1.1-5 for detailed pictures)

Figure 5.1.1-3 Front and back side of NRC1LB

NRC1LB

A

A-B

B-C

C

Figure 5.1.1-4 Marked location A to C of NRC1LB

NRC1LB

D

D-E

E-F

F

Figure 5.1.1-5 Marked location D to F of NRC1LB

NRC2LB

Top

Bottom

Figure 5.1.1-6 Top and Bottom of NRC2LB

NRC2LB

Front

Back

Figure 5.1.1-7 Front and Back side of NRC2LB

NRC2LB

A

A-B

B-C

C

Figure 5.1.1-8 Marked location A to C of NRC2LB

NRC2LB

D

D-E

E-F

F

Figure 5.1.1-9 Marked location D to F of NRC2LB

30SF1LB

Top

Bottom

Figure 5.1.1-10 Top and Bottom of 30SF1LB

30SF1LB

Front

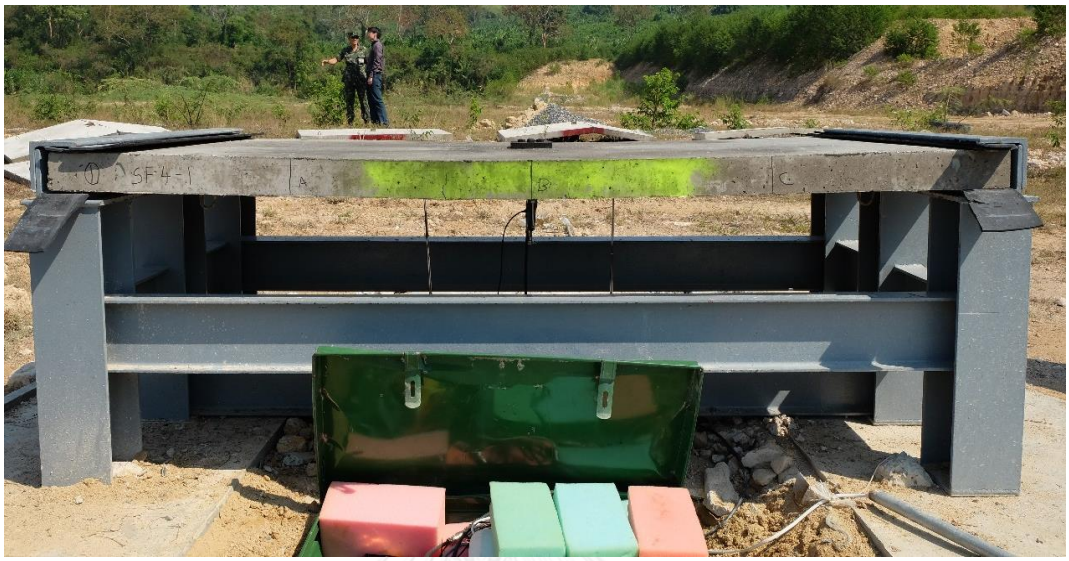

Back

Figure 5.1.1-11 Front and Back side of 30SF1LB

30SF1LB

A

A-B

B-C

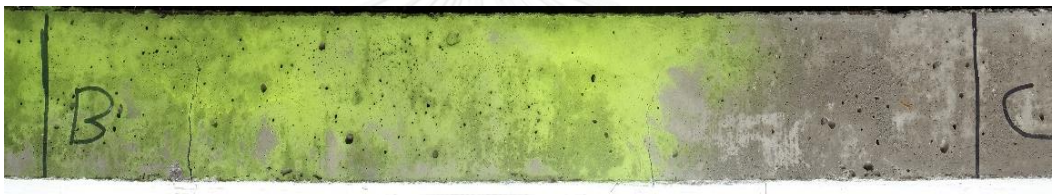

C

Figure 5.1.1-12 Marked location A to C of 30SF1LB

30SF1LB

D

D-E

E-F

F

Figure 5.1.1-13 Marked location D to F of 30SF1LB

30SF2LB

Top

Bottom

Figure 5.1.1-14 Top and Bottom of 30SF2LB

30SF2LB

Front

Back

Figure 5.1.1-15 Front and Back side of 30SF2LB

30SF2LB

A

A-B

B-C

C

Figure 5.1.1-16 Marked location A to C of 30SF2LB

30SF2LB

D

D-E

E-F

F

Figure 5.1.1-17 Marked location D to f of 30SF2LB

60SF1LB

Top

Bottom

Figure 5.1.1-18 Top and Bottom of 60SF1LB

60SF1LB

A

A-B

B-C

C

Figure 5.1.1-19 Marked location A to C of 60SF1LB

60SF1LB

D

D-E

E-F

F

Figure 5.1.1-20 Marked location D to F of 60SF1LB

60SF2LB

Top

Bottom

Figure 5.1.1-21 Top and Bottom of 60SF2LB

60SF2LB

Front

Back

Figure 5.1.1-22 Front and Back side of 60SF2LB

60SF2LB

A

A-B

B-C

C

Figure 5.1.1-23 Marked location A to C of 60SF2LB

60SF2LB

D

D-E

E-F

F

Figure 5.1.1-24 Marked location D to F of 60SF2LB

Results for residual and maximum deflection measured at the specified locations (A to F) as well as at the crack positions for all 6 specimens was summarized in Table 5.1.1-2. The measurement method was as explained in section 3.4. For better comparison, Tables 5.1.1-3 and 5.1.1-4 also shown separated reports for residual deflection and maximum deflection respectively.

Location (unit:mm)	A	B	C	D	E	F	front crack	rear crack
NRC1LB	24.0	42.0	21.0	26.0	44.0	20.0	44.1	46.2
	32.8	57.3	28.7	35.5	60.1	27.3	60.2	63.1
NRC2LB	98.0	161.0	83.0	92.0	185.0	93.0	184.3	186.5
	110.6	181.8	93.7	103.9	208.9	105.0	208.1	210.5
30SF1LB	12.0	18.0	8.0	9.0	16.0	10.0	21.0	17.5
	28.8	43.3	19.2	21.6	38.5	24.0	50.6	42.2
30SF2LB	76.0	116.0	58.0	78.0	122.0	61.0	132.2	133.7
	97.9	149.4	74.7	100.5	157.1	78.6	170.3	172.2
60SF1LB	3.0	11.0	8.0	3.0	11.0	7.0	11.0	11.0
	8.3	30.4	22.1	8.3	30.4	19.4	30.4	30.4
60SF2LB	80.0	120.0	54.0	82.0	127.0	59.0	138.2	144.1
	87.5	131.2	59.0	89.6	138.8	64.5	151.1	148.9

Table 5.1.1-2 Deflection records (unshaded = residual deflection, shaded = maximum deflection)

Location	A	B	C	D	E	F	front crack	rear crack
NRC1LB	24.0	42.0	21.0	26.0	44.0	20.0	44.1	46.2
NRC2LB	98.0	161.0	83.0	92.0	185.0	93.0	184.3	186.5
30SF1LB	12.0	18.0	8.0	9.0	16.0	10.0	21.0	17.5
30SF2LB	76.0	116.0	58.0	78.0	122.0	61.0	132.2	133.7
60SF1LB	3.0	11.0	8.0	3.0	11.0	7.0	11.0	11.0
60SF2LB	80.0	120.0	54.0	82.0	127.0	59.0	138.2	144.1

Table 5.1.1-3 Residual deflection records (unit:mm)

Location	A	B	C	D	E	F	front crack	rear crack
NRC1LB	32.8	57.3	28.7	35.5	60.1	27.3	60.2	63.1
NRC2LB	110.6	181.8	93.7	103.9	208.9	105.0	208.1	210.5
30SF1LB	28.8	43.3	19.2	21.6	38.5	24.0	50.6	42.2
30SF2LB	97.9	149.4	74.7	100.5	157.1	78.6	170.3	172.2
60SF1LB	8.3	30.4	22.1	8.3	30.4	19.4	30.4	30.4
60SF2LB	87.5	131.2	59.0	89.6	138.8	64.5	151.1	148.9

Table 5.1.1-4 Maximum deflection record (unit:mm)

	Maximum deflection (mm)	Displacement (% of NRC)	Residual deflection (mm)	Displacement (% of NRC)
NRC1LB	61.5	-	45.0	-
30SF1LB	50.1	81	19.5	43
60SF1LB	24.5	40	9.0	20

Table 5.1.1-5 Comparison of maximum displacement and residual displacement for specimens subjected to 1lb loading

	Maximum deflection (mm)	Displacement (% of NRC)	Residual deflection (mm)	Displacement (% of NRC)
NRC2LB	209.5	-	185.0	-
30SF2LB	171.0	82	133.0	72
60SF2LB	154.4	72	141.0	76

Table 5.1.1-6 Comparison of maximum displacement and residual displacement for specimens subjected to 2lb loading

For the purpose of discussion and comparison, table 5.1.1-5 and 5.1.1-6 reported separately averaged maximum and residual displacement values for 1lb and

2lb blast load cases respectively. Each of the reported values was an averaged value of displacement values measured at front and rear crack location. The experiment results shown reduction in residual and maximum deflection after the inclusion of steel fiber for both specimen sets subjected to 1lb and 2lb explosive loading. However, the reduction percentages were found to be more pronounced for the specimen group subjected to 1lb explosive loading.

For the specimens subjected to 1lb explosive loading, many flexural cracks appeared on the specimen NRC1LB; only minor flexural cracks were found on the specimen 30SF1LB and none were found on the specimen 60SF1LB. The experiment results also show that an inclusion of 30kg/m^3 steel fiber resulted in a pronounced reduction in deflection response by 19% for maximum displacement and 57% for residual displacement, the increase of fiber ratio from 30kg/m^3 to 60kg/m^3 reduced the displacement response by an additional of 41% for maximum displacement and 23% for residual displacement.

For the specimen group subjected to 2lb explosive loading, the experiment results shown that an inclusion of 30kg/m^3 steel fiber reduced deflection response by 18% for maximum deflection and 28% for residual deflection, however, the increase of fiber ratio from 30kg/m^3 to 60kg/m^3 had only minor effect on the reduction of displacement response and, in fact, worsen the response behavior for residual displacement. The additional maximum displacement reduction was 10% while the residual deflection was worsen by an increase of 2%. The 2% increase was due to the fact that, in a specimen with greater amount of fiber, higher force was required against the resistance from the effect of fibers being pushed back to their original position during the upward movement of the specimen from maximum to final location.

This could be concluded that, although the inclusion of steel fiber effectively reduced both residual and maximum deflection of both specimen groups, the increase of fiber ratio (from 30kg/m^3 to 60kg/m^3) has less efficient increase for the specimens subjected to 2lb explosive load. This due to the effect of fiber clumping which reduced the pull out capacity of each steel fiber in concrete resulting in less effectiveness in

increasing capacity of the concrete in resisting tensile stress especially for plastic behavior.

5.1.2 High-speed video result

From the processing of all recorded video footages, time-history deflection response was successfully extracted from only 1 out of 6 recorded footages; this was because several adjustments on the camera were needed before a clear movement of the panel during the blast could be captured; the displacement responses of specimens subjected to 1lb loading were also too small to observe in the footages. The time-history deflection response of the test trial denoted 30SF2LB were successfully extracted as shown in figure 5.1.2-1 through 5.1.2-4. The figures shown panel movements at certain time periods several milliseconds after the detonation. The movement at the maximum displacement along the front edge or at the front crack position was interpreted through image processing into data points as shown in Figure 5.1.2-5 and Table 5.1.2-1. The interpretation of the displacement response was done by counting the pixels moved by a certain point on the panel crack where one pixel was equivalent to 3.64 mm length on the panel. As all points on the panel moved together respectively and reached maximum displacement at the same time, the percentages of maximum displacements was also reported in table 5.1.2-1 which could be used to calculate for displacements of any points on the panel. Figure 5.1.2- 1 shown a plotted displacement response curve of specimen 30SF2LB which would be useful for the comparison with analysis results of this specimen.

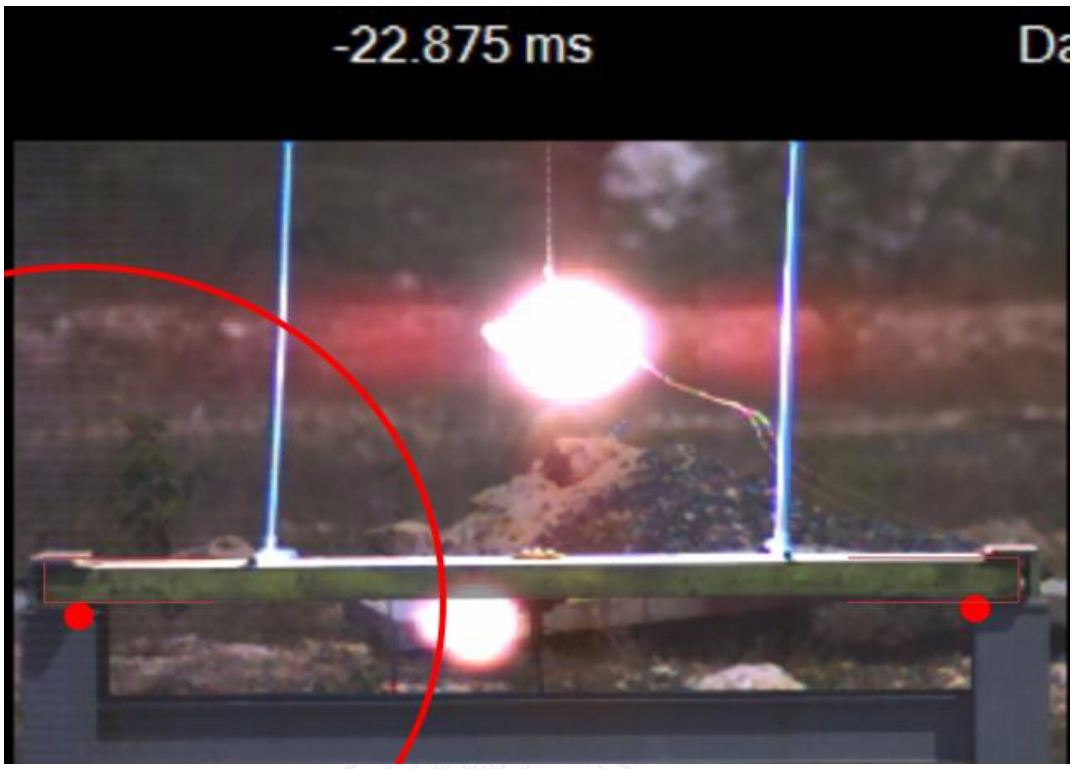

Figure 5.1.2-1 Video footage at 0ms (detonation)

Figure 5.1.2-2 Video footage at 3.975 ms

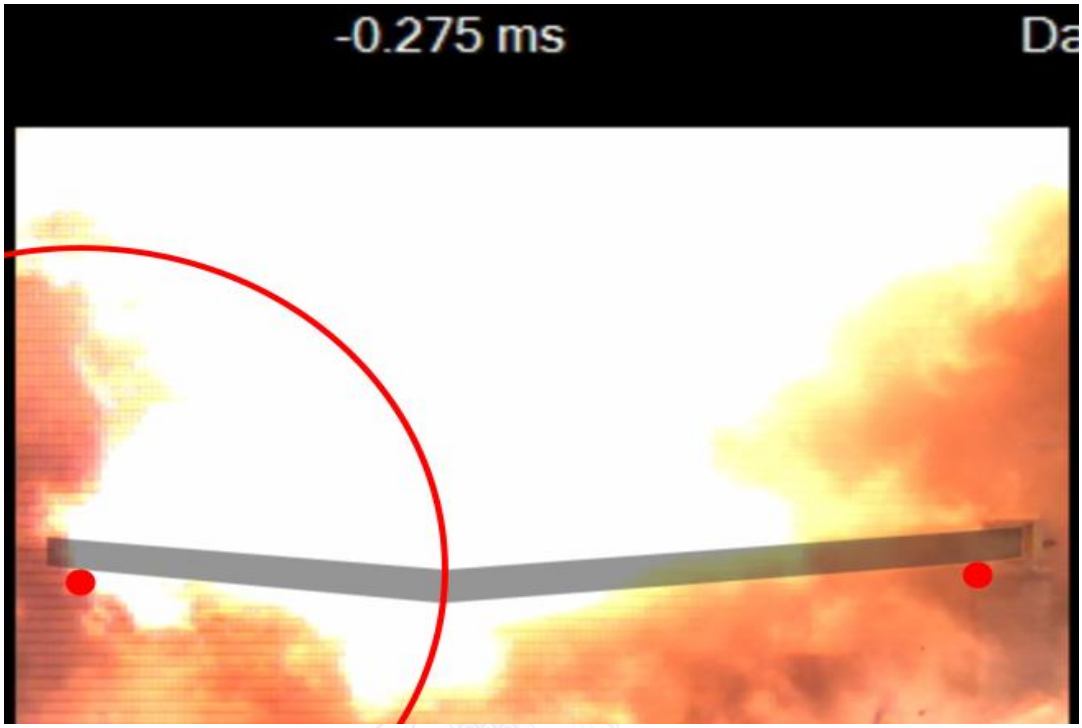

Figure 5.1.2-3 Video footage at 22.600 ms

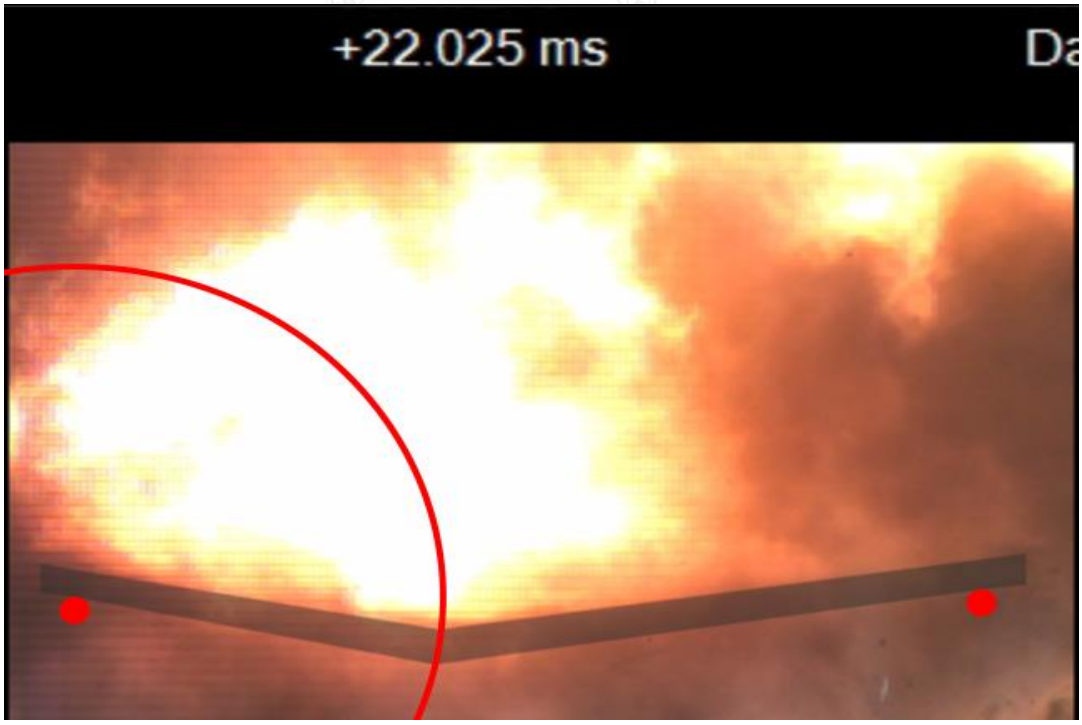

Figure 5.1.2-4 Video footage at 44.900 ms

reference time (ms)	calibrated time (ms)	pixel moved	Displacement (mm)	Displacement (% maximum)
-22.88	0.00	0	0	0.0
-18.90	3.98	0	0	0.0
-16.35	6.53	11	40.0	23.4
-12.13	10.75	21	76.4	44.7
-0.28	22.60	34	123.7	72.3
11.88	34.75	42	152.8	89.4
22.03	44.90	47	171.0	100.0
43.55	66.43	38	138.3	80.9

Table 5.1.2-1 Interpretation of panel displacement

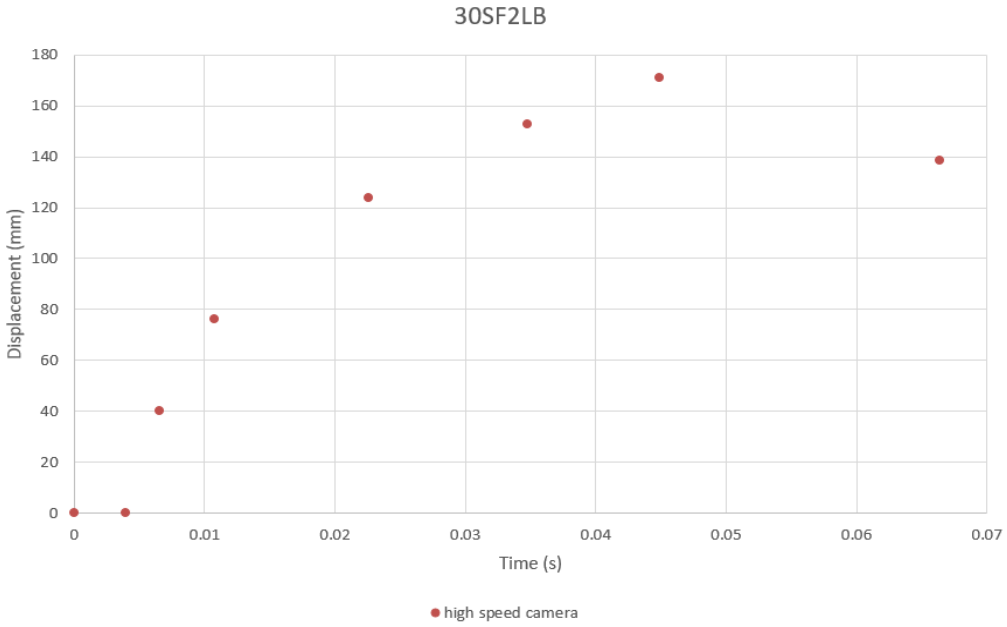

Table 5.1.2-2 Time-displacement history graph of the panel 30SF2LB

5.2 Finite element analysis results and comparison with experiment results

5.2.1 Maximum displacement results and comparisons

Maximum displacement occurred at the corner node nearest to the blast source located at the location as shown in figure 5.2.1-1. Nodal displacement in z direction at the node was obtained from the tabular field displacement outputs for each of the 6 models. Figure 5.2.1-2 through 5.2.1-7 shown comparison between the plotted tabular data sets from analysis and experiment maximum displacement measured at the middle of the test panel for NRC1LB, NRC2LB, 30SF1LB, 30SF2LB, 60SF1LB and 60SF2LB respectively.

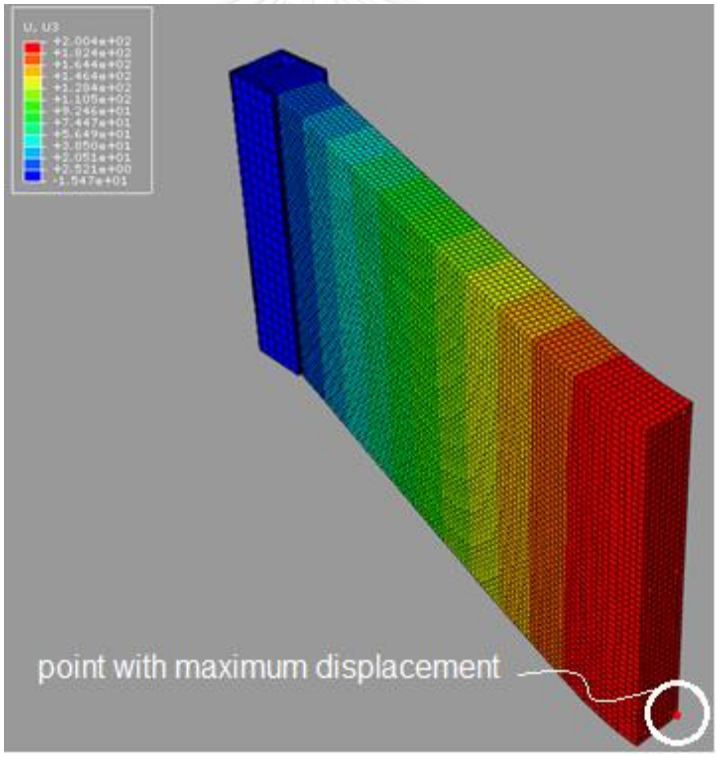

Figure 5.2.1-1 Node location for displacement output

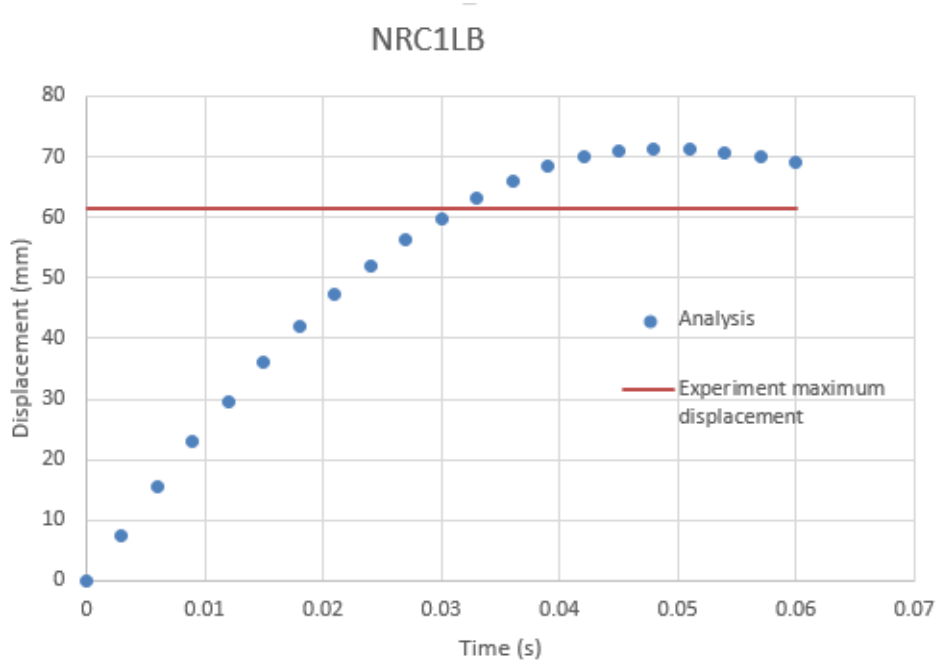

Figure 5.2.1-2 Tabulated analysis displacement output and experiment data for NRC*1*LB

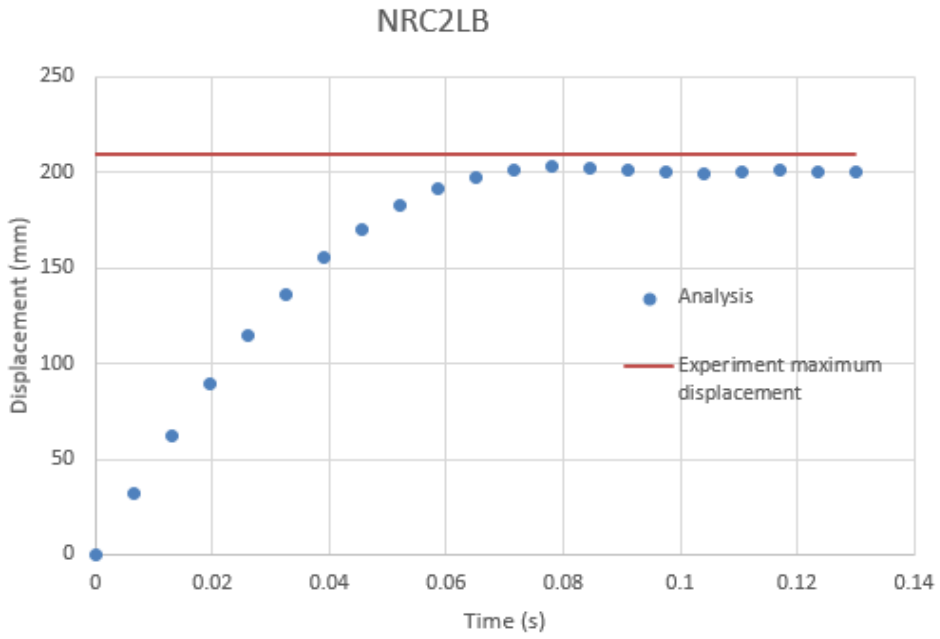

Figure 5.2.1-3 Tabulated analysis displacement output and experiment data for NRC2LB

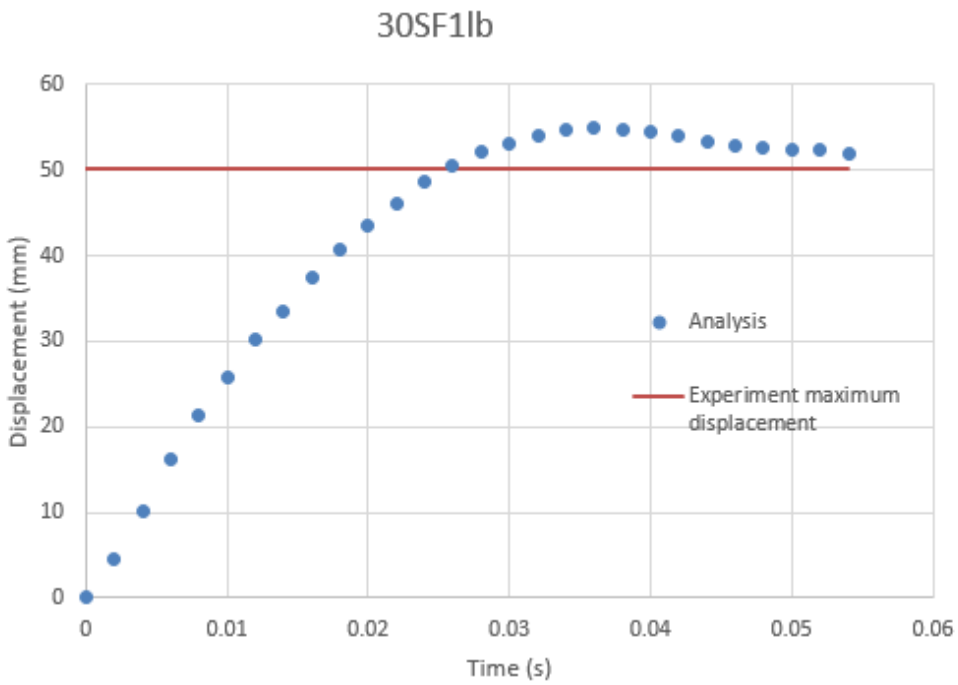

Figure 5.2.1-4 Tabulated analysis displacement output and experiment data for 30SF1LB

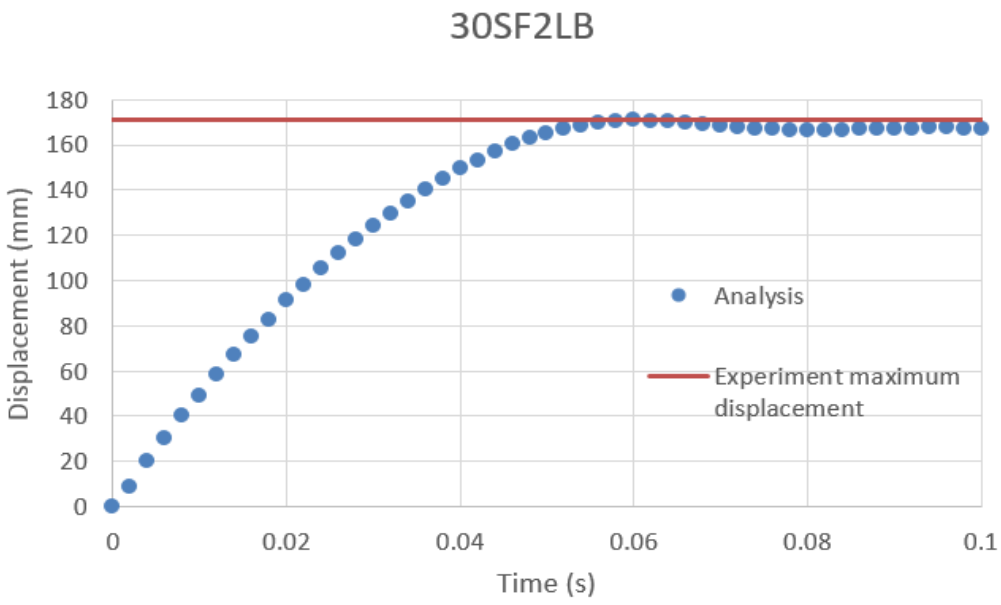

Figure 5.2.1-5 Tabulated analysis displacement output and experiment data for 30SF2LB

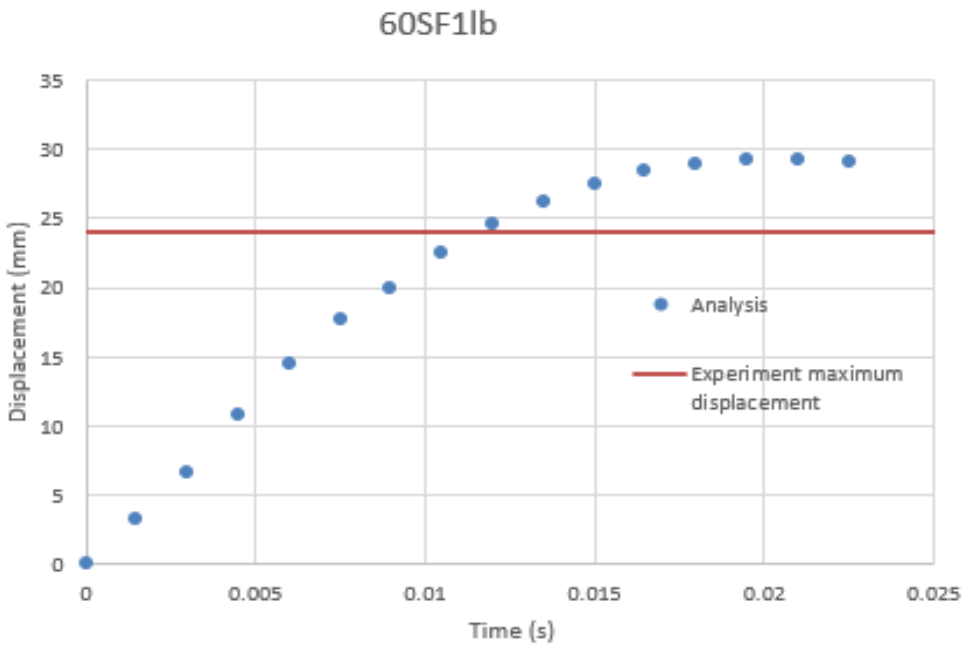

Figure 5.2.1-6 Tabulated analysis displacement output and experiment data for 60SF1LB

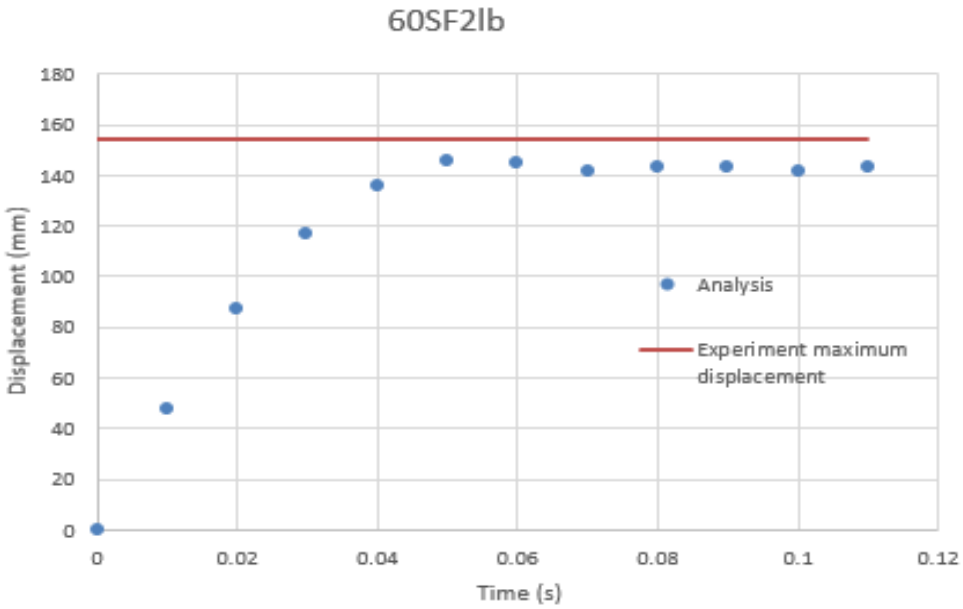

Figure 5.2.1-7 Tabulated analysis displacement output and experiment data for 60SF2LB

The analysis results were found to have very small discrepancy as compared to the experimental results. Table 5.2.1-1 shown the discrepancy percentages of predicted maximum displacement values as compared to the test results. The analysis overestimated the displacement responses for specimens subjected to 1lb loading while underestimated the displacement responses for specimens subjected to 2lb loading. The discrepancy was found to be smaller for specimens subjected to larger 2lb blast load where the largest discrepancy was only 3.9% for specimen 60SF2LB. The discrepancy was greater for specimens subjected to 1lb load, but within an acceptable limit, where the maximum was 16% for specimen NRC1LB.

Specimen	NRC1LB	30SF1LB	60SF1LB	NRC2LB	30SF2LB	60SF2LB
analysis	71	55	29	203	170	145
experiment	62	50	25	210	171	150
Discrepancy %	14.5	10.0	16.0	3.3	0.6	3.3
Average %	13.3			2.4		
Average %	7.85					

Table 5.2.1-1 Maximum displacement comparison between analysis and experiment data

5.2.2 Comparison between analysis result and high-speed camera result

The time history displacement response of the specimen 30SF2LB recorded by high-speed camera was plotted and compared with the tabular field displacement outputs from the analysis as shown in Figure 5.2.2-1. The figure shown that the analysis predicted the maximum displacement response of the panel and the time where maximum displace was reached with small discrepancies. The maximum displacement was underestimated by only 1.8%. The predicted time at maximum displacement was 58ms as compared to 45ms from the actual experiment meaning the discrepancy was only 13ms.

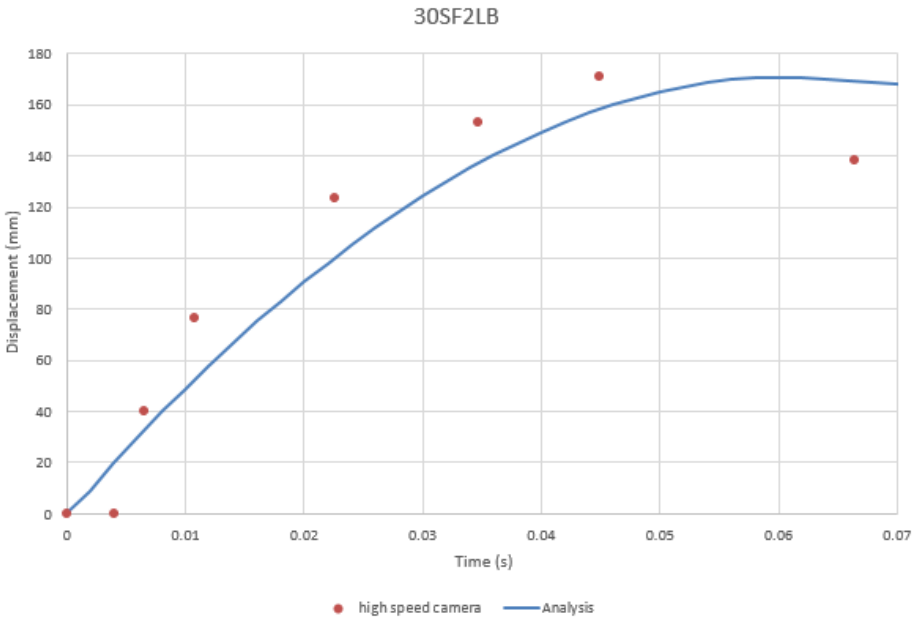

Figure 5.2.2-1 Comparison between analysis and experiment results from high speed camera for 30SF2LB

5.2.3 Crack propagation characteristic from analysis and actual experiment result

Figure 5.2.3-1, 5.2.3-2, and 5.2.3-3 shown flexural crack propagation from the actual experiment side by side with that from analysis result for specimens NRC2LB, 30SF2LB, and 60SF2LB respectively. The analysis results diagrams shown crack propagation behavior where colored (non-grey) regions represented visible crack paths formed by small elements with principal strain according to the color scales. The figures shown that there was a similarity between the experiment and analysis results where flexural cracks were found to be more distributed for NRC panel (NRC2LB) as compared to a more concentrated single flexural crack for SFRC panels (30SF2LB and 60SF2LB). This behavior was counterintuitive as the flexural cracks should have been more distributed with smaller crack bands for fiber reinforced panel which was not the case for dynamic loading scenario.

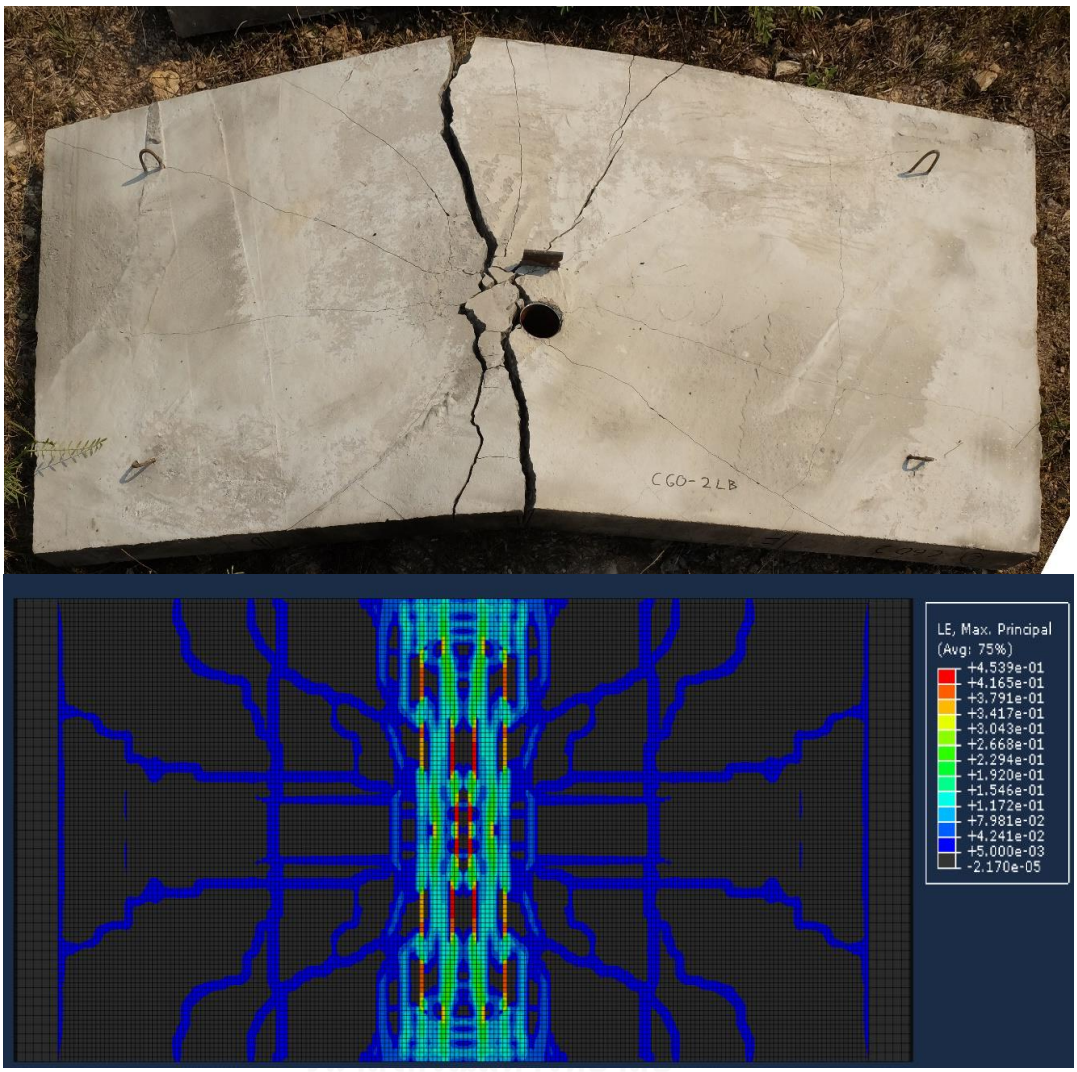

Figure 5.2.3-1 Crack propagation at the bottom surface of panel NRC2LB

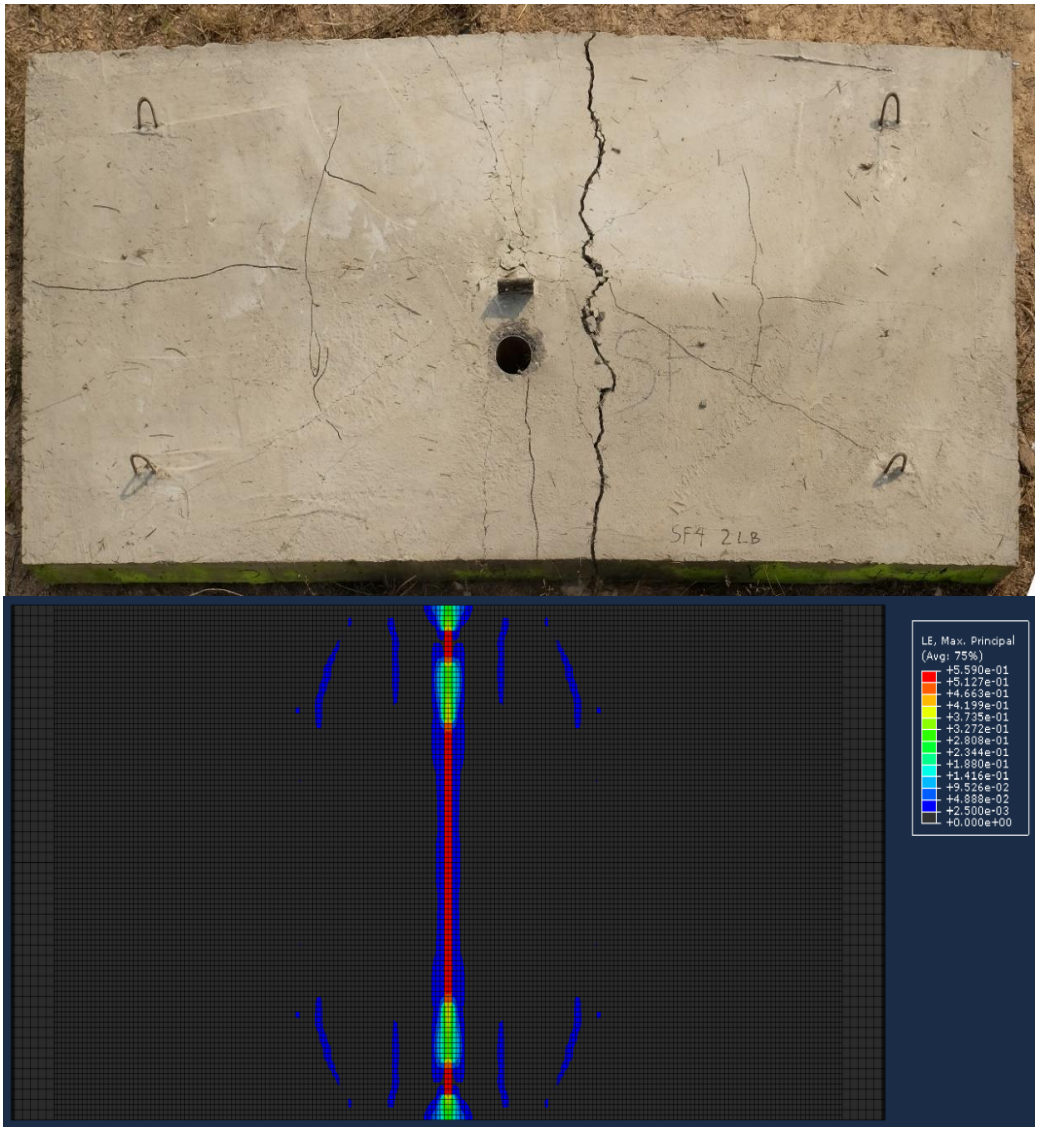

Figure 5.2.3-2 Crack propagation at the bottom surface of panel 30SF2LB

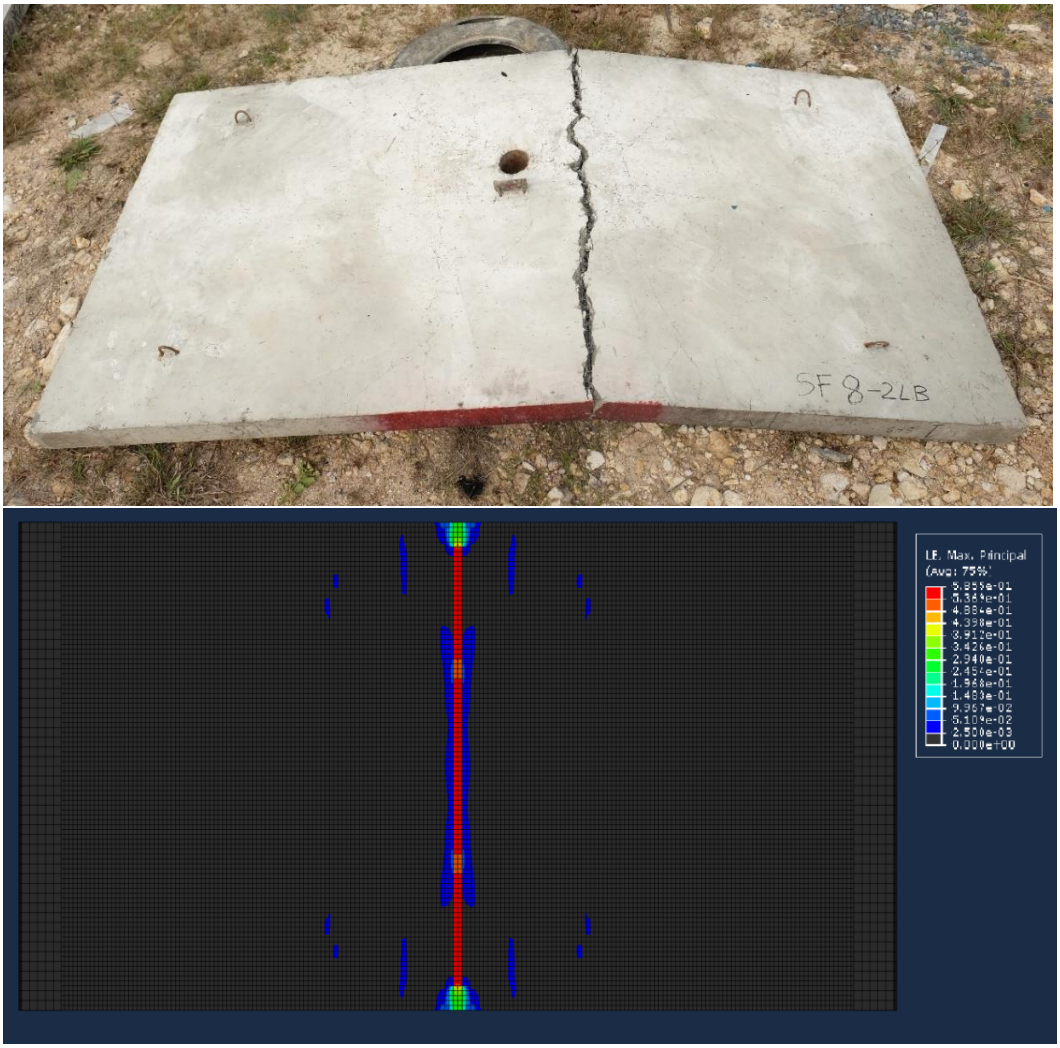

Figure 5.2.3- 1 Crack propagation at the bottom surface of panel 60SF2LB

CHAPTER 6 **Conclusion**

The author investigated the improvement in blast resisting capacity of concrete panel after the inclusion of hooked-type steel fiber; the improvement from increasing steel-fiber with weight ratio from 30kg/m^3 to 60kg/m^3 was also investigated. The improvement was purely due to the inclusion of steel-fiber as all other parameters such as concrete strength, steel reinforcement grade and configuration, blast load, and panel geometry were carefully controlled for all specimens. Analytical models using ABAQUS were also developed to simulate the response of the specimens. The simulated responses were validated by the experiment results for the accuracy in predicting maximum displacement response of the panels. This thesis may be concluded as following

1) The inclusion of steel-fiber into the concrete flexural elements subjected to blast-load resulted in an increase of resisting capacity as indicated by the reduction in maximum deflection and residual deflection responses of the test specimens.

2) The increase of steel-fiber ratio by double (from 30 to 60 kg/m^3) further reduced displacement responses, however, the reduction was marginal for the case of 2lb blast loading where most proportion of the concrete was in plastic behavior.

3) The developed analytical models were validated as being accurate in predicting maximum displacement for all specimens. The analytical model was able to predict the maximum displacement and the time at which the maximum displacement was reached with very small discrepancies. Thus, the modeling procedures used in this study was suitable in modelling the responses for other flexural elements subjected to blast load.

The design of structure subjected to blast load is elemental focus, meaning the survivability of a whole structure is owned to a prevention of progressive collapses caused by the failure of the structural element subjected to explosive loading. The elements of concerned structure such as floor slabs, walls, and columns that are expected to be exposed by the blast load should be designed to withstand explosive loading. The elements should still be able to withstand normal working load after being weaken by the blast load. For example, a column exposed to a blast load will be permanently deflected afterward causing additional eccentric loading to the column which may eventually cause it to fail. Thus, knowing the deflection response of the column is vital in design for survivability of a structure subjected to blast loading. The same is considered for beams and slabs which also serve as structural elements.

This thesis has proven that the inclusion of steel-fiber would not only prevent cracks due to creep and shrinkage of concrete but would also increase the blast-load resisting capacity; the modeling procedures used in this thesis was also appropriate in predicting the deflection response of flexural elements subjected to blast-load. This should be useful in the design of structures prone to blast loading especially the ammunition storage.

REFERENCES

AL-TAAN, S. A., & SHAMMAS, S. S. Y. (2006). Nonlinear Time-dependent Finite Element Analysis of Fibrous Reinforced Concrete Beams. *Jordanian Conference on Civil Engineering*.

Alih, S., & Khelil, A. (2012). Tension Stiffening Parameter in Composite Concrete Reinforced with Inoxydable Steel. *International Journal of Civil and Environmental Engineering, 6*.

Baker, W. E., Cox, P., Westine, P. S., Koles, J. J., & Strehlow, R. A. (1983). *Explosion hazard and evaluation* (Vol. 5).

Beshara, F. B. A. (1994). Modeling od blast loading on above ground structures-II. Internal blast and fround shock. *Computers & Structures*, 585-596.

Bhargava, P., Sharma, U. K., & Kaushik, K. (2005). Compressive Stress-strain Behavior of Small Scale Steel Fibre Reinforced High Strength Concrete Cylinders. *Journal of Advanced Concrete Technology, 4*(1), 109-121.

Borenstein, E., & Benaroya, H. (2009). Sensitivity analysis of blast loading parameters and their trends as uncertainty increases. *Journal of Sound and Vibration, 321(3-5)*, 762-785.

Brode, H. L. (1955). Numerical Solution of Spherical Blast Waves *Journal of Applied Physic*.

Cadoni, E., Meda, A., & G.A., P. (2009). Tensile behavior of FRC under high strain-rate. *Marer Struct*.

Chock, J. M., & Kapania, R. K. (2001). Review of two methods for calculating explosive air blast. *Shock and Vibration*.

Crepeau, J. (2001). *SHAMRC Second-Order Hydrodynamic Automatic Mesh Refinement Code* (Vol. 2). Albuquerqu: Applied Research Associates.

Ezeldin, A. S., & Balaguru, P. N. (1992). Normal and High

Strength Fibre Reinforced Concrete Under Compression. *Journal of Materials and Engineering, 4*.

GSA. (2003). *Progressive Collapse Analysis and Design Guidelines for New Federal Office Buildings and Major Modernization Projects*. Washington, D.C.: Progressive Collapse Analysis and Design Guidelines for New Federal Office Buildings and Major Modernization Projects.

Guzas, E. L., & Earls, C. J. (2010). Air Blast Load Generation for Simulating Structural Response. *Steel and Composite Structures, 10*(5), 429-455.

Hibbitt, Karisson, & Sorensen. (2008). *ABAQUS standard user's manual.* (Vol. 3).

Kingery, C. N., & Bullmash, G. (1984). *Air Blast Parameters from TNT Spherical Air Burst and Hemispherical Surface Blast* (ARBRL-TR-02555). Retrieved from

Kinnery, G. F., & Graham, K. J. (1985). *Spring-Verlag*

Malvar, J. L., & Crawford, E. J. (1998). *Dynamic Increase Factor For Steel Reinforcing Bars*. Retrieved from Naval Facilities Engineering Service Center:

Malvar, L. J., & Crawford, J. E. (1998, Aug. 18-20). *Dynamic increase factors for concrete.* Paper presented at the Proceeding of the 28th Department of Defense Explosives Safety Seminar (DDESB).

Mccann, D. M., & Smith, S. J. (2007). Blast resistant design of Reinforce Concrete Structures. *Structure Magazine,* 22-26.

Mechtcherine, V., Silva, F. A., Butler, M., Zhu, D., & Mobasher, B. (2011). Behaviour of strain-hardening cement-based composites under high strain rates. *Advance Concrete Technology*, 51-52.

Ngo, T., Mendis, P., Gupta, A., & Ramsay, J. (2007). Blast loading and blast effect on structures - an overview. *Loading on Structures*, 76-91.

Randers, P. G., & A.B., K. (1997). *U.S. Army Research LaboratoryTechnicalReport*. Retrieved from

Smith, P. D., & Hetherington, J. G. (1994). *Blast and Ballistic Loading of Structure*. Retrieved from London:

Soroushian, P., & Lee, C. D. (1989). *Constitutive Modeling of Steel Fiber Reinforced Concrete Under Direct Tension and Compression*. Paper presented at the International Conference on Recent Developments in Fibre Reinforced Cement Concrete. , Cardiff

Tanapornraweekit, G., Haritos, N., Mendis, P., & Ngo, T. (2010). Finite element simulation of FRP strengthened reinforced concrete slabs under two independent air blasts. *International Journal of Protective Structures, 1*(4), 469-488.

Tran, T. K., & Kim, D. J. (2014). High strain rate effects on direct tensile behavior of high performance fiber reinforced cementitious composites. *Cement and Concrete Composites, 45*, 186-200. doi:http://dx.doi.org/10.1016/j.cemconcomp.2013.10.005

US Department of the Army. (1990). TM-5-1300Design of Structures to Resist the Effects of Accidental Explosions.

Wahalathantri, B. L., & Thambiratnam, D. P. (2008). A material model for flexural crack simulation in reinforced concrete element using ABAQUS. *Infrastructure Transport and Urban Development*, 260-264.

WBDG. (2016). Whole Building Design Guide. Retrieved from https://www.wbdg.org/design/ammo_magazines.php

Wight, J. K., & MacGregor , J. G. (2012). *Reinforced Concrete Mechanics and Design* (6 Ed.): Pearson Education.

Wu, C., Oehlers, D. J., Rebentrost, M., Leach, J., & Whittaker, A. S. (2009). Blast testing of ultra-high performance fibre and FRP-retrofitted concrete slabs. *Engineering Structures, 31*(9), 2060-2069. doi:http://dx.doi.org/10.1016/j.engstruct.2009.03.020

APPENDIX

VITA

Sakkasem Suwarnarat was born on the 3rd of september, 1987. Sakkasem is a graduate of The University of Melbourne, where he received a bachelor's degree in civil engineering in the year 2012. After graduation, Sakkasem launched his career at an engineering firm named Meinhardt in Bangkok, where he began his specilization in structural engineering. After a year of working, he later started his master degree in engineering at the Chulalongkorn University from the year 2013. During his master study, he had an opportunity to present his research work "Performance of Steel Fiber Reinforced Concrete Panel Subjected to Air-blast Loading" at a conference namely "The 21st National Convention on Civil Engineering" held at Songkhla, Thailand on the 28-30th of June, 2016.